

**Voltage-Tunable 2D and 3D Structures
of Gold Nanoparticles at a Water/1,2-Dichloroethane Interface**

BY

DANIEL AMOANU

B.S. (Kwame Nkrumah University of Science and Technology, Kumasi, Ghana) 2004

M.S. (Lappeenranta University of Technology, Lappeenranta, Finland) 2009

THESIS

Submitted in partial fulfillment of the requirements for the degree of Doctor of Philosophy in
Chemical Engineering in the Graduate College of the University of Illinois at Chicago, 2018

Chicago, Illinois

Defense Committee:

Professor Mark L. Schlossman, Department of Physics, Advisor
Professor Lewis E. Wedgewood, Department of Chemical Engineering, Chair
Professor Ludwig Nitsche, Department of Chemical Engineering
Professor Vivek Sharma, Department of Chemical Engineering
Professor Ursula Perez-Salas, Department of Physics

Copyright by
Daniel Amoanu
2018

To my late father, Kojo Amoanu. You sacrificed everything for me to be where I am today and you are my role model.

To my mom, thank you for your constant advice and love.

To my brothers and sisters. Amoanu family. Thanks for your support.

ACKNOWLEDGMENTS

I would like to thank my advisor, Professor Mark L. Schlossman, who patiently guided me throughout the course of my studies. I learned invaluable skills and attitudes from him throughout my study. I am amazed and motivated by his high standards and the expectations he put on himself and expects from others. I do not have enough words to thank him. Also, I thank my group members, Zhu Liang, Cem Erol and Stephen Geiman who helped me take and analyze data.

Special thanks to Amoanu family especially my late father who passed way in October 2014. Without him, I would not be where I am today and what I am today. I thank my mom who always encourages me to do the right thing and stay focused. I thank my great friends David Ofori-Amoah, Hillary Child, Yaa Serwaa Karikari and Mohammad Amin Hashemian for always being there.

I am grateful for the staff of ChemMatCARS at Argonne National Laboratory for their support, especially Dr. Mrinal Kanti Bera who trained and inspired me with his high standards, humility and patience. I thank Dr. Wei Bu, a staff member of ChemMatCARS who helped me in taking and analyzing data. I thank Dr. Binhua Lin and Dr. Yu-Sheng Chen who gave me the opportunity of an extended stay at ChemMatCARS to learn from the experts during May-June 2017. I am grateful for the support and guidance of my Ph.D. committee members, Prof. Lewis Wedgewood, Prof. Ludwig Nitsche, Prof. Ursula Perez-Salas and Professor Vivek Sharma. These awesome and ambitious people gave me useful advice along my journey and inspired me in many ways.

TABLE OF CONTENTS

<u>CHAPTER</u>	<u>PAGE</u>
1 INTRODUCTION.....	1
2 REVIEW ON PROBING TECHNIQUES, INTERACTIONS AND SUBSTRATES FOR NANO-ASSEMBLY	7
2.1 Real Space and Reciprocal Space Imaging.....	7
2.2 Nano-assembly Interaction Energies.....	9
2.2.1 Competing Wetting.....	9
2.2.2 External Electric Field.....	11
2.2.3 Solvation Energy of Charged Nanoparticle.....	12
2.2.4 Effect of Ionic Size and Valence on Screening of Charged Nanoparticle.....	13
2.2.5 Cheerios Effect	15
2.2.6 Electro-capillary Charges	16
2.2.7 Screened Coulombic Interactions and Van der Waals Interactions	17
2.2.8 Motivation: Previous Study and Simple Calculation	18
3 MATERIALS AND METHODS	24
3.1 Gold Nanoparticles	24
3.2 Preparation of NaCl and BTPPATPFB Salts.....	25
3.3 Purification of 1, 2-dichloroethane (DCE)	26
3.4 Electrolyte Preparation	27
3.5 Making of Electrodes.....	28
3.6 Sample Cell.....	29
3.7 Determination of Potential of Zero Charge (PZC)	31
3.8 Quasi-elastic Light Scattering (QELS) Technique	34
3.9 Spectral Analysis of QELS from Liquid-Liquid Interface	36
3.10 Cyclic Voltammetry	38
4 X-RAY MEASUREMENTS	42
4.1 Liquid Surface Reflectometer.....	42
4.2 Momentum Transfer	45
4.3 GISAXS Measurements.....	46
4.3.1 Form Factor of Nanoparticles.....	47
4.4 X-ray Reflectivity (XR).....	49
4.4.1 Critical Wave Vector	50
4.4.2 Fresnel Reflectivity	53
4.4.3 Parratt Reflectivity	57
5 RESULTS AND DISCUSSIONS.....	61
5.1 Results of Interfacial Tension Measurement.....	61
5.2 GISAXS Measurements.....	64
5.3 XR Measurements.....	83
5.3.1 2D Spherical Nanoparticle Model Analysis.....	85
5.3.2 3D Spherical Nanoparticle Model Analysis.....	91

TABLE OF CONTENTS (Continued)

<u>CHAPTER</u>	<u>PAGE</u>
5.3.3 Slab Model	99
5.3.4 Proposed Structure of the 2D Spherical and 3D Slab Nanoparticle Models...	103
6 CONCLUSION	106
7 CHALLENGES AND FUTURE WORK.....	110
APPENDICES	113
VITA.....	180
REFERENCES.....	187

LIST OF TABLES

<u>TABLE</u>	<u>PAGE</u>
TABLE I. GIBBS ENERGY TRANSFER OF IONS FROM WATER TO DCE (94).....	40
TABLE II.FIT PARAMETERS OF 2D ARRAYS OF NANOPARTICLES WITH 60 nM NANOPARTICLE CONCENTRATION IN BULK WATER PHASE.....	89
TABLE III.FIT PARAMETERS OF 2D ARRAYS OF GOLD NANOPARTICLES WITH 35 nM NANOPARTICLE CONCENTRATION IN BULK WATER PHASE.....	90
TABLE IV.FIT PARAMETERS OF SLAB MODEL WITH 60 nM NANOPARTICLE CONCENTRATION IN BULK WATER PHASE.	101
TABLE V.FIT PARAMETERS OF SLAB MODEL WITH 35 nM NANOPARTICLE CONCENTRATION IN BULK WATER PHASE.	102

LIST OF FIGURES

<u>FIGURE</u>	<u>PAGE</u>
Figure 1. Inter-play of interactions forces between nanoparticle and the interface of water and DCE.....	10
Figure 2. Nanoparticle moving towards the interface under an external electric field.....	12
Figure 3. Adsorbed bubble at an interface with distorted meniscus near the wall	15
Figure 4. Forces acting on charged particles at an interface.	16
Figure 5. GISAXS image of 2D arrays of gold nanoparticle formed (62).....	19
Figure 6. XR data and fit b) Electron density profile from the fit (62).....	19
Figure 7. a) Nanoparticle initially on the water side b,c, d) Nanoparticle transporting to the DCE side of the interface (62).	20
Figure 8. a) TEM image of gold nanoparticles and b) the analyzed TEM image	24
Figure 9. The experimental set up of the glass cell and its auxiliary components.	30
Figure 10. Interfacial and bulk quantities of thermodynamics	32
Figure 11. Capillary surface fluctuation at the interface	34
Figure 12. Scattering from water/DCE interface and gratings	37
Figure 13. CV of 50 mM aqueous NaCl concentrations and 5 mM BTPPATPFB in DCE with a scan rate of 5 mV /s.....	39
Figure 14. : a) When ions move to the interface without crossing b) When ions (Na^+) begin to cross the interface	40
Figure 15. Schematic of the X-ray surface reflectometer for probing surfaces.	43
Figure 16. Momentum Transfer, Q	45
Figure 17. Bragg diffraction rods from ordered in-plane structures.....	46
Figure 18. X-ray reflectivity probing gold structure at water- 1,2 dichloroethane interface	49
Figure 19. S-polarized plane wave.....	51
Figure 20. a) Fresnel reflectivity (semi-log scale) as a function of wave vector, Q_z b) electron density of the Fresnel reflectivity for water and DCE bulk phase. An ideal interface is flat and hence the step function of the electron density.	56
Figure 21. Parratt reflectivity. Electron density varies along the perpendicular direction.	57
Figure 22. X-ray photons hitting a rough interface and scattered in diffused manner.....	59
Figure 23. Reflectivity from rough interfaces (non-ideal) of water and DCE normalized with Fresnel reflectivity b) Electron density profile of the corresponding reflectivity. In the absence of roughness, the electron density is a step function.	60
Figure 24. Interfacial tension measurements.	61
Figure 25. GISAXS measurements of 60 nM nanoparticle concentration in the bulk water phase as a function of interfacial potentials of a) 60 mV b) 40 mV c) 10 mV d) -40 mV. The appearance of the Bragg peaks is an indication of an ordered system at the interface. On the scale, 160 is equivalent to 2165 X-ray photo counts. Data taken with CCD detector.....	64
Figure 26. Lorentzian fit of the normalized integrated intensity along the vertical axis, Q_z with sample nanoparticle concentration 60 nM in the bulk water phase.....	66

LIST OF FIGURES (Continued)

<u>FIGURE</u>	<u>PAGE</u>
Figure 27. GISAXS measurements of 35 nM nanoparticle concentration in the bulk water phase as a function of interfacial potentials a) 60 mV b) 40 mV c) 10 mV d) -40 mV. The appearance of the Bragg peaks is an indication of an ordered system at the interface.	67
Figure 28. Integrated normalized GISAXS intensity fitted with Lorentzian functions and linear background along the vertical axis, Q_z with 35 nM nanoparticle concentration in the bulk water phase.	68
Figure 29. Integrated normalized GISAXS intensity fitted with Lorentzian functions and linear background along the vertical axis, Q_z with 35 nM nanoparticle concentration in the bulk water phase at negative potentials.	69
Figure 30. The nearest neighbour distance between nanoparticles with nanoparticle concentrations of 35 nM and 60 nM in the aqueous phase.	69
Figure 31. Coherence length as a function of interfacial potential.	71
Figure 32. Fitted normalized integrated intensities a) concentration of 60 nM nanoparticles in aqueous phase b) concentration of 35 nM nanoparticles in aqueous phase.	73
Figure 33. a) Form factors from fit b) Size distributions from fits.	74
Figure 34: Normalized intensity at interfacial potentials a) 10 mV and b) -40 mV of 60 nM nanoparticle concentration in bulk phase . The plots are on a logscale.	74
Figure 35. Fixed centers, $C(Q_{xy})$ b) Peaks from the fits of the integrated intensity at interfacial potential, 10 mV.	75
Figure 36. a) Fixed centers, $C(Q_{xy})$ b) Peaks from the fits of the integrated intensity at interfacial potential, 10 mV.	76
Figure 37. a) Peak centers versus fixed centers b) Area of peaks versus fixed centers	77
Figure 38. Fixed centers, $C(Q_z)$ b) Peaks from the fits at interfacial potential of 10 mV. ...	78
Figure 39. a) Fixed centers, $C(Q_z)$ b) Peaks from the fits at interfacial potential of 10 mV.	78
Figure 40. a) Peak centers versus fixed centers b) Area of peaks versus fixed centers at interfacial potential of 10 mV.	79
Figure 41. a) Fixed centers (Q_z) b) Area of peaks at interfacial potentials of -40 mV.	80
Figure 42. a) Peak centers versus fixed centers b) Area of peaks versus fixed centers at interfacial potential of -40 mV.	80
Figure 43. a) Fixed centers, $C(Q_{xy})$ b) Area of peaks at interfacial potential of -40 mV.	81
Figure 44. a) Fixed centers, $C(Q_{xy})$ b) Area of peaks at interfacial potential, -40 mV	81
Figure 45. a) Fixed centers, $C(Q_{xy})$ b) Area of peaks at interfacial potential, -40 mV.	82
Figure 46. a) Peak center versus fixed center b) Area of peak versus fixed center at -40 mV.	82
Figure 47. Fresnel (R_F) normalized reflectivity with a) 60 nM nanoparticle concentration in aqueous phase and b) 35 nM nanoparticle concentration in aqueous phase.	84
Figure 48. a) X-ray data and fit with 60 nM nanoparticle concentration in aqueous phase. b) Corresponding electron density profile from fit of 60 nM nanoparticle concentration in aqueous phase. c) X-ray data and fit with 35 nM nanoparticle concentration in aqueous phase. d) Corresponding electron density profile from fit of 35 nM nanoparticle concentration in aqueous phase.	89

LIST OF FIGURES (Continued)

<u>FIGURE</u>	<u>PAGE</u>
Figure 49. Mesh calculation of size versus depth (position).....	94
Figure 50. Mesh calculation of size of cluster versus depth (position) of single nanoparticle.	94
Figure 51. 3D model XR fit a) 60 nM nanoparticle concentration in bulk phase b) Corresponding electron density profile from the fit of the 60 nM nanoparticle concentration in bulk phase c) 35 nM nanoparticle concentration in the bulk phase d) Corresponding electron density profile from the fit of the 35 nM nanoparticle concentration in bulk phase.	95
Figure 52. a) X-ray reflectivity fit at interfacial potentials -40 and -90 mV of 60 nM nanoparticles in bulk phase b) Corresponding electron density from fit with nanoparticle's average size $\sim 10 \text{ \AA}$	97
Figure 53. Diffused assembly of single nanoparticles as clusters at the interface.....	97
Figure 54. a) XR reflectivity fit with a Gaussian depth distribution function of 60 nM nanoparticle concentration in the bulk aqueous phase. b) Corresponding electron density profile from fit.....	99
Figure 55. Slab model for XR analysis a) domain size, L1 b) domain size, L2	100
Figure 56. 3D slab model fit of a) 60 nM nanoparticle concentration in aqueous phase b) Corresponding electron density profile of the 60 nM nanoparticle concentration in aqueous phase. c) 35 nM nanoparticle concentration in aqueous phase d) Corresponding electron density profile of the 35 nM nanoparticle concentration in aqueous phase.	103
Figure 57. Coulombic interactions between charged nanoparticles and ions at the interface for the 2D structure transition to 3D structure.	104
Figure 58. Proposed model (side view) of the 2D HCP formed due to counter-ion enhancement on the DCE side of the interface.	105
Figure 59. Proposed model (side view) of the 3D structure formed due to counter-ion depletion on the DCE side of the interface	105

LIST OF ABBREVIATIONS

2D	Two Dimensional
3D	Three Dimensional
PB	Poisson-Boltzmann
BTTPATPFB	Bis(phosphoranylidene)ammonium tetrakis(pentafluorophenyl) borate
TPFB	Tetrakis(pentafluorophenyl) borate
TMA	Trimethylammonium
PEG	Polyethylene Glycol
CV	Cyclic Voltammetry
DCE	1,2 dichloroethane
GISAXS	Grazing Incidence Small Angle X-ray Scattering
XR	X-ray Reflectivity
DLVO	Derjaguin-Landau-Verwey-Overbeek
AFM	Atomic Force Microscope
QELS	Quasi-Elastic Light Scattering
PZC	Potential of Zero Charge
TEM	Transmission Electron Microscope
MD	Molecular Dynamics Simulation
SEM	Scanning Electron Microscope
NP(s)	Nanoparticle(s)
NaCl	Sodium Chloride
BTTPACl	Bis(triphenyl phosphoranylidene) ammonium chloride
LiTPFB	Lithium Tetrakis(pentafluorophenyl) borate

LIST OF ABBREVIATIONS (Continued)

ITIES	Interface between Two Immiscible Electrolyte Solutions
SERS	Surface Enhanced Raman Scattering
w/ NP	with nanoparticle
w/o NP	without nanoparticle

SUMMARY

Liquid interfaces play an important role in the development of novel devices. At the interface, arrays of nanoparticles can scatter coherently, absorb and emit light. The fluidity of the interface presents a novel environment for assembling nanoparticles in different configurations. In spite of the growth, interest, and potential in assembling nanoparticles at the liquid-liquid interface, nanoparticle adsorption at a liquid-liquid interface is poorly understood.

It is evident from theory, simulation and experiment that the description of electrostatic and van der Waals forces contained within the DLVO theory is inadequate to explain the adsorption and stability of nanoparticles at a liquid-liquid interface. Instead, the interactions of nanoparticles at a liquid-liquid interface are governed by hydration forces, capillary forces, electrostatic correlations and long-range dipole interactions due counterions, among others.

In this study, we use an electrochemical technique to remotely tune interfacial interactions between nanoparticles at a liquid-liquid interface between water and 1,2-dichloroethane electrolyte solutions. We demonstrate the formation of a 2D array of nanoparticles. X-ray measurements revealed that further tuning of the interfacial potential changed the 2D arrays to 3D clusters of nanoparticles. The X-ray measurement techniques used were X-ray reflectivity (XR) and grazing incidence small angle X-ray scattering (GISAXS) to probe the out-of-plane and in-plane interfacial structures.

CHAPTER 1

INTRODUCTION

Self-assembled structures made from nanoscale materials are important scientifically and technologically. Next generation devices fabricated from nanoscale materials have applications in the areas of optical mirrors (1, 2), drug delivery systems for cancer treatment (2, 3), membranes for separation technology (4), biochemical sensing (5), solar energy harvesting (6), and optics such as self-healing mirrors (7), anti-reflecting substrates (8), and plasmonic rulers (9).

Nanomaterials, defined as materials having at least one dimension in the range of 1-100 nm have properties different from their bulk materials due to finite-size quantum effects (10). These quantum effects influence the structural, optical, electrical and magnetic properties of nanomaterials. Their relatively large surface area to volume ratio compared with bulk materials make them more chemically reactive (11-13).

The ability of nanoparticles to scatter, absorb and emit light at interfaces has been exploited in the manufacture of optical devices and biosensors that use colorimetric (14, 15) and surface enhanced Raman scattering (SERS) (16-18). For example, in SERS, arrays of nanoparticles create local hotspots of electric fields. The presence of analyte molecules in the local hotspots enhances the emission of certain wavelengths, which are fingerprints of the analytes. Liquid interfaces play a role in the development of these devices since nanoparticles are often prepared and stabilized as colloids.

Nanoparticles adsorbed at a liquid-liquid interface were first reported by Pickering and Ramsden (19, 20). Recently, studies of nanoparticles at liquid-liquid interfaces have demonstrated concepts that can be explored as an alternative route to making functional devices. A liquid-liquid interface is formed when two immiscible electrolytic solutions (ITIES) are brought into contact; hydrophilic salt is dissolved in the water phase and hydrophobic salt in the organic phase. Back-to-back electrical double layers, one in each phase, are formed on either side of the interface. The potential drop is localized in the region of the double layers (21-23).

The assembly of nanoparticles at a liquid-liquid interface is cheap, fast, and reproducible, making it suitable for technological applications. In most cases, uncharged dielectric (24) and metallic nanoparticles (25-27) capped with organic molecules are used. The assembly of NPs at liquid-liquid interfaces does not need sophisticated engineering; the interfaces are self-healing, robust, and the structure can be easily reformed from dissolved nanoparticles in the bulk phases (28). The optical transparency of oil and water used for liquid-liquid studies, combined with the mechanically flexible nature of the interface, make it attractive for colloidal assembly (29, 30). The mechanical flexibility of the interface provides a platform to form varying geometries from planar sheets (31, 32) to curved lenses (33) and three dimensional objects coated with nanoparticles (32, 34). The interfacial nanoparticles are accessible to chemical species introduced into the bulk phases.

While liquid-liquid interfaces can provide an opportunity for transformative discoveries and applications, the adsorption of nanoparticles at a liquid-liquid interface is poorly understood. It is evident from theory (24, 35), simulation (36-38), and experiment (39-41) that the description of electrostatic and van der Waals forces in the DLVO theory used to describe colloidal solutions is not enough to explain the adsorption, stability and equilibrium position of nanoparticles at the

liquid-liquid interface. Instead, the interactions of nanoparticles at a liquid-liquid interface are governed by interfacial tension stabilization (1), hydration or solvation forces due to immersion of nanoparticles at the interface (42), capillary forces due to deformation of the interface (43) and long range-dipole interactions due counterions. While uncharged nanoparticles can spontaneously adsorb at the interface, charged nanoparticles may require an initial driving force to facilitate their adsorption and ordering at the interface.

Techniques for inducing interfacial adsorption include the addition of ethanol to the interface (44), centrifugation (9), electrochemical methods (23, 45), and controlled evaporation of solvents. These techniques have been used to form long-range close-packed assemblies of nanoparticles (39). On the other hand, spontaneous self-adsorption is more convenient than induced adsorption; however, it is limited by the diffusion time of the nanoparticles. Once adsorbed to the interface, interactions between nanoparticles can be remotely tuned by an external electric potential (23, 42, 45, 46), pH (29, 39, 47, 48), and ionic strength (9, 49) .

Turek et. al. used centrifugal force to adsorb a passivated gold nanoparticle with a 16 nm core diameter to a water/1,2-dichloroethane interface (9). Variable spacing of 4.5 to 35 nm between the nanoparticles was achieved by varying the pH and salt concentration of the aqueous phase. Nanoparticle adsorption and desorption to the interface was characterized by measuring the localized surface plasmon resonance (LSPR) shift in the bulk phase and at the interface. The study revealed a significantly tunable array of gold nanoparticles. In both cases, plasmon shifts were attributed to a variation in nanoparticle spacing in the bulk and at the interface. Adjustment of pH with HCl and NaOH modulated the surface charge density of the passivated nanoparticles, thereby reversibly increasing and decreasing the spacing between nanoparticles.

Pioneering work on electrochemical adsorption of charged gold nanoparticles ($\sim 1.5 \pm 0.4$ nm gold core diameter) by Girault's group showed a reversible voltage-tunable nanoparticle density at a water/1,2-dichloroethane interface (23). By measuring the potential dependent interfacial tension at the interface, the calculated excess surface charge revealed a reversible modulation of gold nanoparticle density at the liquid-liquid interface.

Schlossman's group demonstrated the formation of a 2D array of charged nanoparticles whose lattice spacing was reversibly tuned between 6 and 7 nm by varying an external electrochemical potential from -130 to +180 mV across the interface (45). In this study, passivated gold nanoparticles of 2 nm core diameter were studied at a water/1,2-dichloroethane interface. The study discovered that ion correlations between charged nanoparticles and counterions played an important role in the assembly process. Understanding effects of ion correlation such as ion condensation, overcharging, among others, can bring transformative and alternative route to nanoparticle assembly at a liquid-liquid interface. The X-ray study probed the direct interfacial coverage of nanoparticles and the interfacial position of nanoparticles as a function of interfacial potential.

Edel's group studied electrochemical adsorption and tunability (3-20 nm spacing) of 16.1 nm passivated gold nanoparticle at a water/1,2-dichloroethane interface using LSPR measurements and by visual observation. The potential dependent LSPR measured was consistent with changes in the colorization observed at the interface (50). Edel's group also exploited the plasmonic properties of assembled gold nanoparticle (~ 43 nm Au core) arrays for trace analyte detection at a water/1,2-dichloroethane interface (16). By assembling nanoparticles in an array, hotspots of local electric fields were created and the presence of trace molecules near the hotspots caused the molecules to emit light measured with surface enhanced Raman scattering (SERS). Each trace

analyte studied had a unique SERS fingerprint corresponding to the chemical nature of the analytes and the affinity of analytes to the gold nanoparticles. Additional study detected the presence of mercury, Hg(II), with arrays of gold nanoparticles, as well as polyatomic ligands (51). The study demonstrated the versatility of the liquid-liquid interface in detecting different ligands and Hg(II). Visual, SERS, and LSPR measurements established a proof of concept for a voltage, pH, and ionic strength tunable assembly of nanoparticles at a liquid-liquid interface, indicating the potential to make functional devices such as electro-variable mirrors, optical filters, biochemical sensing devices, among others. The studies provided insight into the mechanism that controlled the spacing of nanoparticles within the array, which can be exploited to vary with plasmonic properties of the interfaces.

In this study, we use synchrotron X-ray techniques to demonstrate the formation of 2D arrays and 3D clusters of gold nanoparticles at a liquid-liquid interface by electrochemical techniques. Nanoparticle clusters have different plasmonic properties than single-nanoparticle arrays. Among the questions we address: What are the driving forces for the formation of 2D and 3D nanoparticle structures? What is the effect of bulk nanoparticle and electrolyte concentration on the equilibrium interfacial structure, position and coverage of the nanoparticles? We remotely control the screening of heavily charged nanoparticles by changing the local electric field around the nanoparticles with an external electric field. It has been established that a planar object in contact with an electrolyte solution can experience condensation of counter-ions on its surface, leading to the screening of heavily charged planar objects (52, 53). It is therefore reasonable to expect more nanoparticles to adsorb at the interface due to screened electrostatic repulsive forces.

Using 50 mM NaCl in aqueous phase and 5 mM BTPPATPFB in DCE phase, we stabilized a gold nanoparticle array at the water/DCE interface. The nanoparticles have a 2 nm diameter gold

core coated with one hundred ligands whose terminal endgroup is a positively charged trimethyl ammonium (TMA). Our X-ray measurements revealed potential dependent tunable 2D and 3D structures on the DCE side of the water/DCE interface. The 2D structures were formed at interfacial potentials of 60 mV and 40 mV while the 3D structures were formed at interfacial potentials of 10 mV and below. Our X-ray reflectivity and GISAXS analyses showed that the 2D structure is a hexagonal close-packed lattice (HCP) of single gold nanoparticles. XR and GISAXS analyses showed that the 3D structure is a non-spherical gold nanoparticle cluster whose form factor is consistent with a pyramidal form factor. The X-ray and GISAXS analyses also showed that increasing the bulk concentration of nanoparticles changed the interfacial adsorption of nanoparticles and their spacing. By investigating the structure of adsorbed nanoparticles at the interface as a function of applied interfacial potential and bulk concentration, we gained insight into the mechanism and driving forces leading to the formation of 2D and 3D nanoparticle structures.

CHAPTER 2

REVIEW OF PROBING TECHNIQUES, INTERACTIONS AND SUBSTRATES FOR NANO-ASSEMBLY

Nanoscale assembly structures have been formed on several different types of substrates in recent times. Examples are air-solid, solid-liquid, air-liquid and liquid-liquid interfaces. Fixed arrays of nanoparticles have been formed on solids. Protein cages (54) and DNA (55) templates are widely used in assembling 2D and 3D structures in different geometric shapes, such as trigonal, tetrahedral, and pyramidal structures. The liquid-liquid interface can be exploited to assemble nanoparticles cheaply and simply, producing mechanically flexible, self-healing arrays that can be accessed by light from either side of the array, which can also interact with either hydrophilic or hydrophobic chemical species.

2.1 Real Space and Reciprocal Space Imaging

Imaging tools such as atomic force microscopy (AFM), transmission electron microscopy (TEM), nuclear magnetic resonance (NMR), optical microscopy, scanning electron microscopy (SEM) and X-rays have been used to investigate nanoparticle systems. These tools measure physical parameters, for example, concentration, surface area, length, tissue parameters in biological systems (56)..

Spatial resolutions and acquisition frequency of imaging techniques have improved over the years providing the ability to probe sub-nanometer length scales in validating established computation models. For example, models describing the activity of protein interactions and

biochemical signaling networks (56-58). SEM and optical microscopy yield an accurate image of a surface but cannot provide quantitative information about surface roughness (59). Surface roughness provides information, for example on particle-particle separation. AFM provides quantitative roughness and height measurements of surfaces with a good lateral resolution of 1 nm and vertical resolution of 1 Å (60, 61). However, AFM measurement is slow and probes only small area (59). Light scattering has been used to study particle sizes. It is non-destructive. In literature, a number of theories have been established for the study of particles with light scattering. However, those theories may be valid under some specific conditions, different from experimental conditions. Light scattering measurements are often performed in conjunction with other techniques (62).

Electrical capacitance (63, 64), optical reflectivity (1, 9, 65), and X-ray techniques (45, 66) have been used in recent times to characterize the structure of nanoparticles at liquid interfaces. The X-ray technique is non-destructive and measures averages of parameters over a large area of a sample. It can operate in different environmental conditions from ultra-low to ultra-high pressure and can discriminate many different elements in a sample. It can access buried interfaces and probe different morphologies. However, probing nanometer and sub-nanometer length scales require synchrotron radiation (highly collimated X-ray source) due to low signals from the surface, which scales with the size of the nanoparticles. Information provided by X-rays is in reciprocal space and has to be translated into real space, which requires modeling. It is also difficult to discriminate a single nanoparticle from other nanoparticles due to the X-ray beam size, divergence and X-ray optical limitations.

2.2 Nano-assembly Interaction Energies

A number of forces play a role in the equilibrium position of the nanoparticles. For example, capillary charges, electrostatic interactions, cheerios effect, thermal energy capillary arrest, van der Waal's interactions, etc. These interacting forces at the interface will be discussed in the following sections.

2.2.1 Competitive Wetting

The driving force for the adsorption of particles to an interface is the decrease in interfacial energy, which depends on the three-phase contact angle. The maximum gain of interfacial energy occurs when the contact angle is 90 degrees. The interfacial adsorption energy of micrometer-sized particles is usually 10^6 kT, making the particle effectively stuck at the interface (67). For a nanometer-sized particle, the gain in energy is comparable to thermal energy (kT), which can detach the particle from the interface into the bulk. A small deviation of the 3-phase contact angle from 90 degrees can prevent nanoparticles from adsorbing to the interface. Wetting experiments have shown that an approximately 90 degree three phase contact angle is required to stabilize layers of gold and silver nanoparticles at an interface (68, 69). It has also been shown that a 3 nm CdSe at water/toluene interface is spontaneously replaced by a 5 nm CdSe nanoparticle (70, 71).

Considering the uncharged particle shown in Figure 1. The position of the nanoparticle at the oil-water interface is dominated by its ability to reduce the interfacial energy. When the particle adsorbs to the interface, it pierces the interface to reduce the interfacial energy. Therefore, energy is “gained” by interfacial adsorption. If $\gamma_{p,o} < \gamma_{p,w} + \gamma_{w,o}$ and the particle is hydrophilic, the particle will move to the water side of the interface in order to remove some contact area from the

oil side. If $\gamma_{p,o} < \gamma_{p,w} + \gamma_{w,o}$ and the particle is hydrophobic, then it will localize on the oil side but still pierce through the interface to reduce the water/oil interface's energy (42).

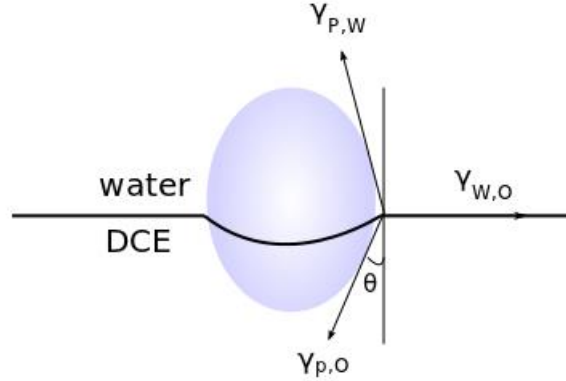


Figure 1. Interplay of interaction forces between nanoparticle and the interface of water and DCE.

For a particle of radius R and interfacial energy between the water-oil, nanoparticle-oil and nanoparticle-water $\gamma_{w,o}$, $\gamma_{p,o}$ and $\gamma_{p,w}$ respectively, the interfacial energy gained, ΔE when the particle is located at the interface is (72):

$$\Delta E = -\pi R^2 / \gamma_{w,o} \left(\gamma_{w,o} - (\gamma_{p,o} - \gamma_{p,w}) \right)^2 \quad (2.2.1.1)$$

From the Young-Laplace equation, $\gamma_{p,o} - \gamma_{p,w} = -\gamma_{o,w} \cos \theta$, (42), the equation (2.3.1.1) reduces to $\Delta E = -\pi R^2 (1 - \cos \theta)^2$. Due to ionic screening on the charged nanoparticle, the free energy of formation of the double layer changes the surface free energy of the charged nanoparticle (73), $\gamma_{P1} = \gamma_{P,0} + \Delta F_{DL}$ where γ_{P1} is the interfacial energy of the nanoparticle due to coulombic screening, $\gamma_{P,0}$ is the interfacial energy of the nanoparticle at zero charge and ΔF_{DL} is the free

energy due to ionic screening. By substituting $\gamma_{P1} = \gamma_{P,0} + \Delta F_{DL}$ into the Young-Laplace contact angle, $\cos \theta_{new} = \cos \theta - \frac{\Delta F_{DL}}{\gamma_{w,o}}$. Since the ionic screening is spontaneous, this implies $\Delta F_{DL} < 0$ and therefore, the contact angle for the charged nanoparticle, θ_{new} is smaller than the contact angle of the uncharged nanoparticle, θ . Although the applicability of the laws of macroscopic capillarity at the nanoscale could be questioned, several experimental and molecular dynamics (MD) simulations have observed an extension of the wetting properties from their macroscopic states to microscopic states (36, 74, 75).

2.2.2 External Electric Field

A voltage drop across an oil/water electrolytes interface will cause repositioning of ions between the bulk phases and the interface., which can destabilize or stabilize nanoparticles at the interface. For example, if a positively charged nanoparticle is in the bulk water phase and a positive potential drop is applied across the interface, the nanoparticle would be pushed towards the interface under the applied electric field. However, solvation and interfacial tension will also act in the direction opposite to the applied electric field and could prevent nanoparticle penetration into the oil phase (42). If the electric field is greater than the solvation energy and the interfacial tension, then the nanoparticle will move to the oil side of the interface. Otherwise, it would stay on the water side of the interface if the effects of solvation and the interfacial tension dominated. Figure 2 is a cartoon of a nanoparticle attracted to the interface under an external potential. Without the external field, the solvation energy of charged nanoparticles repel charged nanoparticles from the organic phase. The role of the electric field is to cause ion enhancement, which can stabilize or destabilize the nanoparticles at the interface. For example, a positively charged nanoparticle in the water bulk phase under a positive potential drop would be attracted to the interface by counter-

ions on the oil side. If the interfacial potential is reversed where co-ions instead of counter-ions are enhanced on the oil side of the interface, then the charged nanoparticles would be repelled from the interface.

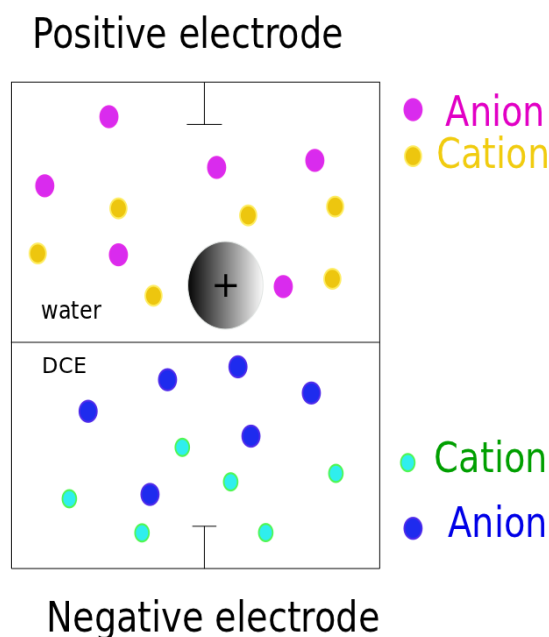


Figure 2. Nanoparticle attracted to the interface under an external electric field.

2.2.3 Solvation Energy of Charged Nanoparticle

Bare metal nanoparticles are often passivated with a ligand which can hydrolyze (deprotonate) in water to stabilize the particle-particle interactions. For example, it is expected that a carboxylic (-COOH) terminal ligand can deprotonate in water giving rise to high charge density on the surface of the nanoparticle. The solvation energy scales as z^2 where z is the number of deprotonated charges on the surface of the nanoparticle (42). When the nanoparticle is moved into a high permittivity medium, for example, water, the effective charge on the nanoparticles, z will decrease. The solvation energy is therefore significantly reduced due when moving from oil to water side of

the interface (42). The effect of solvation energy in moving a particle from oil to water side of the interface can give a different ordering based on electrostatic interactions.

2.2.4 Effect of Ionic Size and Valence on Screening of Charged Nanoparticle.

The size and valence of ions in an electrolyte solution play important roles in the screening of the charged nanoparticle. There is experimental evidence of the role of size in electrostatic interaction between the counter-ions and the heavily charged nanoparticles (76). Dishon et al. provided experimental evidence of ion specific interactions with negatively charged silica particles in solutions. They discovered that given NaCl, KCl and CsCl, NaCl created a repulsive environment between the charged silica particles while KCl and CsCl created attractive environment. It was concluded that ion specific adsorption was favorable for relatively larger cations, thereby justifying why Na^+ did not adsorb onto the surface of the silica particles (77).

Ion specific adsorption was correlated with the solvation properties of the ions and the free energy cost associated with partial or full dehydration of the adsorbing cations on the surface of the silica particles. The driving force for the ions accumulating on the surface of the charged silica was due to increased competing osmotic pressure (concentration gradient) of the ions in the solution and ion hydration in the bulk. Thus, while hydration forces favor ions remaining in the aqueous solutions, osmotic pressure drove the salts from the solution to the surfaces of the charged silica particles (76). It was observed that beyond the neutralization point where the charged silica particle surfaces were slightly overcharged positively charged ions continued to adsorb at the surface of the charged silica particles, indicating that the driving force between silica particles and counter-ions was beyond coulombic interaction. Thus, hydration and osmotic pressure played an important role. Hydration is favorable for high charge densities. Hence, smaller and divalent

charges have higher hydration energy and will prefer to stay in solutions rather than adsorb on the charged silica particles. On the contrary, between divalent and trivalent charges, it was observed that an additional force of interaction between the charged silica and the trivalent existed making the trivalent ion favorably adsorbed on the surface of the silica particles showing an anomalous role in the size and charge of counter-ions around a heavily charged particle.

Colloids and capillary forces combine to form a high energy barrier due to a significant change in energy landscape when a large particle replaces small molecules at a liquid-liquid interface. For molecular size l the interfacial energy landscape scales with kT/l^2 where k is Boltzmann constant and T is temperature. The change in interfacial energy ΔU for a colloidal particle of size R replacing the solvent is, $\Delta U/kT \approx (R/l)^2$. This explains why capillary forces and colloids combine to form metastable states which can induce different forms of ordering at a liquid interface (78). The free energy gained, $-\Delta U$ is relatively large compared with thermal energy kT (79). The metastable state of the adsorbed nanoparticle at the interface under certain conditions can cause precipitation of the particles. For example, precipitation has been observed in anisotropic phase of solvents when colloidal particles were in metastable states (78, 80) .

2.2.5 Cheerios Effect

The so-called “Cheerios effect” is a capillary phenomenon which induces aggregation of microparticles at an interface. A typical case is a floating bubble on an air/water (medium 1 and 2) in a vessel as in Figure 3.

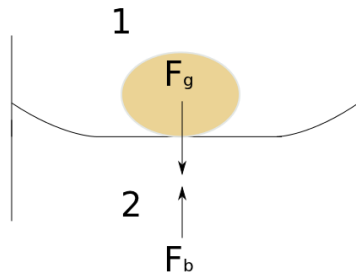


Figure 3. Adsorbed bubble at an interface with distorted meniscus near the wall

The wall of the vessel distorts the interface forming a meniscus. This induced meniscus at the interface causes an aggregation of the bubbles at the interface. Considering the weight of the bubble, the particles will experience net buoyancy force. If the particle is constrained to stay at the interface, the buoyancy force, F_b will cause the particles to move upwards along the curved meniscus to the edge of the vessel. This motion towards the wall appears as if there is an attractive force between the wall and the particle when in reality, the buoyancy force causes the particle to move along the curved meniscus towards the wall (81). This effect is responsible for the accumulation and aggregation of bubbles and other micro particles at interfaces. On a nanometer length scale, however, the weight of the nanoparticle is insignificant (scales as R^3) for a sphere of radius R and the cheerios effect becomes negligible.

2.2.6 Electro-capillary Charges

Particles attached to an interface between a polar solvent (water) and non-polar solvent (oil) can experience the following forces: electro-dipping force (82), direct electric repulsion between the charged particles (83, 84) and electric field induced capillary attraction (85).

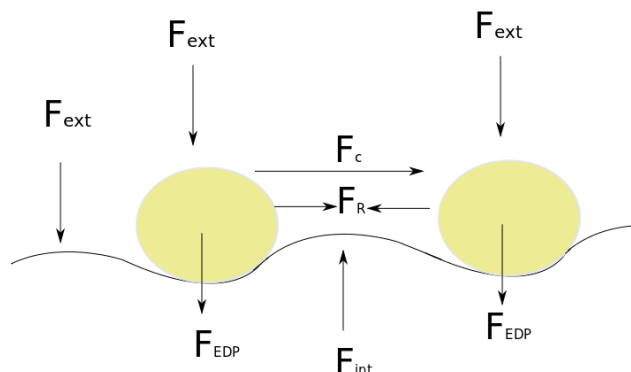


Figure 4. Forces acting on charged particles at an interface.

The electro-dipping force, F_{DP} , normal to the interface is an electrostatic image charge effect which pushes the particles into the lower phase (86, 87). The particles see image charges on the other side of the interface, which can cause attraction or repulsion depending upon the relative permittivities of the two phases. A force imbalance between the electro-dipping force and the interfacial energy will cause interfacial distortion. This interfacial distortion in Figure 4 can lead to capillary attractive force at the interface. The direct repulsion, F_R , is due to the electrostatic repulsion between like charges of the nanoparticles. The capillary attraction, F_c , is due to the deformation of the interface from the particle causing attraction between dimples formed at the interface (85).

2.2.7 Screened Coulombic Interactions and van der Waals Interactions

Counter-ions screen the bare charges of nanoparticles leading to reduction in the electrostatic repulsive energy of the two like charged nanoparticles. The electrostatic interaction energy, U_C , between two particles in a bulk solvent is given by (88)

$$U_C = 64\epsilon_r\epsilon_o a/2 \left(\frac{kT}{e} \right)^2 \gamma^2 e^{-\kappa s} \quad (2.2.7.1)$$

where ϵ_r is the relative permittivity, ϵ_o is the permittivity of free space, k is Boltzmann's constant, T is the temperature in K , e the charge of electron. The reciprocal Debye length, $\kappa = 1/D_B$ (88):

$$\kappa = \sum_i \sqrt{\frac{(8\pi c_i e^2 z_i^2)}{(\epsilon\epsilon_r k_B T)}} \quad (2.2.7.2)$$

Where $z_i e$ is the charge on an aqueous ion of valence z_i and c_i is the ion concentration in m^{-3} . The variable γ is determined by the surface potential, ψ , using $\gamma = \tanh[(e\psi)/(4k_B T)]$. The surface potential can be calculated from the surface charge density σ of the particle using the Grahame equation (88):

$$\psi = \frac{k_B T}{(2ze)} \sinh^{-1} \left(\frac{\sigma}{\sqrt{8k_B T c \epsilon \epsilon_o}} \right) \quad (2.2.7.3)$$

The non-retarded van der Waals interactions between identical spheres of radius R and separation distance s is given by (89):

$$U_{vdW} = -\frac{A}{6} \left[\left(\frac{2R^2}{s^2} + 4RS \right) + \left(\frac{2R^2}{s^2} + 4RS + 4R^2 \right) + \ln \left[\frac{s^2 + 4RS}{s^2 + 4RS + 4R^2} \right] \right] \quad (2.2.7.4)$$

where A is the Hamaker constant of the particle. Based on the classical Derjaguin-Landau-Verwey-Overbeek (DLVO) theory of colloidal behavior, the competing forces are the long-range electrostatic and short-range van der Waals interactions. Within DLVO theory, particles of like charge are stabilized against aggregation by their mutual long-range electrostatic repulsive forces. In some solution conditions, this electrostatic repulsive energy barrier, which prevents aggregation, can be overcome leading to cluster formation.

2.2.8 Motivation: Previous Study and Simple Calculation

Our previous study on the assembly of arrays of charged nanoparticles at a water/1,2-dichloroethane interface focused on interfacial potentials in the range -130 mV to 180 mV. A 2D array of gold nanoparticles was formed on the DCE side of the interface using 5 mM aqueous NaCl and 5 mM BTPPATPFB in DCE. Figures 5 and 6 show the GISAXS and XR results of the previous study.

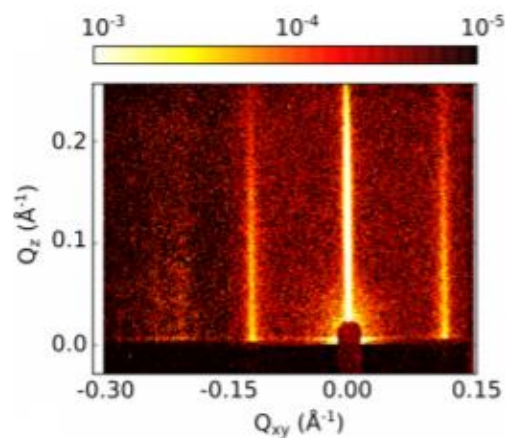


Figure 5. GISAXS image from 2D arrays of gold nanoparticle (62).

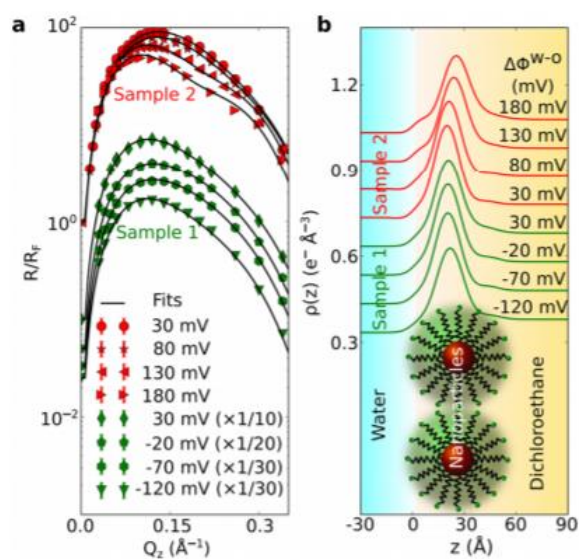


Figure 6. a) XR data and fit; b) electron density profile from the fit (62).

Figure 5 shows a GISAXS measurement of the two dimensional (2D) hexagonal close-packed (HCP) diffraction rods. X-ray reflectivity (XR) in Figure 6 shows that the nanoparticles transported from the bulk water phase to the DCE side of the interface. MD simulation results supported this observation as shown in Figure 7.

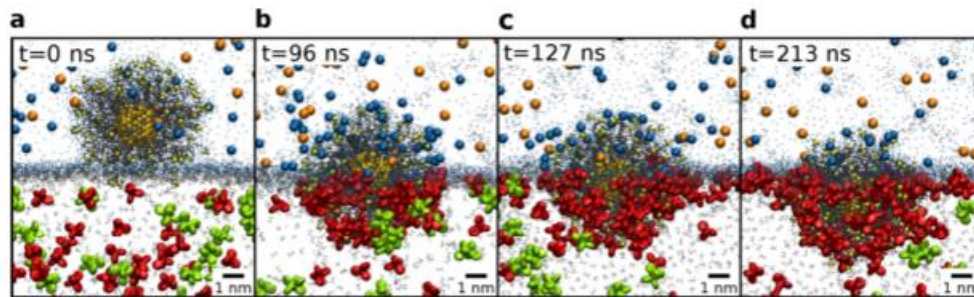


Figure 7. a) Nanoparticle initially on the water side b,c, d) Nanoparticle transporting to the DCE side of the interface (62).

Our current system is a 50 mM aqueous NaCl concentration and a 5 mM BTPPATPFB in DCE using interfacial potentials from 60 mV towards -190 mV. The goal is to stabilize the nanoparticles on the water side of the interface by enhancing the electrostatic potential energy of the nanoparticles on the water side of the interface. In our previous study, even though, the nanoparticles were initially in the water phase, on applying an external field, the electrostatic correlation between the nanoparticles and the counter-ions on the DCE side of the interface facilitated the transport of the nanoparticles to the DCE side of the interface. Our simple calculation showed that ~ 7 mM NaCl and 5 mM BTPPATPFB in DCE should be enough to stabilize the nanoparticles on the water side of the interface if electrostatic correlations and entropy are neglected.

The relative permittivity of water, ϵ_r is ~ 80 and that of DCE is ~ 10 and the electrostatic correlation energy (E_r) scales as, $E_r \propto 1/\epsilon_r$. To account for entropy and electrostatic correlations, we could replace the DCE with a higher permittivity medium for example, nitrobenzene.

Alternatively, the concentration of the bulk water solution can be increased. This will change the electrostatic potential energy of the nanoparticle in water and compensate for the stronger electrostatic correlation from the DCE side of the interface.

We propose an increased bulk water concentration since it will be easier to compare the results with our previous study. We have done preliminary estimation on the electrostatic potential energy of the system and found that given the relative dielectric of water and DCE to be ~ 80 and 10 respectively, the electrostatic potential energy will be equal ($U_{\text{DCE}} = U_{\text{H}_2\text{O}}$) for nanoparticles if 5 mM BTTPATPFB in DCE and ~ 7 mM NaCl in water were maintained. Beyond the 7 mM NaCl in water -while maintaining the same conditions in the oil phase-one would expect the nanoparticles to localize on the water side of the DCE. This is the case when electrostatic correlations and entropy are not considered. The Debye length, λ_D of an ionic cloud around a charged nanoparticle is estimated as:

$$\lambda_D = \frac{1}{\sqrt{8\pi l_B I}} \quad (2.2.8.1)$$

Where I is the molar ionic strength and l_B is the Bjerrum length. The molar ionic strength, $I = 1/2 \sum_i c_o z_i^2$ arises from Debye-Huckle theory which is a result of linear approximation of the Poisson-Nernst-Planck equation for small voltages (90). The Bjerrum length, l_B , is the length scale at which electrostatic interactions between ions is comparable to thermal energy, kT of the bulk medium. For a monovalent ion with a magnitude of charge, q , in a relative dielectric medium of solution, ϵ and Bjerrum length, l_B , $kT = \frac{q^2}{4\pi\epsilon l_B}$. Then, $l_B = \frac{q^2}{4\pi\epsilon kT}$. The electrostatic potential energy, U_E of the charged nanoparticles by the ionic cloud around the nanoparticles is given as:

$$U_E = 1/2 \frac{\sigma^2 \lambda_D}{\epsilon} \quad (2.2.8.2)$$

The charge density of the nanoparticle, σ , is the total number of charges per unit area of the nanoparticle. Given the relative dielectric of water and DCE as 80 and 10 respectively for a spherical gold nanoparticle, then:

$$\frac{U_o}{U_w} = \frac{\lambda_{D,o} \epsilon_{r,w}}{\lambda_{D,w} \epsilon_{r,o}} \quad (2.2.8.3)$$

Where U_o and U_w are the electrostatic potential energies of the nanoparticles in the DCE and water phases respectively. The parameters, $\epsilon_{r,w}$ and $\epsilon_{r,o}$ are the relative dielectric constants of water and organic phases, $\lambda_{D,o}$ and $\lambda_{D,w}$ are the Debye lengths of the ionic clouds around the nanoparticles in the DCE and water phases respectively. For the electrostatic potential energy to be the same for both water and DCE phase,

$$\frac{\epsilon_{r,o}}{\epsilon_{r,w}} = \frac{\lambda_{D,o}}{\lambda_{D,w}} = \sqrt{\frac{l_{B,w} C_w}{l_{B,o} C_o}} \quad (2.2.8.4)$$

The parameters, C_o and C_w are the concentrations of salts in the organic and aqueous phases, $l_{B,w}$ and $l_{B,o}$ are the Bjerrum lengths in the water and organic phases respectively. Given a monovalent symmetric salt BTTPATPFB in DCE whose charge in the organic solvent is ± 1 and 1 electronic charge to be equal to 1.69×10^{-19} C, relative dielectric of organic solvent, $\epsilon_{r,o} \approx 10$, permittivity of air, $\epsilon_o = 8.85 \times 10^{-12}$ F/m, Boltzmann constant, $k_B = 1.38 \times 10^{-23}$ J/K, then, $l_{B,o} \approx 6.2 \text{ nm} = 62 \text{ \AA}$.

If we consider the dissociation of the BTPPATPFB to be 58 % (91), then the ionic strength, I , of BTPPATPFB in DCE reduces by a factor of $(0.58)^2$. This dissociation factor scales the Debye length of the nanoparticles in organic phase by a factor of 1.72. Similarly, for a symmetric salt, NaCl in water of relative dielectric, $\epsilon_{r,W} \approx 78$, $l_{B,W} \approx 0.8 \text{ nm} = 8 \text{ \AA}$. The NaCl salt is completely dissociated in water. Substituting the defined parameters into equation (2.3.9.4) gives $\frac{c_w}{c_o} = 1.72$. Hence, for a 5 mM BTPPATPFB in DCE, 7 mM of NaCl is required to keep the same electrostatic potential between the water and DCE. However, this simple calculation does not account for the entropic contributions in the water and DCE phase. It does not also account for the electrostatic correlation. Again, the assumption of diffused double layer is not valid in the DCE phase as MD results showed that the counter-ions condense heavily condensed on the nanoparticles. It is no longer a diffused double layer in the oil phase. We propose the following:

- i) Use 50 mM NaCl in place of the 5 mM NaCl while maintaining the 5 mM BTPPATPFB in DCE used previously. By this, we expect the nanoparticles to form a 2D array on the water side of the interface. Our preliminary measurement with 20 mM NaCl did not show significant change in the GISAXS and reflectivity measurements compared with our previous study. We therefore study our system with 50 mM NaCl instead. Beyond 50 mM, we saw instability and precipitates.

We propose the formation of cluster at the interface. Cluster formations were observed in our previous study at certain negative potentials. We will explore a broader range of the negative interfacial potentials.

CHAPTER 3

MATERIALS AND METHODS

3.1 Gold Nanoparticles

The gold nanoparticles used in this study consist of a 2 nm diameter gold core bound to a thiol (S), hydrocarbon chain, a polyethylene glycol chain and a trimethylammonium terminal moiety (TMA) – $\text{Au}-(\text{S}(\text{CH}_2)_{10}(\text{CH}_2\text{OCH}_2)_4\text{CH}_2\text{N}^+(\text{CH}_3)_3)_{100}$. Figure 8a is a transmission electron microscope image of the gold core nanoparticles.

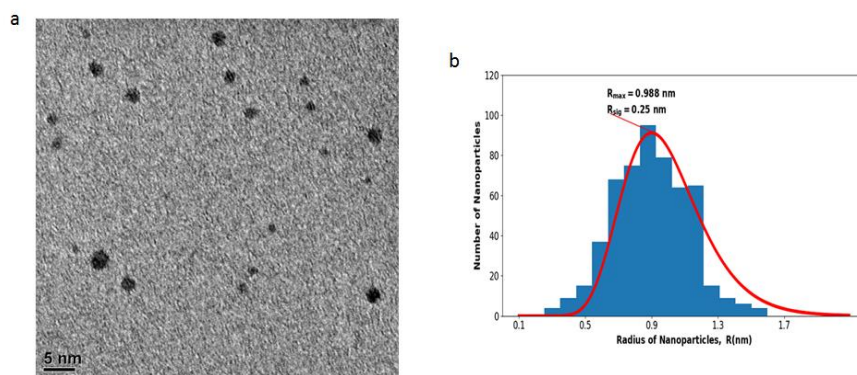


Figure 8. a) TEM image of gold nanoparticles and b) the analyzed TEM image

The total length of the nanoparticle including the ligand is ~ 6 nm. The hydrocarbon part of the ligand provides steric repulsion and the trimethylammonium (TMA) provides electrostatic repulsion. The polyethylene glycol (PEG) stabilizes the ligand in water by adsorbing water molecules so that the ligand does not shrink in water. The methodology used in making the nanoparticles has been described in details by Moyano et al. (92, 93).

The transmission electron microscopy (TEM) was performed at the research resources center, UIC. The TEM is a 300 kV transmission electron microscope with a LaB6 electron source. It collects

images using a Gatan Orius SC200 CCD Camera (2K x 2K) with Windows XP computer running a digital micrograph software, which is capable of recording in-situ events at a TV rate and high-resolution images. Small amount of the gold nanoparticles was diluted in water. The dilution is discontinued when the nanoparticle solution becomes colorless. This is to ensure that the nanoparticles are separated from each other and only a 2D nanoparticle is resolved. A portion of the diluted nanoparticles is deposited on a holey carbon-grid and heated at a temperature of 200-300 °C for ~ 10 minutes to evaporate the water. The carbon grid is then transferred to a JEM-3010 TEM equipment where the surface of the grid is probed. It collects images using a Gatan Orius SC200 CCD Camera (2K x 2K) with windows XP computer running a digital micrograph software, which is capable of recording in-situ events at a TV rate and high-resolution images. The TEM's images were analyzed using image j software. The distribution of the analyzed images was fitted with a lognormal probability distribution function .The nanoparticle's sizes, r was fitted with a lognormal probability distribution function $P (r)$:

$$P (r) = \frac{fac}{r} \cdot \frac{1}{\sqrt{2\pi}R_{sig}} \exp\left(-\frac{(\log r - R)^2}{2R_{sig}^2}\right) \quad (3.1.1)$$

Where R , is the probable size of the nanoparticles and R_{sig} is the width of the distribution of the nanoparticles.

3.2 Preparation of NaCl and BTPPATPFB Salts

Sodium chloride (NaCl) was purchased from Alfa Aesar Putratronic and roasted at 450 °C for 45 minutes to remove organic impurities. The final product was allowed to cool to room temperature (25 °C) and stored in a tightly sealed container. The Bis(triphenyl phosphoranylidene)

ammonium tetrakis penta fluorophenyl borate (BTPPATPFB) salt was prepared by dissolving equal moles (1:1) of bis(triphenyl phosphoranylidene) ammonium chloride (BTPPACl) and potassium ammonium tetrakis penta fluorophenyl borate (LiTPFB) separately in a 2:1 volume ratio of methanol and water separately. Each mixture, after dissolving in the water/methanol mixture was slowly and simultaneously poured into a cleaned beaker containing a magnetic stirrer to mix the reactants. A gel-like product appears in the beginning of the reaction and becomes a slurry as more of the reactants were added. The product was allowed to sit for about 30 minutes for the reaction to complete. Liquid (filtrate) in the product was removed by filtering the slurry with a 0.2 μm Wilma filter. The solid part of the product was allowed to dry on the filter for about 24 hours. To crystalize the dried product, a small amount of acetone was used to dissolve the product in a clean dry beaker. The dissolved salt was heated gently until a cloudy solution appeared at which the heating was discontinued and taken off the heating element. The solution was allowed to cool to room temperature where small white crystals, about 2-3 mm in size were formed. The crystals were separated from the acetone solution with a 0.2 μm Wilma filter and transferred into a cleaned bottle and allowed to dry for about 24 hours.

3.3 Purification of 1, 2-dichloroethane (DCE)

1, 2-dichloroethane used for this study was purchased from Sigma Aldrich with a purity of 99.8%. The DCE was further purified by running it through activated aluminum oxide in a glass column 6 times to remove ionic impurities. For every third run, fresh activated alumina was used.

3.4 Electrolyte Preparation

Water from Nanopure UV Barnstead system whose conductivity is approximately 17.7-18 M Ω -cm (Siemens) was used to prepare the NaCl solution by adding the water to a known amount of NaCl salt in a 500 mL volumetric flask. While the volumetric flask was tightly sealed, the flask was shaken to dissolve the NaCl in water. About 10 mL of purified DCE was added to the water solution to saturate it. This pre-equilibration prevents diffusion of bulk DCE to the water side of the interface during experimentation. The water solution was placed in a rum shaker oscillating at a frequency of 10 Hz for 24 hours to completely saturate the bulk water with the added DCE. The water solution was filtered with a 0.2 μ m filter (OMNIPORE membrane filter, PTFE) stainless steel pressure filter holder purchased from Sartorium Stedim Biotech (16249) to remove residual alumina entrained in the DCE. A small amount of water together with the saturation DCE were left to remain in the flask and safely discarded.

The BTPPATPFB in DCE solution was prepared by adding purified DCE to a known amount of BTPPATPFB salt in a 500 ml volumetric flask. The flask was tightly sealed and shaken to completely dissolve the BTPPATPFB salt. The DCE solution was saturated with about 10 mL of water in order to prevent water diffusing into the DCE bulk phase during experimentation. The volumetric flask was placed in the rum shaker for about 24 hours for complete saturation. The saturation water placed on top of the DCE was removed after 24 hours and the DCE solution filtered with a 0.2 μ m filter (OMNIPORE membrane filter, PTFE) using a stainless steel pressure filter holder from Sartorium Stedim Biotech (16249) to remove residual alumina. The BTPPATPFB has 58% solubility in DCE according to conductance measurement (94).

3.5 Making of Electrodes

The electrodes used were platinum (Pt) mesh and silver/silver chloride (Ag/AgCl). The platinum electrodes were purchased from Alder with 99.999% purity and the Ag/AgCl electrodes were prepared in our laboratory. To make Ag/AgCl electrode, a pure Ag metal about 3 mm thick was coated with silver chloride (AgCl) through an electrochemical reaction. The electrochemical process was done by passing ~ 10 mA current through two cleaned Ag electrodes in a 0.1 M hydrochloric acid (HCl) aqueous solution placed in a beaker for about 1 minute. The following reaction describes the electrochemical reactions at the anode and cathode respectively.

At the Anode:



The Ag^+ combines with chloride ion (Cl^-) in the solution to give:



AgCl deposits on the Ag metal anode forming the Ag/AgCl electrode.

At the Cathode:



The Ag^- combines with H^+ in the solution to give:



3.6 Sample Cell

The glass sample cell, ~7 cm in diameter, was cleaned with piranha solution in a 1:3 volume ratio of hydrogen peroxide (H_2O_2) and sulphuric acid (H_2SO_4) respectively. Piranha solution oxidizes organic impurities mainly of carbon and hydrogen compositions to carbon dioxide (CO_2) and water (H_2O). It also generates a hydroxyl group (OH^-) group on the surface of the glass which binds with water molecule and improve the glass cell's wettability with the aqueous phase. Piranha solution is very exothermic and should be prepared in a fume hood. The peroxide solution in a separate beaker was slowly poured into the beaker containing sulphuric acid while the solution was continuously stirred. The hot mixture is carefully poured into the glass cell and allowed to sit in the cell until it cools down to room temperature. At this temperature, all organic contaminants were assumed to be completely oxidized to CO_2 and H_2O . The cooled piranha mixture was disposed in a special waste delivery bottle with perforated caps to allow built up gas (CO_2) to escape. The cell was generously washed with water and dried with 99.99% nitrogen gas. The sample cell is a four electrode system, with electrodes labeled CE_1 , CE_2 , RE_1 and RE_2 . The electrodes CE_1 and CE_2 provide electric field across the water/DCE interface while the electrodes RE_1 and RE_2 simultaneously measure the current due to ion adsorption at the interface. The CE_1 and CE_2 act as negative and positive polarities as shown in the following Figure 9.

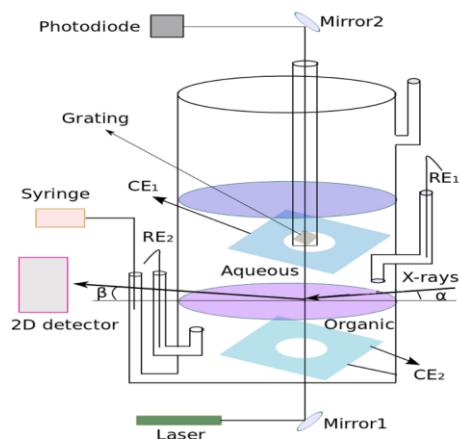


Figure 9. The experimental set up of the glass cell and its auxiliary components.

A 532 nm green laser steered by Mirror 1 passes through the interface where it is scattered and steered by Mirror 2 to a photodiode detector. The scattering of the laser at the interface is due to thermal capillary waves. An auxiliary grating about $10 \times 10 \text{ mm}^2$ contained in a glass column provides additional light scattering to augment the weak scattering from the interface. An incoming x-ray impinges on the interface at an angle, α , where it scatters and leaves the interface at an angle, β . The scattered x-ray intensity is collected on a 2D detector for analysis. A syringe pump is used to regulate the level of the interface during x-ray measurement by adding or removing DCE from the lower bulk phase. An X-ray measurement requires a very flat liquid-liquid interface. Since the water readily wets glass and the DCE does not wet the glass, a curved meniscus at the interface will be formed, thereby making X-ray measurements and analysis difficult. To address this meniscus problem, a hydrophobic strip of Mylar ($10 \text{ }\mu\text{m}$ thick) is aligned on the DCE side of the interface to wet the DCE. This eliminates the curvature problem by changing the wetting surface of the glass on the DCE side. Equal volumes ($\sim 100 \text{ mL}$) of the electrolyte solutions were measured into the glass cell. The organic electrolyte due to its

relatively high density (1253 kg/m^3) is poured at the bottom of the cell while the aqueous phase is later poured on top of the DCE. Few drops of an electrolyte solution consisting of 10 mM aqueous lithium Chloride (LiCl) and 1 mM bis(triphenyl phosphoranylidene) ammonium Chloride (BTPPACl) were added to the side of the lower lugging capillary containing the RE_2 electrode. The RE_1 electrode is located in the upper lugging capillary of the aqueous phase. The overall electrochemical set-up of the cell is described as :

Ag | AgCl (RE_2) 50 mM NaCl (Water) || 5 mM BTPPATPFB (DCE) 10 mM LiCl + 1 mM BTPPACl (Water) | AgCl (RE_1) | Ag .

3.7 Determination of Potential of Zero Charge (PZC)

An applied external potential across the cell is different from the interfacial potential. The least amount of current occurs when the potential across the interface is zero. At this potential also known as potential of zero charge (PZC), the ions do not feel any external force. There is no surface excess charge across the interface at the PZC. The external potential applied across the cell consists of the potential at the interface and the potential across all other parts of the electrochemical cell. Forming interfaces. Therefore, a theoretical framework is required to discriminate the potential across the interface from the overall cell potential. There is a thermodynamic relationship between the PZC and interfacial tension, which can be established experimentally. The definition of thermodynamic quantities are based on bulk properties because the interface differs from the bulk phases by composition (95-97). Considering two semi-infinite bulk phases of the water/DCE system, as in Figure 10.

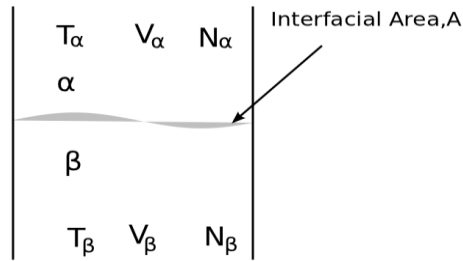


Figure 10. Interfacial and bulk quantities of thermodynamics

In a canonical ensemble, the thermodynamic property of the water/DCE system is determined by the temperature (T), volume (V), and number of ions (N) without direct reference to the details of the ions in the system. The volumes V_α and V_β are defined with respect to a reference surface/plane known as the Gibbs dividing surface (GDS) (96), and the total volume

$V = V_\alpha + V_\beta$. The surface was chosen such that $\sum_i \mu^i N^i = 0$ where i is ionic species, N is the number of ionic species, and μ is the chemical potential of the ionic species. The Helmholtz free energy, F in both phases are defined such that:

$$F_\alpha = -pV_\alpha + \sum_i \mu^i N_\alpha^i, \quad F_\beta = -pV_\beta + \sum_i \mu^i N_\beta^i \quad (3.7.1)$$

The total free energy of the system is:

$$F_\alpha + F_\beta = -pV + \sum_i \mu^i N^i \quad (3.7.2)$$

The bulk phases are characterized by volume, temperature and number of particles. To account for the total energy of the system, the interface whose area is A , and distinct from the bulk phases has to be taken into consideration. This energy of the interface (F) is the excess free energy of the system.

$$F = F_{\alpha}(V_{\alpha}, \mu_{\alpha}, N_{\alpha}, p) + F_{\beta}(V_{\beta}, \mu_{\beta}, N_{\beta}, p) + F_s(A, \gamma) \quad (3.7.3)$$

We define the free energy at the interface as:

$$F_s = \gamma A \quad (3.7.4)$$

Where γ is the energy per unit area of the interface and A is the area of the interface. This energy per unit area is the energy cost in creating such surface with an area A under conditions of isothermal reversible work. An applied external field across the interface changes the interfacial energy dF , defined as:

$$dF = \gamma + \sigma d(\Delta\phi_{cell}^{w-o}) \quad (3.7.5)$$

Where σ is the excess surface charge per unit area and $\Delta\phi_{cell}^{w-o}$ is the external potential applied across the interface. At thermodynamic equilibrium (thermal and chemical) where T , p , V and μ are constant, $\frac{\partial F}{\partial \Delta\phi_{cell}^{w-o}} = 0$ and we have Lippmann equation, $\sigma = -\left(\frac{\partial \gamma}{\partial \Delta\phi_{cell}^{w-o}}\right)_{T,V,\mu}$. This equation defines the excess surface charge concentration under constant temperature, T , volume V , and

chemical electrochemical potential, μ , of the system. Electro-neutrality condition holds for the system such that at any given external potential, $\sigma_w + \sigma_o = 0$ for the water, w and organic, o , phases.

3.8 Quasi-elastic Light Scattering (QELS) Technique

Considering a thermally fluctuating surface whose surface modes are represented in Figure 11.

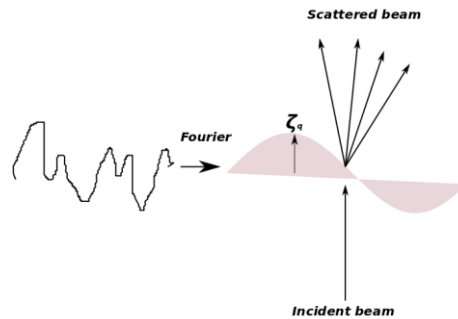


Figure 11. Capillary surface fluctuation at the interface

The amplitude of the mode $\zeta_k(t)$ is given by (98):

$$\zeta_k(t) = A^{-1} \int d^2r \zeta(\vec{r}, t) \exp(i\vec{k} \cdot \vec{r}), \quad (3.8.1)$$

where $\zeta(\vec{r}, t)$ is the vertical thermally induced displacement of the liquid whose projection on the horizontal plane is \vec{r} and A is the surface area of the vertically displaced liquid. At thermal equilibrium, the average displacement $\langle \zeta(\vec{r}, t) \rangle = 0$ where $\langle \rangle$ is the ensemble average of the height fluctuations at the interface. A space-time correlation function for the surface, $\overline{\zeta(t, r) \zeta(t + \tau, r + \Delta)}$

which is temporal and spatially invariant, is defined for the system. The displacement Δ represents a change in position after time, τ from a reference point r . Thus, for wave vectors k and k' corresponding to different surface modes at the interface, the space-time correlation function is:

$$\overline{\zeta_k(t)\zeta_{k'}(t+\tau, r+\Delta)} = \int \Delta g(\tau, \bar{\Delta}) d\tau \int d^2R \exp(i(\bar{k}' - \bar{k}) \cdot \bar{R}), \quad (3.8.2)$$

where $\bar{R} = (\vec{r} + \vec{r}')/2$. Since $\int d^2R \exp(i(\bar{k}' - \bar{k}) \cdot \bar{R})$ is zero unless $\bar{k} = \bar{k}'$ and r is the projection of the displaced fluid in the horizontal plane. The Fourier transform of the space-time correlation function becomes:

$$G_k(\tau) = \int \Delta g(\tau, \bar{\Delta}) d\tau \quad (3.8.3)$$

Equation (3.8.3) is the correlation function of the thermally induced fluctuating surface. The Fourier transform of the surface correlation function gives the surface fluctuation power spectrum ($P_k(\omega)$) (98) :

$$P_k(\omega) = (2\pi)^{-1} \int_{-\infty}^{+\infty} d\tau G_k(\tau) \exp(i\omega\tau) \quad (3.8.4)$$

ω is the propagating frequency of the surface modes. In the QELS technique, the scattered light intensity was measured as an electric field current, i . The measured current i consists of scattering from a grating, E_{l0} , and scattering from the thermally induced fluctuating surface E_s , (98).

$$i \sim (E_{l0} + E_s)^2 = |A_{l0} e^{i\omega_0 t} + A_s e^{i(\omega_0 \pm \omega)t} + cc|^2 \quad (3.8.5)$$

The right hand side of equation (3.8.5) can be simplified to $|A_{l_0}A_s|e^{i2\omega_o+\omega)t} + |A_s|^2e^{i2(\omega_o+\omega)t} + cc'$, where A_{l_0} is the scattering amplitude of the incident electric field scattered from the grating, A_s is the scattering amplitude of the electric field from the fluctuating surface, ω is the offset frequency from the propagating frequency at the interface (ω_o) by the grating and cc' is an additional complex conjugate term. Intrinsic noise in the laser adds an additional term to the scattering from the grating such that $A_{l_0} = A_{l_0}^o + \delta A_{l_0}e^{i\delta t\delta\omega}$. The $A_{l_0}^o$ is the amplitude of the electric field signal scattered from the grating and δA_{l_0} is the amplitude of the accompanying noise signal from the incident beam which varies with time (δt) and $\delta\omega$ is the frequency of the noise. The scattered intensity on the photodiode detector can be analyzed in different forms (98):

$A_s \gg A_{l_0}$ and the analyzed signal is homodyne detection : $(|A_s|^2e^{i2(\omega_o+\omega)t})$.

$A_{l_0} \gg A_s \gg \delta A_{l_0}$ and the analyzed signal is heterodyne detection : $(|A_{l_0}A_s|e^{i2\omega_o+\omega)t})$

$\delta A_{l_0} \gg A_s$ and the analyzed signal is laser intrinsic noise : $(A_{l_0}^o + \delta A_{l_0}e^{i\delta t\delta\omega})$

Our goal is to use heterodyne detection at the water/DCE interface.

3.9 Spectral Analysis of QELS from Liquid-Liquid Interface

The spectral analysis of the scattered intensity by the correlator is a Fourier transform (FT) of the correlation function. The scattering wave vector from the interface is k_o . The peak center f_c of the spectrum can be estimated from Lamb's equation (99):

$$f_c^2 = \frac{\gamma k_o^3}{(2\pi)^2(\rho_{m,o} + \rho_{m,w})} \quad , \quad (3.9.1)$$

where γ is the interfacial tension, $\rho_{m,o}$ and $\rho_{m,w}$ are the mass densities of organic (DCE) and aqueous (water) phases respectively. To account for the effect of viscosity, η , on the thermally induced wave which offsets the peak center of the spectrum, we have (99):

$$f_p = f_c - \frac{f_c^{1/2} k_o [(\rho_{m,w} \eta_w) + (\rho_{m,o} \eta_o)]^{1/2}}{4\sqrt{\pi}(\rho_{m,w} + \rho_{m,o})} \quad (3.9.2)$$

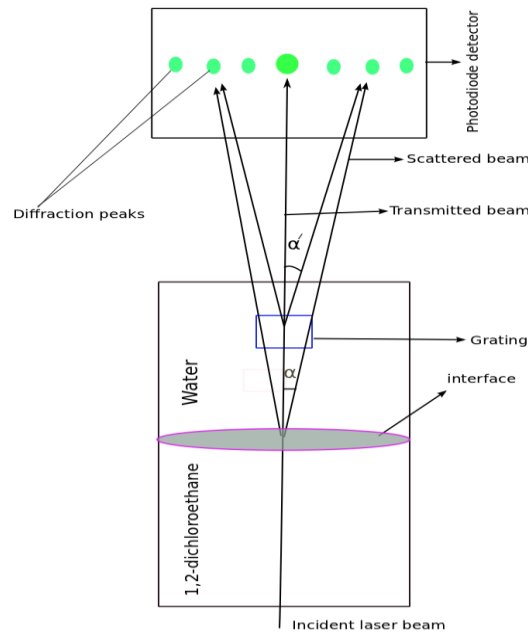


Figure 12. Scattering from water/DCE interface and gratings

From the Figure 12, the wave number (k_o) of the scattered intensity from the interface is ,

$$k_o = \frac{2\pi \sin \alpha}{\lambda},$$

where α is the angle the scattered intensity makes with the normal to the surface

and λ is the wavelength of the laser (532 nm). The scattering from the grating by Bragg's diffraction whose spacing d is 250 μm is given as, $d \sin \alpha' = n\lambda$ where n is the diffraction order,

α' is the scattering angle of the intensity from the grating. The photodiode detector is about 1m (100 cm) away from the interface while the distance between the interface and the grating is about 1 cm. Hence, one can assume $\alpha \approx \alpha'$ and $k_o \approx \frac{2\pi n}{d}$. That is the wave number from the grating and the interface are assumed to be equal. The surface fluctuating power spectrum can be analyzed by fitting a Lorentzian function (*LF*) to the measured experimental spectrum. The model *LF* is of the form (98):

$$P_k(\omega) = \frac{2k_B T(\eta_o + \eta_w)}{\pi\gamma(\rho_o + \rho_w)(\omega - \omega_k)^2 + (\Delta\omega_k)^2} \quad (3.9.3)$$

where ω_k is the peak frequency of the scattered intensity, $\Delta\omega_k$ is an offset from instrumental resolution, T is temperature, γ is interfacial tension, k_B is Boltzmann constant, η_w and η_o are viscosities of water and organic electrolytes respectively.

3.10 Cyclic Voltammetry

Cyclic Voltammetry (CV) is a complementary technique used to measure the flow of ions across the interface. By scanning the interface with a range of interfacial potential, currents were measured. Figure 13 is a CV measurement of a 50 mM NaCl aqueous solution with 5mM BTTPATPFB in DCE at a scan rate of 5 mV/s.

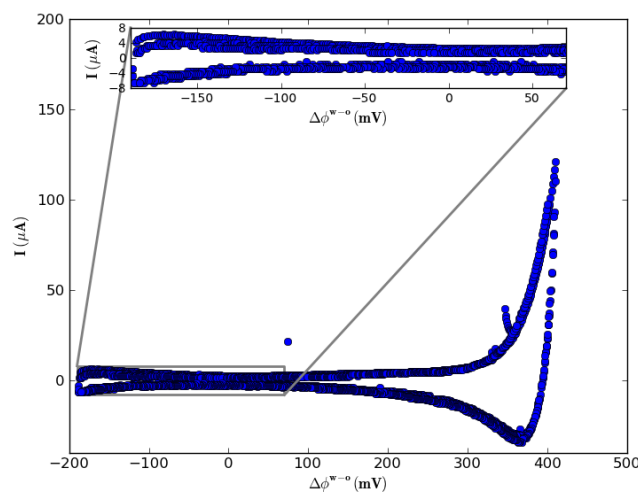


Figure 13. CV of 50 mM aqueous NaCl concentrations and 5 mM BTPPATPFB in DCE with a scan rate of 5 mV /s.

On applying an external field across the interface, ions moved toward the interface from the bulk where they are measured as currents. CV measurements was done in the interfacial potential range of -190 to 400 mV in a step of 5 mV/s in a forward and backward sweep of 5 cycles. The curve in Figure 13 is consistent with literature curves of CV measurements (100-103). The low current between -190 mV and 100 mV in Figure 13 correspond to ions moving towards the interface and remaining on either side of the interface without crossing. This is capacitive current. Beyond the 100 mV in Figure 13, the current increases and grows exponentially indicating ions transfer across the interface. A cartoon depicting the flow of ions in the low currents and high currents from the CV measurements in Figure 13 is shown in Figure 14.

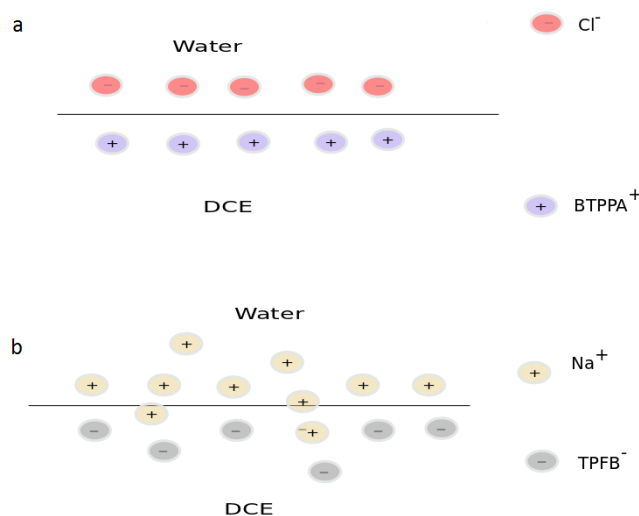


Figure 14. : a) When ions move to the interface without crossing b) When ions (Na^+) begin to cross the interface

TABLE I. GIBBS ENERGY TRANSFER OF IONS FROM WATER TO DCE (94)

Ion	Na^+	Cl^-	BTPPA^+	TPFB^-
$\Delta G^{w \rightarrow o}$ (kJ/mol)	57.7 ± 6	53.0 ± 4	-56 ± 2	-72.5 ± 6
$\Delta G^{w \rightarrow o}$ (mV)	508 ± 52.8	550 ± 41.5	-536 ± 19.1	-717 ± 59.3

To understand the flow of ions across the interface, the Gibbs transfer energies of the ions in the water/DCE system are shown in Table I. At the positive potential in Figure 13, it is expected that the electric field applied should transport Na^+ ions from the bulk water to the water side of the interface and transport the TPFB^- ions from the bulk DCE to the DCE side of the interface as well. The Gibbs transfer energy required to transport TPFB^- across the interface is 717 mV while the Gibbs transfer energy required to transfer Na^+ across the interface is 508 mV. From the Figure 13, the transfer of ions across the interface take place beyond 300 mV. It is clear that if any of the ions will be transported across the interface at high positive potentials on the water side, Na^+ ions should

readily transport compared with TPFB⁻ on the oil side based on their Gibbs transfer energy. We believe that experimental conditions are different from theoretical estimates of Gibbs transfer energy. The Gibbs' transfer at standard conditions assumes an infinitely dilute system, which is far from our experimental condition. This explains the differences in the potentials in which Na⁺ ions were transported in the experiment and the theoretical Gibbs transfer energy in Table I. The Cl⁻ ions even though have a similar Gibbs transfer energy compared with the Na⁺, will remain in the water phase because of the positive polarity of the electrode in the bulk aqueous phase. The TPFB⁻ on the DCE side of the interface will not transfer across the interface at the high positive potentials due to its high Gibbs transfer energy needed to transfer it across the interface, which is beyond our experimental measurements.

CHAPTER 4

X-RAY MEASUREMENTS

X-ray surface scattering techniques have been used to probe molecular structure at liquid-liquid interfaces with sub-nanometer spatial resolution (104). The main techniques used in this study are grazing Incidence small angle Scattering (GISAXS) and X-ray reflectivity (XR). While GISAXS is generally used to probe in-plane structures, XR is used to probe structures normal to the surface (perpendicular to the interfacial plane). A liquid surface reflectometer is used for both GISAXS and XR measurements.

4.1 Liquid Surface Reflectometer

Liquid surfaces and interfaces are of interest to scientists and engineers because they can be used to test ideas of structure and phase transitions. Understanding interfaces and surfaces offers an opportunity to understand synthetic and naturally occurring processes which can be optimized for technological advances in the field of medicine, pharmaceuticals, extraction, catalysis, communication, among others. The challenge is the technique needed to probe the length scales of the surfaces and interfaces. One of the rapidly growing techniques in recent times is the X-ray technique. This technique is able to measure length scales in atomic resolution and is applicable to a wide range of processes, which require special environments for studying, for example, ultra-low pressure processes to ultra-high pressure processes. The liquid surface reflectometer is a set of optical arrangements designed to select a monochromatic X-ray energy, which interacts with the interfaces and surfaces to reveal their structural make up under various experimental conditions.

XR and GISAXS were used to study the structure of the adsorbed nanoparticles at the water-DCE interface with the surface reflectometer at ChemMatCars beamline 15-ID at the Advanced Photon Source (Argonne National Laboratory, USA). XR was performed under specular condition ($\alpha = \beta$) which probes the part of the interface normal to the sample's surface as in Figure 15.

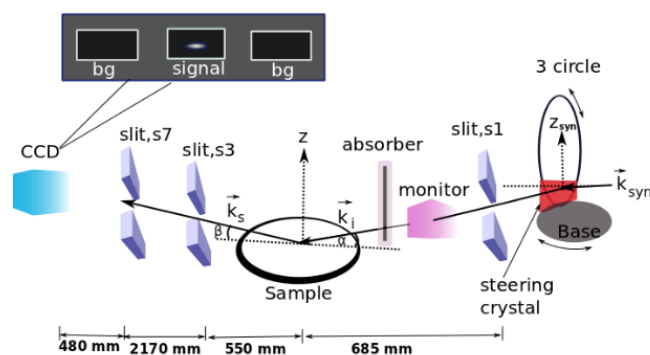


Figure 15. Schematic of the X-ray surface reflectometer for probing surfaces.

XR was measured by varying the perpendicular momentum transfer, Q_z at the water/DCE interface where, $Q_z = (4\pi/\lambda) \sin \alpha$ for specular reflectivity, α is the angle of incidence and λ is the wavelength of the X-ray forming a set of points called reflectivity curve. The energy of the X-ray used and convenient for this study was a 30 keV corresponding to a wavelength, $\lambda \sim 0.4132 \pm 0.00005 \text{ \AA}$. This almost monochromatic X-ray energy was obtained by using a set of optical arrangements to resolve a broad range of X-ray energy source. The resolved X-ray is further resolved by optical set-ups near the sample (steering crystal under Bragg diffraction). The steering crystal made of germanium, Ge (111) also deflects the resolved X-ray energy to the desired angle (angle of incidence, α) unto the sample's interface. Before the X-ray hits the surface of the sample,

a rectangular slit, $S1$ of dimension $15 \times 100 \mu\text{m}^2$ (height \times width) is placed between the sample and the steering crystal to pre-determine the footprint of the X-ray at the interface.

The incident X-ray is scattered from the interface and collected on the 2D CCD detector. In addition to the scattered X-ray from the interface, a fraction of the direct beam penetrates through the upper phase (aqueous phase) and the glass after transmitting through the liquid-liquid interface and eventually striking the CCD detector. This beam can be separated from the reflected beam on the detector down to the smallest measured reflection angles (5×10^{-4} rad). A rectangular aperture, slit $S3$ (about 1 mm in height), is placed between the sample and the detector at a distance of approximately 550 mm from the sample to reduce scattering from the bulk liquid. The $S3$ slit is mounted to an arm that follows the reflected beam, ensuring that the scattered intensity passes through the center of the slit, $S3$ as the incident angle is varied.

The CCD has a large active area of $6 \times 6 \text{ cm}^2$. Although fixed in position, it can detect reflectivity throughout the entire angular range of measurements. A 5 mm vertical slit, $S7$, is placed 480 mm away from the detector to reduce the background scattering from the experimental hutch. This slit is mounted in a fixed position, however, it has movable jaws that can be moved to follow the reflected beam and block the direct beam. The reflected beam intensity is calculated by summing over a region of the 30×60 (height \times width) virtual pixels whose center is determined by a 2D dimensional Gaussian fit to the signal. The background is the average integrated intensity over two similar regions, separated horizontally on either side of the measured signal by ± 0.1 degrees.

4.2 Momentum Transfer

An X-ray wave impinging on a surface with an incident wave vector, \vec{k}_i is scattered from the surface with an out-going wave vector, \vec{k}_s such that the wave vector transfer (momentum transfer), $\vec{Q}_z = \vec{k}_s - \vec{k}_i$. The incident wave vector, scattered wave vector and the wave vector is shown in Figure 16 (105).

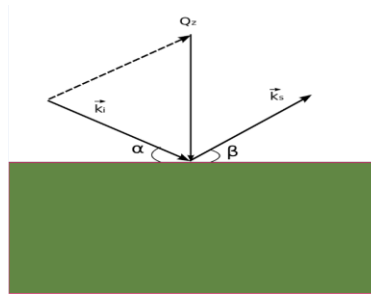


Figure 16. Momentum Transfer, Q

The magnitudes of the incident and scattered wave vectors are $|\vec{k}_i|$ and $|\vec{k}_s|$ respectively such that $|\vec{k}_i| = |\vec{k}_s| = k$. By resolving the wave vectors normal to the scattering surface, the momentum transfer, $Q_z = k \sin \alpha + k \sin \beta$. A special case of scattering, where the angle of incidence, $\alpha = \beta$ gives $Q_z = 2k \sin \alpha$ where $k = 2\pi/\lambda$ and λ is the wavelength of the incident X-ray.

4.3 GISAXS Measurements

GISAXS is used to probe molecular ordering within the surface. The X-ray beam is incident on the sample at an angle slightly below the critical angle for total reflection. The critical wave vector, Q_z for the water/DCE interface is 0.008 \AA^{-1} . A CCD detector collects the scattered X-ray photons, which contain the information of the sample. Another scattering technique, grazing incidence diffraction (GID) is also used to probe molecular length scales. Although GISAXS data may include GID measurements, GID refers to the measurement of Bragg rods that reveal an ordered structure. The scattered beam from the interface, together with a portion of the incident beam, which penetrates through the upper phase, is recorded on a detector. Figure 17 shows a typical GISAXS measurements for an ordered system where the incident and the scattered intensity are collected on the detector. The X-ray strikes the sample at an angle α where it is scattered at out-of-plane and in-plane angles (azimuthal angle), β and 2θ respectively.

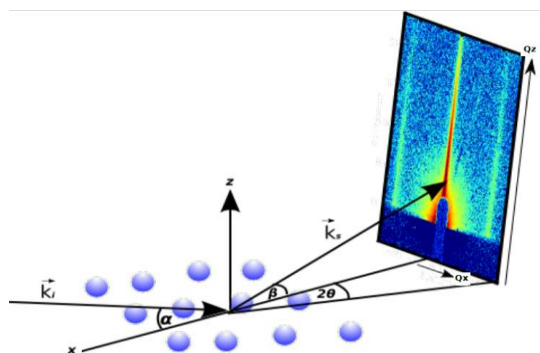


Figure 17. Bragg diffraction rods from ordered in-plane structures

The ordered particles scatter the incident X-ray and the scattered X-ray interfere forming dense and diffuse patterns of intensities on detector as in Figure 17. These dense intensities are known as peaks. A Bragg peak or rod is produced when the in-plane momentum vector transfer, Q_{xy} , of

the X-ray is equal to the reciprocal lattice space of the ordered particles, $2\pi/d$ where d is the lattice spacing between the particles.

4.3.1 Form Factor of Nanoparticles

The scattering X-ray intensity (I) from a single nanoparticle is proportional to the form factor of the nanoparticle and the scattering geometry (105). Thus,

$$I \propto \left| \sum_n f_n e^{i\vec{Q} \cdot \vec{r}_n} \right|^2 \propto \frac{Z^2 r_e^2}{L^2} |FT\{\rho(\vec{r})\}|^2 \quad (4.3.1.1)$$

where subscript n is the number of nanoparticles, f is the atomic form factor of a particle, Z is the atomic number, L is the distance from detector to sample, FT is Fourier transform, r_e is the electron scattering radius and $\rho(\vec{r})$ is the electron density. For a spherical shape particle, the electron density, $\rho(\vec{r}) = N/V$ where V is volume of a uniform sphere given as $V = \frac{4\pi R^3}{3}$, R is the radius of the sphere and N is the number of electrons in the nanoparticle.

The form factor of the sphere, $F(Q)$ is the sum of the individual form factors of the atoms making up the sphere. Thus, $F(Q)$ (105):

$$F(Q) = \sum_j f_j e^{i\vec{Q} \cdot \vec{r}_j} = \int \rho(\vec{r}) e^{-i\vec{Q} \cdot \vec{r}} d\vec{r} \quad (4.3.1.2)$$

Substituting electron density, $\rho(\vec{r}) = N/V$, into equation (4.3.1.2):

$$F(Q) = \frac{3N}{4\pi R^3} \int_0^R r^2 dr \int_0^{2\pi} d\varphi \int_{-1}^1 e^{-iQ r \cos(\theta)} d \cos(\theta) \quad (4.3.1.3)$$

Where θ is the angle between the position, r of the particle and the momentum transfer, Q of the scattered X-ray from the spherical particle. By integrating equation (4.3.1.3), the form factor of the sphere:

$$F(Q) = \frac{3}{R^3} \int_0^R r^2 \frac{\sin(Qr)}{Qr} dr = 3 \left(\frac{\sin(QR)}{(QR)^3} - \frac{\cos(QR)}{(QR)^2} \right) \quad (4.3.1.4)$$

For a cylindrical shape whose volume, $V = \pi R^2 L$. The form factor along the long axis (L) is:

$$F_z(Q_z) = \frac{1}{L} \int_{-L/2}^{L/2} e^{-iQ_z z} dz = \frac{\sin(LQ_z/2)}{LQ_z/2}, \quad (4.3.1.5)$$

where L is the height of the cylinder and Q_z is the momentum transfer in the long axis. For a unit cell, the form factor, $F(Q)$, of the lattice is the sum of the form factors of the atoms in the unit cell:

$$F(Q) = \sum_j f_j e^{i\vec{Q} \cdot \vec{r}_j} \quad (4.3.1.6)$$

for which j is an element in the unit cell, \vec{r}_j is the position of a particle j in the unit cell, \vec{Q} is the momentum transfer. The structure factor $S(\vec{Q})$, is the sum of the phases of the unit cells given

as:

:

$$S(\vec{Q}) = \left| \sum_n e^{i\vec{Q} \cdot \vec{R}_n} \right|^2 \quad (4.3.1.7)$$

where \vec{R}_n is the position of each unit cell with respect to the origin of the lattice. This $S(\vec{Q})$ does not involve a particle or an electron but simply their relative positions or phases from the origin.

4.4 X-ray Reflectivity (XR)

X-ray reflectivity probes the electron density variation along the z direction perpendicular to the interface while averaged over the x - y region of the x-ray's footprint on the interface (104).

$$\frac{I}{I_0} = R_F \left| \int_{-\infty}^{+\infty} \frac{1}{\Delta\rho_\infty} \frac{\langle \partial\rho \rangle_{xy}}{\partial z} e^{-iQ_z z} dz \right|^2 \quad (4.4.1)$$

The left side of equation (4.4.1) is the reflected intensity (I) normalized by the intensity incident on the sample (I_0). The Fresnel reflectivity, R_F is the reflectivity for a perfectly flat or an ideal interface. The symbols z and Q_z are the depth and momentum transfer respectively. The term, $\left| \int_{-\infty}^{+\infty} \frac{1}{\rho_\infty} \frac{\langle \partial\rho \rangle_{xy}}{\partial z} e^{-iQ_z z} dz \right|^2$ is the reflectivity due to the presence of structure at the interface also known as structure factor, $\Phi(Q_z)$.

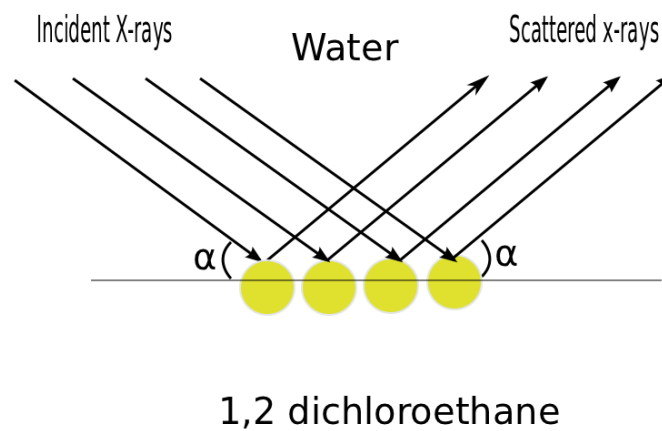


Figure 18. X-ray reflectivity probing gold structure at water- 1,2 dichloroethane interface

In the Figure 18, an incident X-ray wave (I_o) hits the interface where it is scattered by the interface and gold nanoparticle. The collected intensity (I) is normalized with the incident to obtain reflectivity. The equation (4.4.1) shows that there has to be a variation of electron density to have reflectivity. The integral is the Fourier transform (sum of all the electron densities including their respective phases from an origin) of the electron density profile, $\frac{\langle \partial \rho \rangle_{xy}}{\partial z}$ which is averaged over the x - y region and $\Delta \rho_{\infty}$ is the change in bulk densities of the water and DCE phases involved.

Reflectivity data are measured as a function of momentum transfer normal to the interface, $\vec{Q}_z = |\vec{k}_s - \vec{k}_i| = 2k_o \sin \alpha$, where $k_o = 2\pi/\lambda$ is the wave number of the X-ray, \vec{k}_i is the incident wave vector, and \vec{k}_s is the scattered wave vector. The reflectivity data at each Q_z consists of measured specularly reflected X-ray intensity ($\vec{Q}_{xy} = 0$) and the background intensity measured slightly off the specular condition ($\vec{Q}_{xy} \neq 0$) is subtracted from the specular reflectivity measurements. All measured intensities are normalized by the incident beam intensity after background subtraction from the measured signal at the interface.

4.4.1 Critical Wave Vector

The critical wave vector can be obtained by considering a simple s-polarized plane wave moving from medium (1) to another medium (2) as in Figure 19.

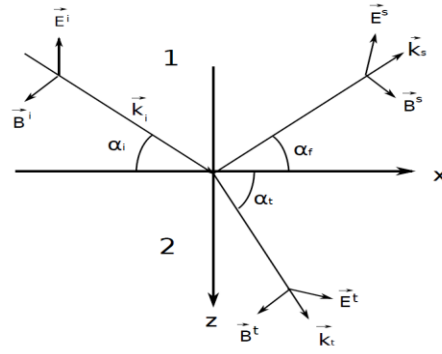


Figure 19. S-polarized plane wave

The refractive index of medium 1 is $n_1 = 1 - \zeta_1 + i\beta_1$ and the refractive index of medium 2 is $n_2 = 1 - \zeta_2 + i\beta_2$. Where ζ is the scattering length of the medium (1 or 2) and α_i, α_t are angles which the incident and transmitted waves make with the horizontal. The scattering length, ζ and absorption factor, β , are defined $\zeta = 2\pi r_e \rho_\infty (1 + f'/Z)/k_0^2$, $\beta = 2\pi \rho_\infty r_e (1 + f'')/k_0^2$, $r_e = e^2/(m c^2)$ is the classical radius of the electron, e of mass m and velocity c , ρ_∞ is the average number of electrons per unit volume of the bulk material, $k_0 = 2\pi/\lambda$, λ is the wavelength of the X-ray, Z is the atomic number of the elements making up the bulk phase and f' and f'' are the real and imaginary parts of the anomalous dispersion corrections to the atomic scattering correction factor, which vary smoothly for X-ray energies greater than 1 keV away from atomic absorption edges (the ionization energies). Typical values of ζ and β are in the order of 10^{-5} and 10^{-6} , respectively. The vector symbols, \vec{E} , \vec{B} and \vec{k} are electric field, magnetic field and wave vectors respectively, while the superscripts i, s and t represent incident, scattered and transmitted respectively.

By Snell's law (106):

$$n_1 \cos(\alpha_i) = n_2 \cos(\alpha_t) \quad (4.4.1.1)$$

$$\frac{n_2}{n_1} \approx \frac{(1-\zeta_2)}{(1-\zeta_1)} \approx 1 + \zeta_1 - \zeta_2 - \zeta_1 \zeta_2 \text{ and considering air whose } \zeta_1 \sim 0 \text{ and } \zeta_1 \zeta_2 \approx 0$$

Considering small angles for which, $\cos \alpha \approx 1 - \frac{\alpha^2}{2}$. By substituting this into (4.4.1.1),

$$1 - \alpha_i^2/2 = \left(1 - \alpha_t^2/2\right) (1 - \zeta_2) . \text{ Assuming, } \zeta_2 \alpha_t^2/2 \approx 0, \text{ then}$$

$$\alpha_i^2 \approx \alpha_t^2 + 2\zeta_2 \quad (4.4.1.2)$$

There exists an angle of incident, $\alpha_i = \alpha_c$ for which the transmitted wave lies parallel to the interface and no reflection. That is for $\alpha_t = 0$, $\alpha_c \approx \sqrt{2\zeta_2}$ from equation (4.5.1.2) .Substituting the scattering length, ζ_2 into the critical angle, α_c

$$\alpha_c \approx k_o^{-1} \sqrt{\left(4 \pi r_e \rho_{\infty,t} (1+f'_2/Z_2)\right)} \quad (4.4.1.3)$$

The critical momentum vector transfer (Q_c) is given by:

$$Q_c = 2k_o \sin(\alpha_c) \approx 4 \sqrt{\left(\pi r_e \rho_{\infty, t} (1 + f'_2 / Z_2) \right)} \quad (4.4.1.4)$$

The equation (4.4.1.4) shows that the critical angle is energy dependent because α_c depends on the wave number which depends on the X-ray's wavelength.

4.4.2 Fresnel Reflectivity

The simplest X-ray reflectivity is from an interface between two bulk phases consisting of vacuum and the flat surface of a material whose index of refraction is given by n . This is known as Fresnel reflectivity. The amplitudes of the transmitted wave \vec{k}_t , the incident wave, \vec{k}_i and the refractive index n of the medium are related by (104):

$$|\vec{k}_t| / |\vec{k}_i| = n = 1 - \zeta + i\beta \quad (4.4.2.1)$$

In air, the refractive index is approximately 1 and the amplitude of the incident wave,

$|\vec{k}_i| = k_o = 2\pi/\lambda$ where $\zeta = 2\pi r_e \rho_{\infty} (1 + f'/Z) / k_o^2$, $\beta = 2\pi \rho_{\infty} r_e (1 + f'') / k_o^2$, $r_e = e^2 / (mc^2) \approx 2.818 \times 10^{-18} m$, r_e is the classical radius of the electron, ρ_{∞} is the average number of electrons per unit volume of the bulk material, λ is the wavelength of the x-ray, Z is the atomic number of the element making up the bulk material and ζ , β are scattering correction factor and absorption, which vary smoothly for x-ray energies greater than 1 keV away from atomic absorption edges (the ionization energies). Typical values of ζ and β are on the order of 10^{-5} and 10^{-6} , respectively. Since, $\beta \ll \zeta$, β can often be ignored for simplification f' and f'' are the real and imaginary parts of the anomalous dispersion corrections to the atoms.

For the s -polarized electric fields – incident $\vec{E}^i(\vec{r})$, reflected ($\vec{E}^s(\vec{r})$) and transmitted $\vec{E}^t(\vec{r})$ – (see Figure 19), the transverse-components of the waves can be expressed as follows (104):

$$\vec{E}^i(\vec{r}) = \hat{y}E^i \exp[\vec{k}_i \cdot \vec{r} - \omega t] \quad (4.4.2.2)$$

$$\vec{E}^s(\vec{r}) = \hat{y}E^s \exp[\vec{k}_s \cdot \vec{r} + \omega t] \quad (4.4.2.3)$$

$$\vec{E}^t(\vec{r}) = \hat{y}E^t \exp[\vec{k}_t \cdot \vec{r} - \omega t] \quad (4.4.2.4)$$

where ω is the angular frequency and t is time. Resolving the wave vectors ($\vec{k}_i, \vec{k}_t, \vec{k}_s$) into vertical and horizontal components, we find:

$$\vec{k}_i = k_{i,x} \hat{x} - k_{i,z} \hat{z} = k_o [\hat{x} \cos \alpha_i - \hat{z} \sin \alpha_i] \quad (4.4.2.5)$$

$$\vec{k}_s = k_{i,x} \hat{x} + k_{i,z} \hat{z} = k_o [\hat{x} \cos \alpha_i + \hat{z} \sin \alpha_i] \quad (4.4.2.6)$$

$$\vec{k}_t = k_{i,x} \hat{x} - k_{t,z} \hat{z} \approx k_o [\hat{x} \cos \alpha_i - \hat{z} \sin \alpha_t] \quad (4.4.2.7)$$

for which \hat{x} , \hat{y} , \hat{z} are unit vectors. Considering $\alpha_t^2 \approx \alpha_i^2 - 2\zeta + i2\beta$, and equation (4.4.2.7) becomes:

$$\vec{k}_t \approx k_o \left[\hat{x} \cos \alpha_i - \hat{z} \sqrt{\sin^2 \alpha_i - 2\zeta + i2\beta} \right] \quad (4.4.2.8)$$

Given $\sin\alpha_c \approx 2\zeta$, and substituting into equation (4.4.2.8) becomes:

$$\vec{k}_t \approx k_o \left[\hat{x} \cos\alpha_i - \hat{z} \sqrt{\sin^2\alpha_i - \sin^2\alpha_c + i2\beta} \right] \quad (4.4.2.9)$$

If $\alpha_i < \alpha_c$ and $\beta \approx 0$, then the normal component of the wave vector becomes imaginary and the amplitude of the wave penetrates into the second medium in a decaying manner (evanescent). The imaginary normal component of the transmitted wave ($k''_{t,z}$) is the inverse of the decay length (Λ):

$$k''_{t,z} = 1/\Lambda \approx k_o \sqrt{\alpha_c^2 - \alpha_i^2} \quad (4.4.2.10)$$

The reflection coefficient $r(\alpha_i)$ and transmission coefficient $t(\alpha_i)$ are given by:

$$r(\alpha_i) = E^s/E^i = (k_{i,z} - k_{t,z})/(k_{i,z} + k_{t,z}) \quad (4.4.2.11)$$

$$t(\alpha_i) = E^t/E^i = 2k_{i,z}/(k_{i,z} + k_{t,z}) \quad (4.4.2.12)$$

The Fresnel reflectivity, $R_F(\alpha_i)$ is expressed as:

$$R_F(\alpha_i) = \left| (k_{i,z} - k_{t,z}) / (k_{i,z} + k_{t,z}) \right|^2 \quad (4.4.2.13)$$

Neglecting β and $k_{t,z} \approx k_o \sqrt{(\sin^2 \alpha_i - \sin^2 \alpha_c)} \approx k_o \left(\sin \alpha_i - \frac{\sin^2 \alpha_c}{2 \sin(\alpha_i)} \right)$ and $k_{i,z} = k_o \sin(\alpha_i)$, we express the reflectivity R_F as:

$$R_F(\alpha_i) \approx \sin^4 \alpha_c / (16 \sin^4 \alpha_i) \approx \left(Q_c / 2Q_z \right)^2 \quad (4.4.2.14)$$

Figure 20a is a typical Fresnel reflectivity from an interface between water and DCE bulk phases. The Figure 20b shows the variation of the electron density as a function of depth, z , which is a step function.

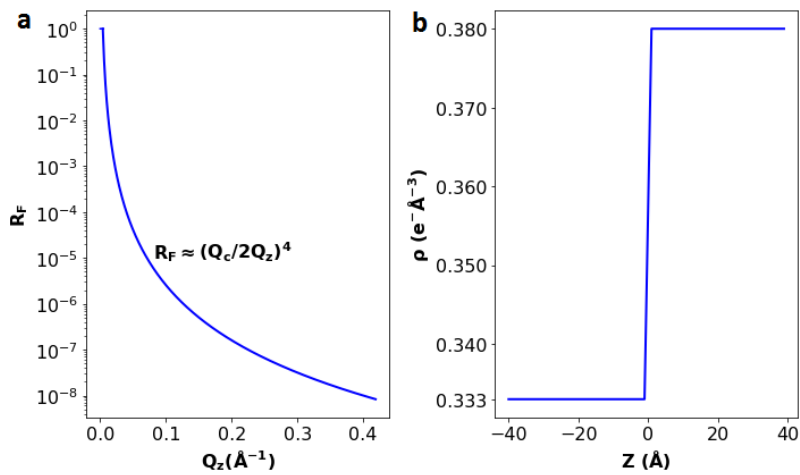


Figure 20. a) Fresnel reflectivity (semi-log scale) as a function of wave vector, Q_z b) electron density of the Fresnel reflectivity for water and DCE bulk phase. An ideal interface is flat and hence the step function of the electron density.

4.4.3 Parratt Reflectivity

The Parratt reflectivity considers a variation of electron density normal to the interface (107). This variation consists of several internal layers whose electron density varies normal to the surface. When X-ray impinges on the surface as shown in Figure 21, the X-ray undergoes both transmission and reflection in the internal layers.

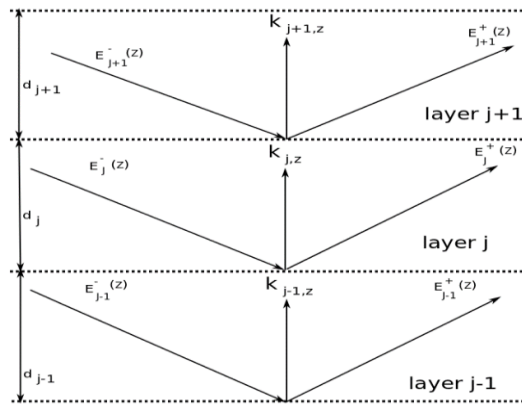


Figure 21. Parratt reflectivity. Electron density varies along the perpendicular direction

Because of the variation in electron density as well as different phases of the internal layers, the X-ray is scattered in different phases. Each layer has a different refractive index related to their electron densities. The refractive index n_j of a wave traveling through the j^{th} layer is $n_j = 1 - \zeta_j + i\beta_j$. The amplitude of the wave vector k_j has both horizontal and vertical components, such that $k_j^2 = k_{x,j}^2 + k_{z,j}^2$, where $k_{x,j}$ and $k_{z,j}$ are the horizontal and normal components of the wave vector k_j . For continuity at the interface, the horizontal components of the wave vector across all the layers are the same. Thus, $k_{j-1,x} = k_{j,x} = k_o \cos(\alpha_i)$. Given $k_j = k_o n_j = k_o [1 - \zeta_j + i\beta_j]$, then

$$k_{j,z}^2 = k_j^2 - k_x^2 = k_o^2 \left[\left(1 - \zeta_j + i\beta_j\right)^2 - \cos^2 \alpha_j \right] \approx k_o^2 [\sin^2 \alpha_j - 2\zeta_j + 2i\beta_j] \quad (4.4.3.1)$$

Taking $Q_j = 2k_o \sin \alpha_j = 2k_{j,z}$ and substituting it into equation (4.4.3.1),

$$Q_j = \sqrt{Q^2 - 8k_o^2 \zeta_j + i8k_o^2 \beta_j} \quad (4.4.3.2)$$

Next to the the last layer is a substrate (bulk phase) where there is no reflection and only transmission. The first step is the calculation of reflectivity from the interface between the substrate and the (j-1)th next to the substrate layer given by (105):

$$r'_{j-1,\infty} = \frac{Q_{j-1} - Q_\infty}{Q_{j-1} + Q_\infty} \quad (4.4.3.3)$$

The amplitude of the reflectivity on the jth layer next to the (j-1)th layer is:

$$r'_{j,j-1} = \frac{Q_j - Q_{j-1}}{Q_j + Q_{j-1}} \quad (4.4.3.4)$$

The amplitude of reflectivity between the (j+1)th and jth layer is:

$$r'_{j+1,j} = \frac{Q_{j+1} - Q_j}{Q_{j+1} + Q_j} \quad (4.4.3.5)$$

By using Parratt's recursive(107), the total amplitude of the reflection on the jth layer is a sum of all reflection amplitudes on and below the jth layer. Thus,

$$r_{j,j-1} = \frac{r'_{j,j-1} + r'_{j-1,\infty} e^{id_{j-1}Q_{j-1}}}{1 + r'_{j,j-1} r'_{j-1,\infty} e^{id_{j-1}Q_{j-1}}} \quad (4.4.3.6)$$

The total recursive amplitude from the $j+1$ th layer, the intermediate layers and the substrate is:

$$r_{j+1,j} = \frac{r'_{j+1,j} + r_{j,j-1} e^{id_j Q_j}}{1 + r'_{j+1,j} + r_{j,j-1} e^{id_j Q_j}} \quad (4.4.3.7)$$

For non-ideal interface where there exists capillary wave roughness or adsorbed nanoparticle, the interface has a structure, which can be resolved with Parratt recursive formula. For example, a rough interface will have variation of electron density normal to the surface as in Figure 22.

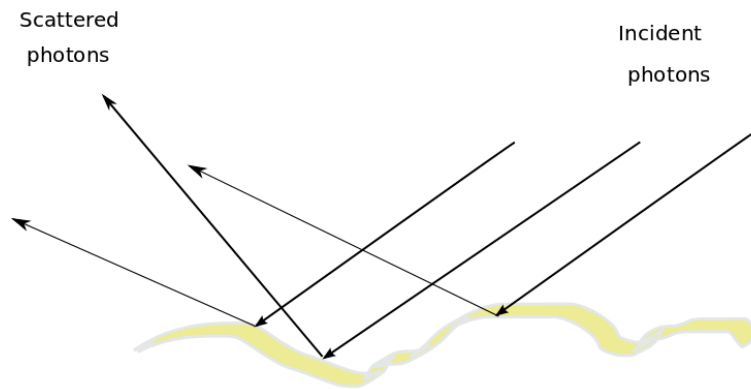


Figure 22. X-ray photons hitting a rough interface and scattered in diffused manner.

The Figure 23 is a typical reflectivity with their corresponding electron density for a non-ideal

surface. The roughness at the interface gives rise to different reflectivity as shown in Figure 23.

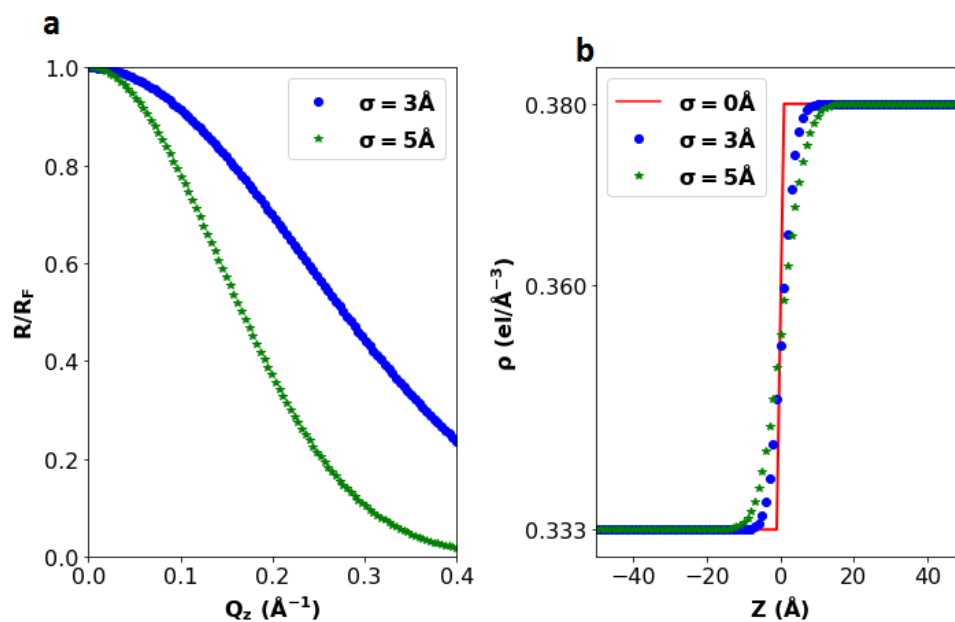


Figure 23. Reflectivity from rough interfaces (non-ideal) of water and DCE normalized with Fresnel reflectivity b) Electron density profile of the corresponding reflectivity. In the absence of roughness, the electron density is a step function.

CHAPTER 5

RESULTS AND DISCUSSIONS

5.1 Results of Interfacial Tension Measurement

Interfacial tension measurement was performed with and without nanoparticles and the results shown in Figure 24. Different bulk concentrations of nanoparticles in the bulk water phase were used: 60 nM and 35 nM nanoparticles in bulk water phase.

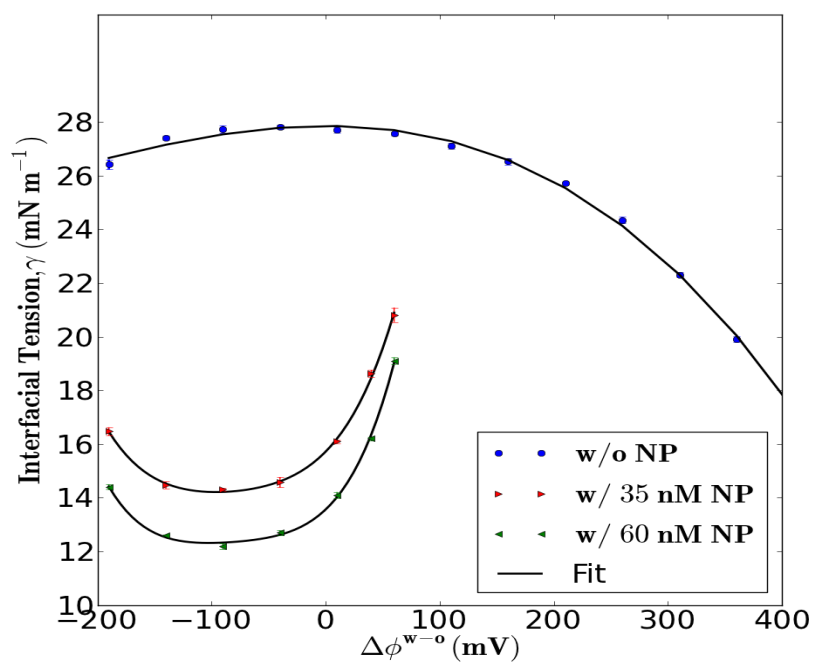


Figure 24. Interfacial tension measurements.

The Figure 24 without nanoparticles (w/o NP) has a characteristic of literature curves (23). The interfacial tension curve without nanoparticles was obtained by taking interfacial tension measurements in a range of potentials (150 mV to 750 mV) in a step of 50 mV across the interface. To find the PZC, the range of interfacial potentials together with their corresponding cell potentials, $\Delta\phi_{cell}^{w-0}$ were fitted to a third order polynomial function from which the PZC (0.341+/- 0.07 V) was extracted. This potential of zero charge (PZC) corresponds to the apex from the tension curve without nanoparticles. The interfacial potential across the interface is given by $\Delta\phi_w^o = \Delta\phi_{w_{cell}}^o - \Delta\phi_{w_{pzc}}^o$ where $\Delta\phi_{w_{pzc}}^o$ is the potential of zero charge and $\Delta\phi_{w_{cell}}^o$ is the potential difference across the entire electrochemical cell. Nanoparticles were added to the bulk phase of the water, continuously stirred and equilibrated at various interfacial potentials.

From Figure 24 (without nanoparticles, w/o NP), the variation in interfacial tension as a function of the interfacial potential shows that the ions in the bulk respond to the external potential. There is an enhancement and repositioning of ions between the bulk phases and the interface leading to variation in the interfacial tension curve. Above the PZC, Na^+ ions are enhanced on the water side of the interface while $TPFB^-$ ions simultaneously enhance on the DCE side of the interface (108). Below the PZC, Cl^- ions are enhanced at the water side of the interface while $BTPPA^+$ are simultaneously enhanced on the DCE side of the interface. Within our working interfacial potentials (60 to -190 mV), the ions in the supporting electrolytes are not expected to be transported across the interface.

Gold nanoparticles were injected into the aqueous phase (w/ 35 nM and w/ 60 nM NP), stirred continuously (at ~ 130 rpm) at an initial interfacial potential of 60 mV leading to reduction in interfacial tension (Figure 24 with nanoparticles) as expected from earlier work from literature (42). Equilibrium was achieved when the interfacial tension did not change by more than +/- 0.5

$\text{mN}\cdot\text{m}^{-1}$. Further decrease in the interfacial potential led to re-positioning of the ions from the aqueous, organic electrolytes (Na^+ , Cl^- on the water side and BTPPA^+ , TPFB^- ON THE DCE side) and the nanoparticles leading to a change in interfacial excess charge. The slope of the interfacial tension measurements curves provides information on the excess charge per unit area Q_{tot} , at the interface given by $Q_{tot} = -(\partial\gamma/\partial\Delta\phi^{w-o})_{T,P,\mu_i}$ (temperature, T , pressure, p , and chemical potential μ_i of species i). The excess charge, Q_{tot} quantifies the enhancement of ions and nanoparticles at the water side of the interface while $-Q_{tot}$ quantifies ions and nanoparticles' enhancement on the DCE side of the interface. The presence of the nanoparticles at the interface initially produced a large positive slope at an interfacial potential, $\Delta\phi^{w-o} > 0$ indicating a net enhancement of negative charges on the water side and positive charges on the DCE side. This is counterintuitive because at a positive potential, Na^+ ions and positively charged nanoparticles are expected to enhance at the water side of the interface and TPFB^- ions on the DCE side of the interface. Our slope at the positive potential indicates that there are negatively charged ions (Cl^- as the suspect) when positive potentials are applied. The net negative excess charge on the water side of the interface and the net positive on the DCE side of the interface from the slope indicates the likely presence of nanoparticles on the DCE side of the interface at $\Delta\phi^{w-o} > 0$. This counterintuitive trend in tension was observed in the previous study of our interfacial tension measurement (45). As the interfacial potential is further reduced and $\Delta\phi^{w-o} < 0$, there is a transition in the slope indicating that the DCE side of the interface has excess positive charge. The most likely reason is the possibility of the nanoparticles initially in the DCE moving to the water side of the interface making the DCE side of the interface negatively charged and the water side positively charged. X-ray measurements will be used to probe the adsorbed nanoparticles and characterize them to determine the position of the nanoparticles as a function of interfacial potential.

5.2 GISAXS Measurements

GISAXS technique was used to measure the in-plane structure of the arrays of the nanoparticles. The result from the Bragg diffraction peaks shown in Figure 25. The Bragg diffraction peaks indicate an ordered nanostructure.

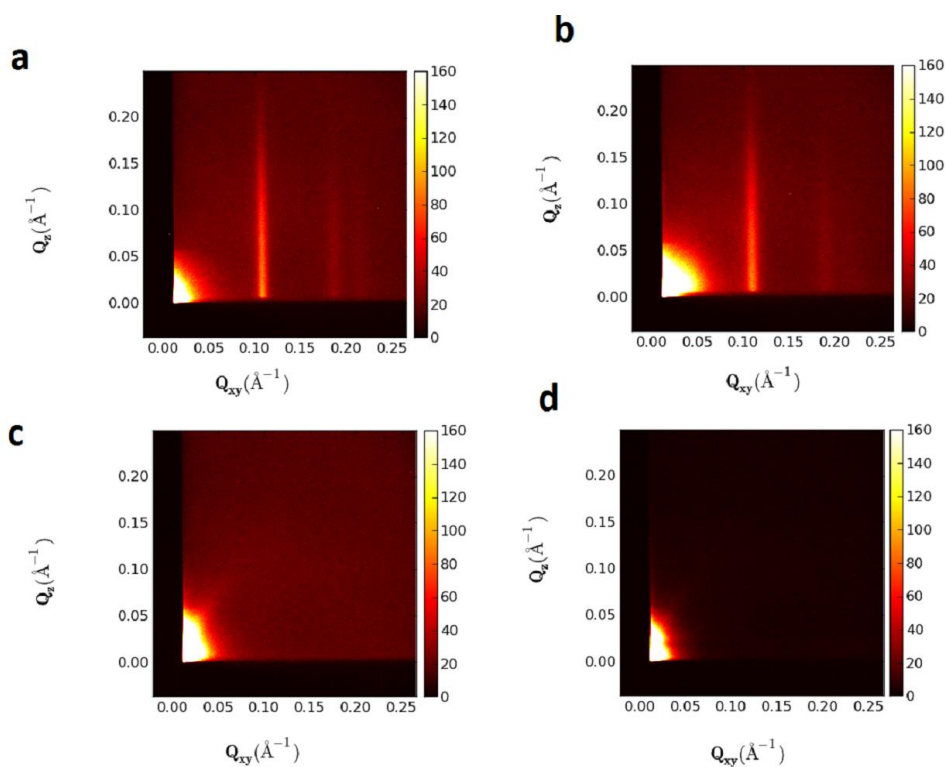


Figure 25. GISAXS measurements of 60 nM nanoparticle concentration in the bulk water phase as a function of interfacial potentials of a) 60 mV b) 40 mV c) 10 mV d) -40 mV. The appearance of the Bragg peaks is an indication of an ordered system at the interface. On the scale, 160 is equivalent to 2165 X-ray photo counts. Data taken with CCD detector.

The decay of the peak intensity along the vertical wave vector, Q_z is a signature of the typical length scale of nanoparticle's size we used in this study. For example in Figure 25a, from the intensity profile, the decay along the vertical axis $Q_z \sim 0.25 \text{ \AA}^{-1}$ has real space dimension diameter = $2\pi/0.25 = 2.5 \text{ nm}$, which is typical of our nanoparticle size from the TEM analysis.

Based on the dimension, the structure formed at the interface is a two dimensional (2D) hexagonal closed packed (HCP) monolayer array at interfacial potentials of 60 mV and 40 mV as in Figure 25 a and b. The in-plane ordering has first, second and third order peaks which indicates different domain orderings at the interface. The positions of the momentum vector parallel to the surface with first, second and third order peaks are $Q_{[10]} \approx 0.1072 \text{ \AA}^{-1}$, $Q_{[11]} \approx 0.1857 \text{ \AA}^{-1}$ and $Q_{[20]} \approx 0.2150 \text{ \AA}^{-1}$ respectively at interfacial potential of 60 mV.

At $\Delta\phi^{w-o} = 40 \text{ mV}$, the unit lattice is still hexagonal except an additional enhanced scattering at the low Q_{xy} near the direct beam ($Q_{xy} \sim 0$) which is not clearly visible but resolved on further analysis. On further analysis, it shows a weak peak at $Q_{xy} \sim 0.033 \text{ \AA}^{-1}$. Thus, there are four diffractions peaks at interfacial potential of 40 mV which are $Q_{[10]} \approx \pm 0.033 \text{ \AA}^{-1}$, $Q_{[11]} \approx \pm 0.1085 \text{ \AA}^{-1}$, $Q_{[20]} \approx \pm 0.18828 \text{ \AA}^{-1}$ and $Q_{[30]} \approx \pm 0.2180 \text{ \AA}^{-1}$. Further tuning of the interfacial potential towards the negative (Figure 25 c and d) led to the disappearance of the higher order peaks and increased intensity at the low Q_{xy} . This low Q_{xy} in intensity is consistent with literature study on GISAXS measurements of 3D pyramidal structures (10, 109).

The centers of the Bragg diffraction peaks, Q_{xy} were obtained by fixing the width of the intensity along the vertical axis ($Q_z = 0.05$ to 0.1 \AA^{-1}) and integrating the intensity along the horizontal (Q_{xy}). The integrated intensity is normalized by the photon intensity hitting the sample.

The resultant curve is fitted to a Lorentzian function with a linear background $f(Q_{xy})$:

$$f(Q_{xy}) = \sum_{i=0}^{N-1} \frac{A_i Q_{w,i}}{\left[(Q_{xy} - Q_{o,i})^2 + \frac{Q_{w,i}^2}{4} \right]} + aQ_{xy} + b \quad (5.2.1)$$

Where N is the number of peaks, Q_{xy} is the in-plane wave vector, Q_o is the peak centre, A is the area of the peak, a is the slope of the linear background and b is the intercept of the linear background. Fitting the Lorentzian to the number of peaks, we obtain Figure 26.

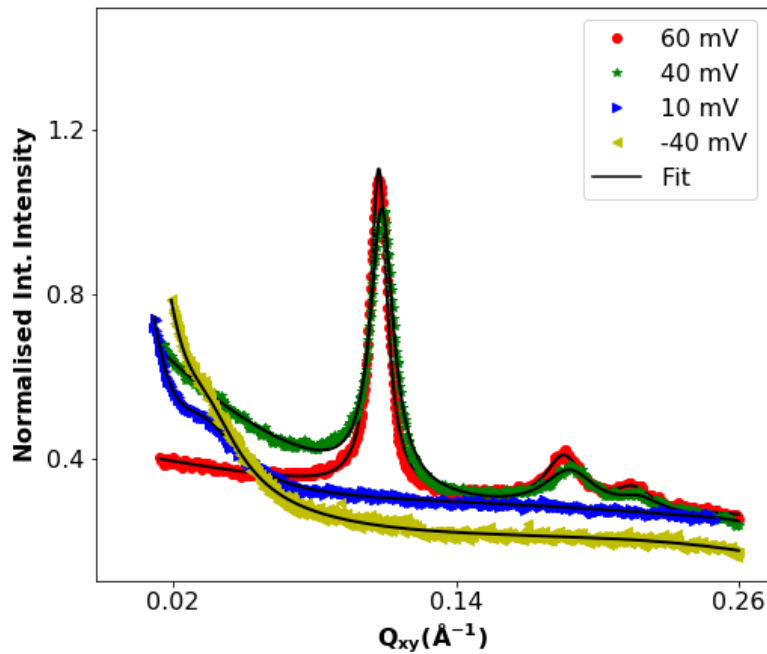


Figure 26. Lorentzian fit of the normalized integrated intensity along the vertical axis, Q_z with sample nanoparticle concentration 60 nM in the bulk water phase.

Similar measurements of the 350 nM sample showed Bragg peaks whose decay along the vertical axis (Q_z) is consistent with the size of the nanoparticles' used in this study. A plot of the Bragg diffraction peaks is shown in Figure 27.

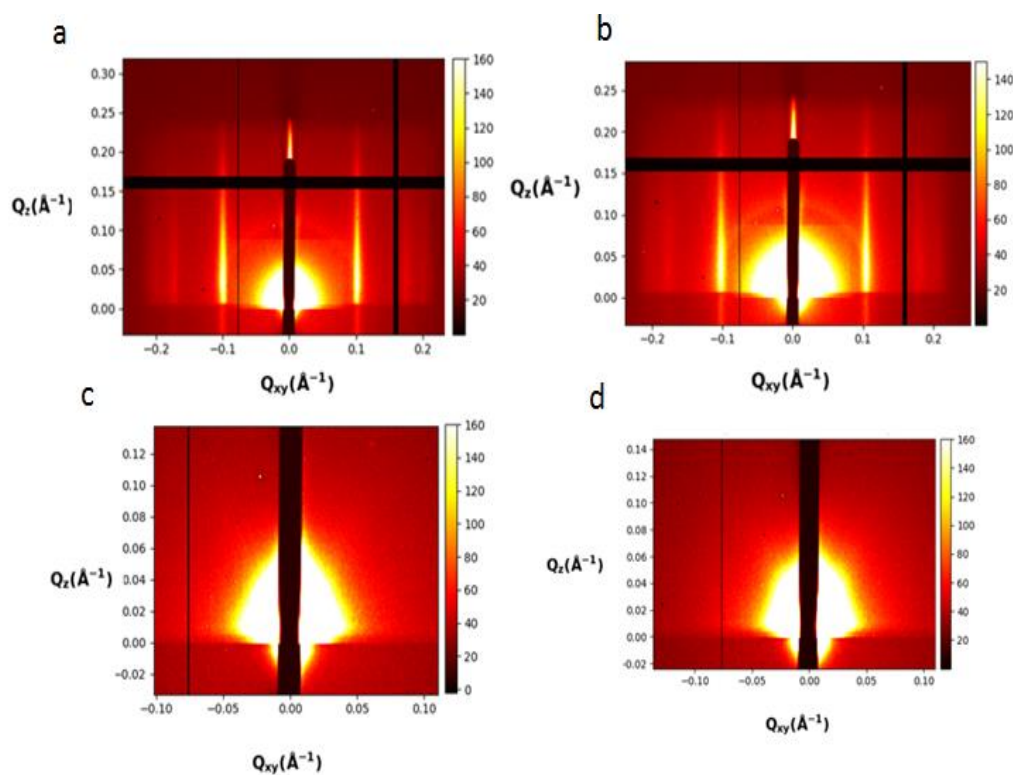


Figure 27. GISAXS measurements of 35 nM nanoparticle concentration in the bulk water phase as a function of interfacial potentials a) 60 mV b) 40 mV c) 10 mV d) -40 mV. The appearance of the Bragg peaks is an indication of an ordered system at the interface.

Measurement was done with APEX detector whose resolution is different from the CCD detector.

The Bragg diffractions peaks of sample with 350 nM nanoparticles in aqueous phase is similar to the peaks observed with the 60 nM nanoparticles concentration in aqueous phase where there is enhanced scattering at the low Q_{xy} .

The analysis of the integrated normalized intensity of Figure 27 are shown in Figures 28 and 29. At $\Delta\phi^{w-o} = 60 \text{ mV}$, the first, second and third order peaks were $Q_{[10]} \approx \pm 0.1005 \text{ \AA}^{-1}$, $Q_{[11]} \approx \pm 0.1743 \text{ \AA}^{-1}$ and $Q_{[20]} \approx \pm 0.1998 \text{ \AA}^{-1}$ respectively. At $\Delta\phi^{w-o} = 40 \text{ mV}$, the first, second and third order peaks' positions are $Q_{[10]} \approx \pm 0.1030 \text{ \AA}^{-1}$, are $Q_{[11]} \approx \pm 0.17912 \text{ \AA}^{-1}$ and $Q_{[20]} \approx \pm 0.2042 \text{ \AA}^{-1}$ respectively.

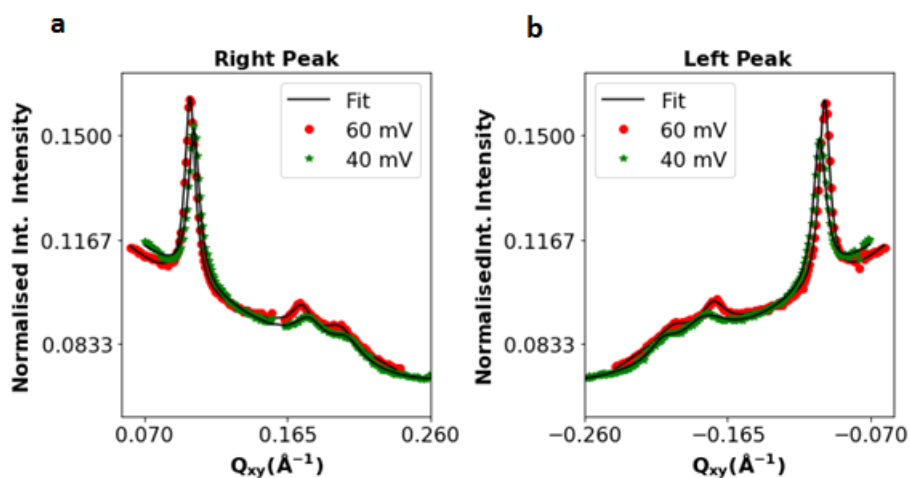


Figure 28. Integrated normalized GISAXS intensity fitted with Lorentzian functions and linear background along the vertical axis, Q_z with 35 nM nanoparticle concentration in the bulk water phase.

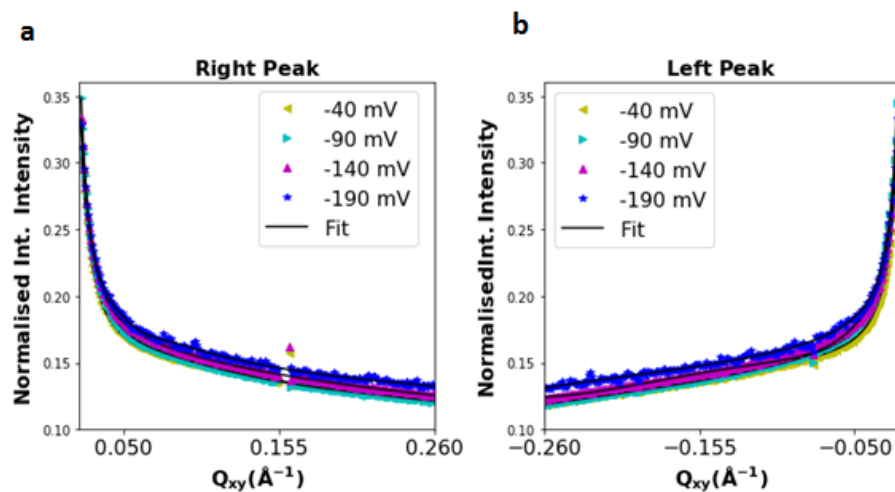


Figure 29. Integrated normalized GISAXS intensity fitted with Lorentzian functions and linear background along the vertical axis, Q_z with 35 nM nanoparticle concentration in the bulk water phase at negative potentials.

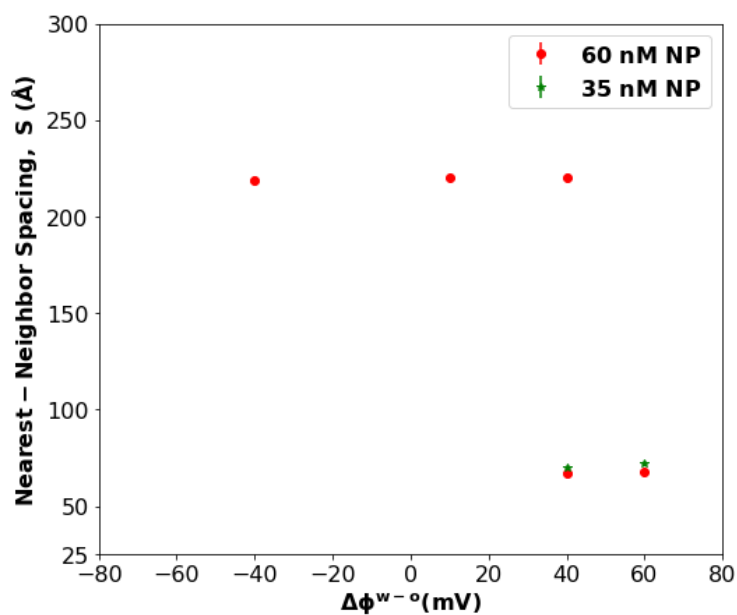


Figure 30. The nearest neighbour distance between nanoparticles with nanoparticle concentrations of 35 nM and 60 nM in the aqueous phase.

The results of the nearest neighbor distance is shown in Figure 30. The peak positions, in addition to the peak widths provide important information on the nearest neighbor distance and correlation (also known as coherence) length. The nearest neighbor distance, $S = 2d/\sqrt{3}$ where d is the lattice spacing defined as $d = 2\pi/Q_{[10]}$. The analyzed spacing in Figure 30 shows that nanoparticles nearest neighbor distance decreased from 60 mV to 40 mV indicating that nanoparticles come closer together as interfacial potential is decreased. Below the interfacial potential of 40 mV, separation distance increased significantly. The increased nearest neighbor distance could be due to the formation of a large particle formed from the single nanoparticles initially used. The nearest neighbor distance between the nanoparticles decreased from the interfacial potential of 60 mV to 40 mV corresponding to 67.7 Å and 66.9 Å respectively for the 60 nM nanoparticle concentration in the aqueous phase. Similarly, the nearest neighbor distance of the 60 mV and 40 mV of 35 nM nanoparticle concentration in the aqueous phase was estimated to be 72.2 Å and 70.2 Å respectively. At the interfacial potential of 40 mV of the 60 mM nanoparticle concentration, two different length scales at the interface exists based on the positions of the diffraction peaks. Small and large nanoparticles corresponding to $Q_{xy} \sim 0.109 \text{ \AA}^{-1}$ and $Q_{xy} \sim 0.33 \text{ \AA}^{-1}$ respectively. This means that some of the 2D nanoparticle have begun to form 3D structure (cluster).

The coherence length, ξ , was obtained from the width of the peaks and instrumental resolution of the detectors. The in-plane resolution of the CCD detector with square pixel of size (p_x) 60 μm x 60 μm and sample to detector distance of 3125 mm was estimated to be $2.81 \times 10^{-4} \text{ \AA}^{-1}$ using $2\pi p_x/(\lambda D_d)$. The in-plane resolution of the Pilatus detector whose pixel (square) size is 172 μm x 172 μm with sample to detector distance 2925 mm, was estimated to be $9.5 \times 10^{-4} \text{ \AA}^{-1}$. The symbols p_x , λ and D_d are the pixel sizes, X-ray wavelength and sample's center to detector distance respectively. To obtain the coherence length, the resolution of the

detector was subtracted from the width of the peak and the inverse of the result multiplied by 2π .

The plot of the coherence length as a function of the interfacial potential is shown in Figure 31:

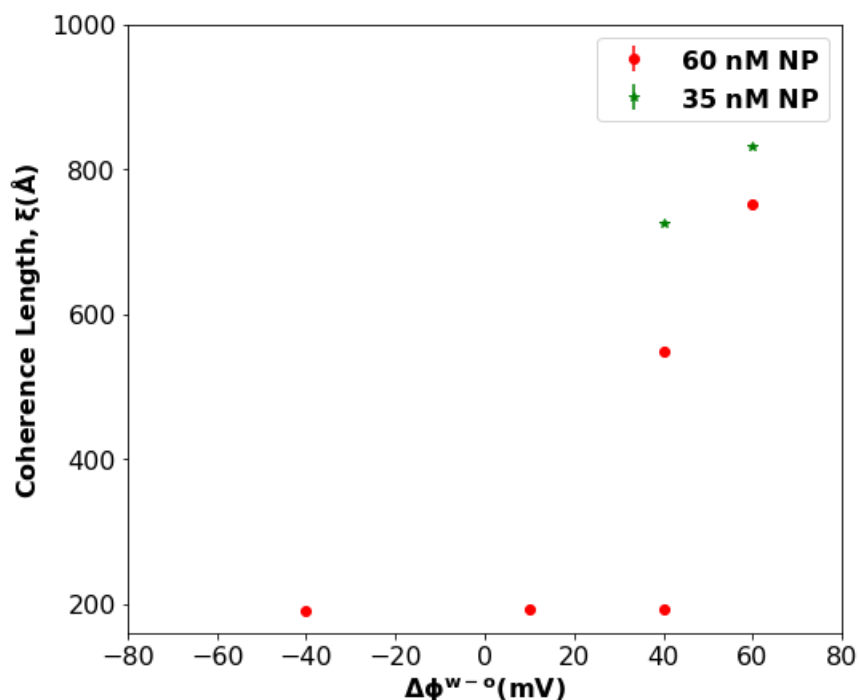


Figure 31. Coherence length as a function of interfacial potential.

The coherence shows the length scale at which domains at the interface are ordered. The Figure 31 shows that the coherence length of the ordering for the larger nanoparticles (with relatively large nearest neighbor distance) is less than the single nanoparticles (small nearest neighbor distance). That is, the 2D nanoparticles are more ordered than the 3D nanoparticles. Between the single nanoparticles (2D), the coherence length decreased with increased bulk concentration of the nanoparticles in the aqueous phase. The decrease in coherence length is possibly due to a transition from highly ordered states to less ordered states. Comparing the nearest neighbor distance to the coverage of the nanoparticles from the XR measurements and analysis (in the following chapters)

showed that with decreased interfacial potential, from 60 mV to 40 mV, the decreased nearest neighbor spacing correspond to increased nanoparticle coverage at the interface. For example, for bulk nanoparticle concentration of 60 nM, the nearest neighbor spacing decreased from 67.7 Å to 66.9 Å corresponding to increased nanoparticle coverage from ~ 90% to 100% at interfacial potentials of 60 mV to 40 mV respectively for a closed packed hexagonal unit lattice for a hexagonal nanoparticle. Similarly, with nanoparticle concentration in the bulk water phase of 35 nM, the nanoparticle's nearest neighbor distance changed from 72.2 Å to 70.2 Å corresponding to interfacial coverage of 81% to 91% at interfacial potentials of 60 mV to 40 mV respectively.

Beyond the interfacial potential of 40 mV, there was a dramatic change in the structure of the nanoparticle arrays from possibly a 2D structure to a 3D structure. The integrated intensities of the enhanced intensities at the low Q_{xy} at interfacial potentials below 40 mV were fitted to a spherical form factor of a nanoparticle whose average radius is ~ 30 Å .

The intensities were fitted to a functional form, $F(Q, r)$:

$$F(Q, r) = N(\Delta\rho)^2 \left(\frac{(\sin Qr - Qr)^2 P(r, R, R_{sig})}{(Q)^6} \right) / \sum P(r, R, R_{sig}) + bg \quad (5.2.2)$$

Where $P(r, R, R_{sig})$ is a lognormal distribution function, N is a scaling factor and $\Delta\rho$ is a scattering contrast between the nanoparticles and the solvent, r is the size of the nanoparticle, R is the probable size of the nanoparticle from the lognormal distribution, bg is background fit. Q is the wave vector which consists of the vertical component (Q_z) and horizontal component (Q_{xy}) wave vectors, where $Q = \sqrt{Q_{xy}^2 + Q_z^2}$. The Q_{xy} is the peak center obtained from the in-plane

GISAXS analysis and Q_z is the out-of-plane component from which the intensities were integrated. The plot of the fits and intensities as a function of Q_z is shown in Figure 32. In the fit, it was assumed that the scattering intensities is due to the form factor of the nanoparticles without a structure factor contribution.

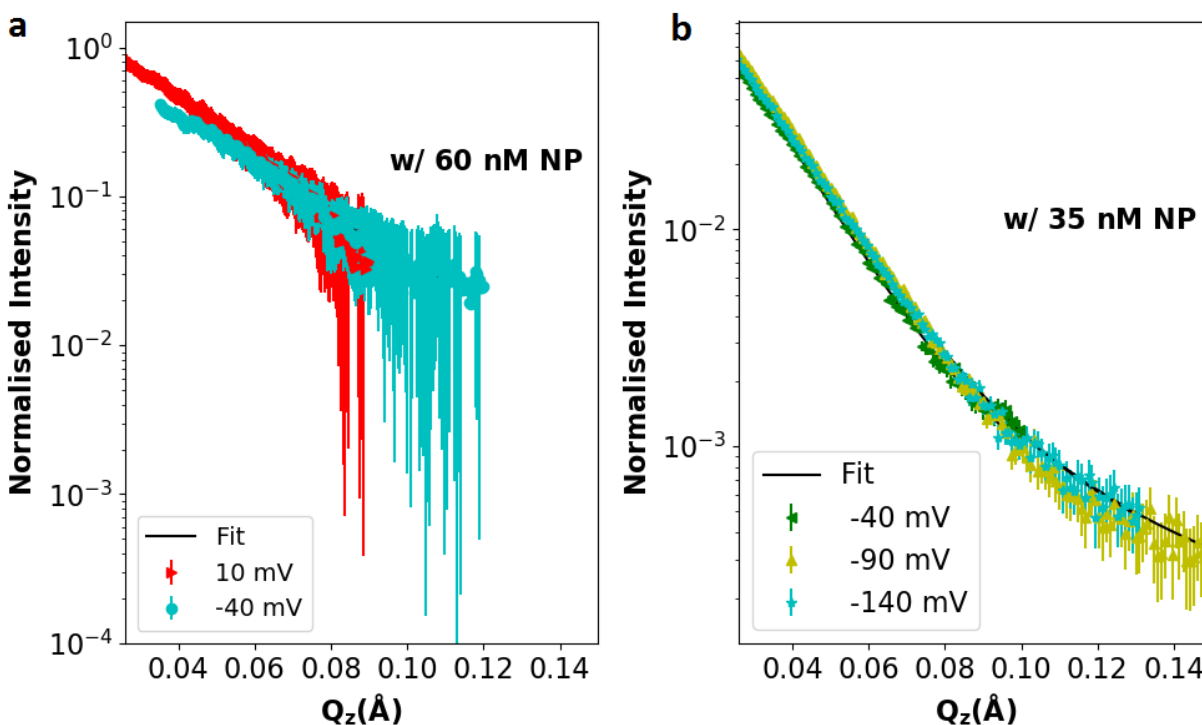


Figure 32. Fitted normalized integrated intensities a) concentration of 60 nM nanoparticles in aqueous phase b) concentration of 35 nM nanoparticles in aqueous phase.

The extracted form factors of the interfacial potentials and bulk nanoparticle concentrations in the aqueous phase is shown in Figure 33.

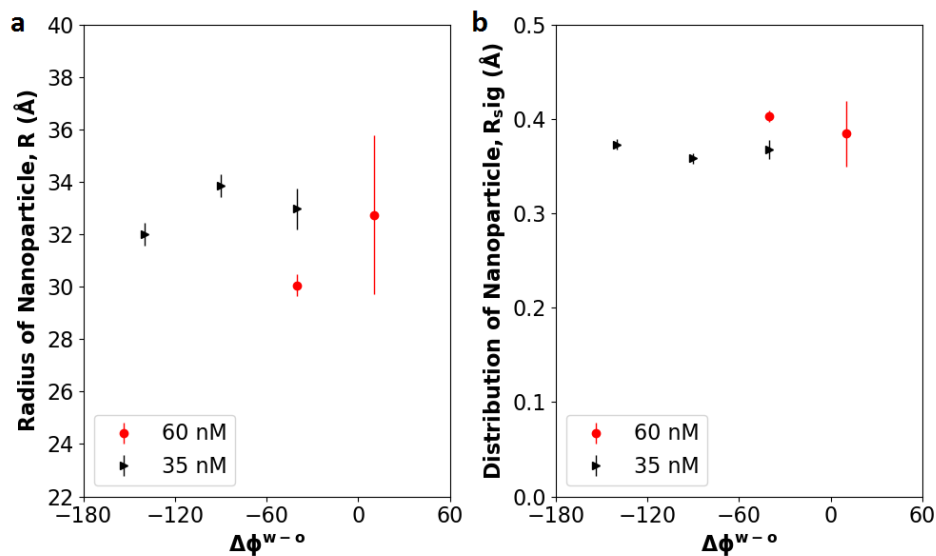


Figure 33.a) Form factors from fit b) Size distributions from fits.

The results of the extracted sizes from the fits is shown in Figure 33. Further analysis of the low Q_{xy} were done to find the scattering centers in the Q_{xy} and Q_z planes. The Figure 34 is the normalized intensity on a logscale.

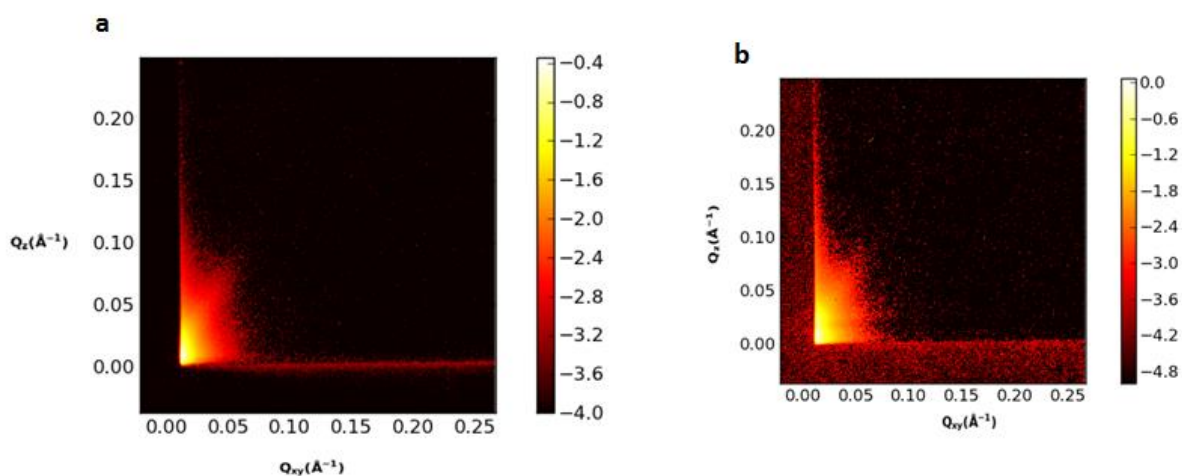


Figure 34: Normalized intensity at interfacial potentials a) 10 mV and b) -40 mV of 60 nM nanoparticle concentration in bulk phase. The plots are on a logscale.

The normalized intensity at the lower interfacial potential were integrated in a step of 0.001 \AA^{-1} for both the Q_{xy} and Q_z planes. C is the center from which the intensity was integrated. For example, in the vertical axis in Figure 35, $C=0.02$ means that integration of the intensity was done from 0.01 \AA^{-1} to 0.02 \AA^{-1} . In Figure 34, we fixed the horizontal axis's centers, Q_{xy} for a width of 0.001 \AA^{-1} at different centers and integrated the intensities along the vertical axis, Q_z .

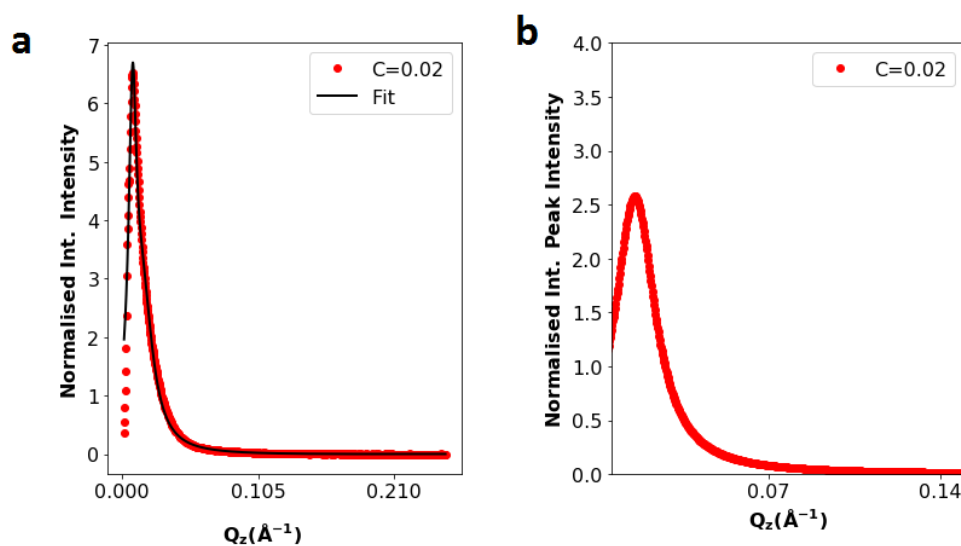


Figure 35. Fixed centers, C (Q_{xy}) b) Peaks from the fits of the integrated intensity at interfacial potential, 10 mV.

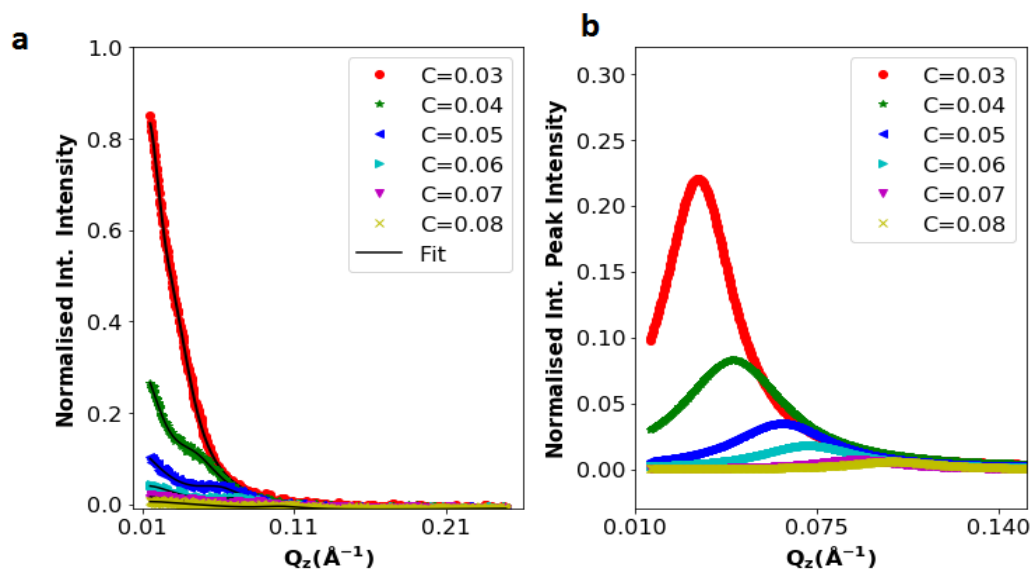


Figure 36. a) Fixed centers, C (Q_{xy}) b) Peaks from the fits of the integrated intensity at interfacial potential, 10 mV.

The peak centers and areas of the peaks from Figures 35 and 36 are shown in Figure 37. From the Figure 37, there is a gradual shift in the peaks' centers areas as a function of integration centres, C , while the peak areas decrease simultaneously.

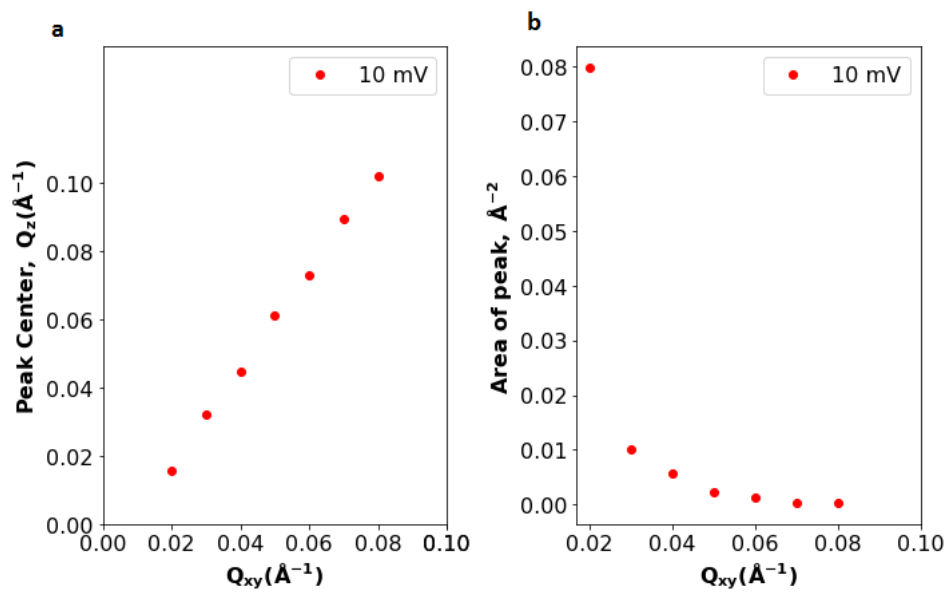


Figure 37. a) Peak centers versus fixed centers b) Area of peaks versus fixed centers

Similar analysis was obtained when the Q_z centers were fixed in step of 0.01\AA^{-1} and integration done over the horizontal axis, Q_{xy} at interfacial potential of 10 mV. The results of the analysis are shown in Figures 38 and 39 respectively.

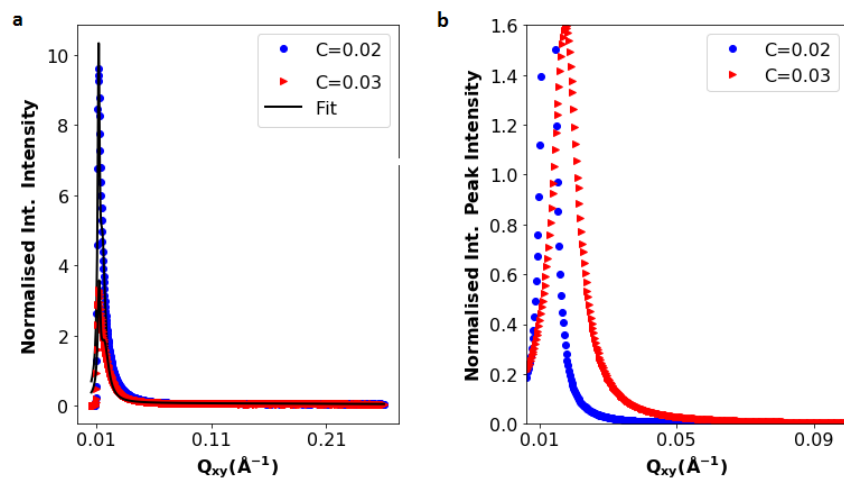


Figure 38. Fixed centers, $C(Q_z)$ b) Peaks from the fits at interfacial potential of 10 mV.

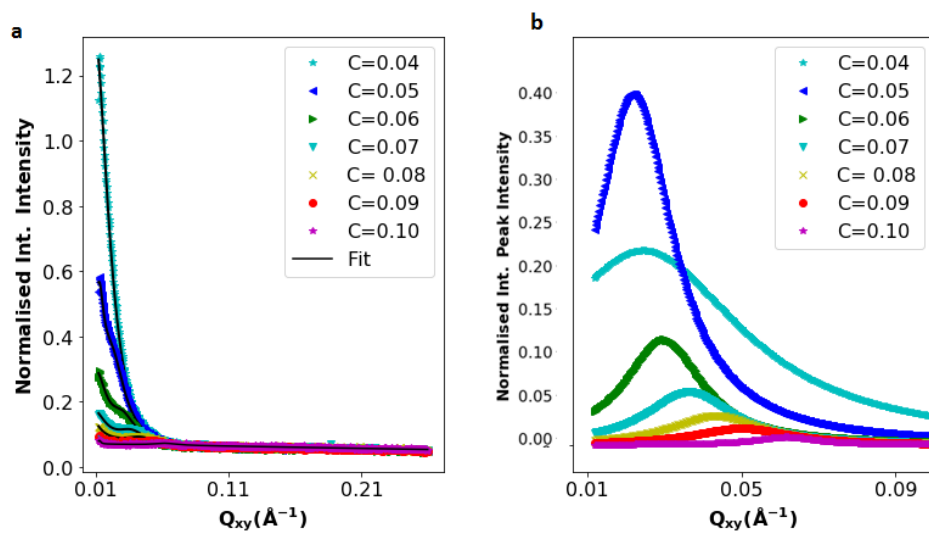


Figure 39.a) Fixed centers, $C(Q_z)$ b) Peaks from the fits at interfacial potential of 10 mV.

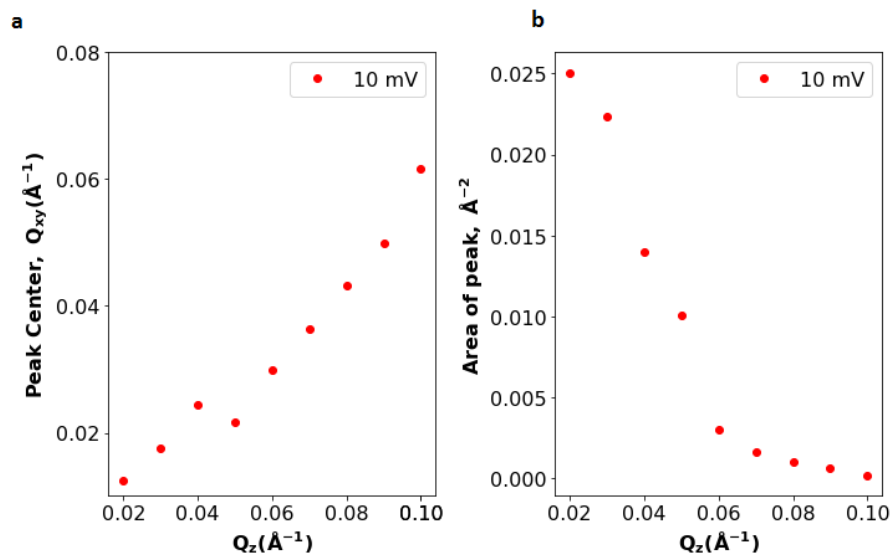


Figure 40. a) Peak centers versus fixed centers b) Area of peaks versus fixed centers at interfacial potential of 10 mV.

The corresponding peak centers and areas of the peaks of Figures 38 and 39 are shown in Figure 40. The results of Figures 37 and 40 of the peak center positions show that integrating the intensities in steps of 0.01 in both Q_z and Q_{xy} at interfacial potential of 10 mV are not symmetric.

Similar analyses were done at interfacial potential of -40 mV by fixing the vertical axis (Q_z) and integrating the intensity along the horizontal axis, Q_{xy} . The result of the analysis is shown in Figure 41 and the corresponding peak centers shown in Figure 42.

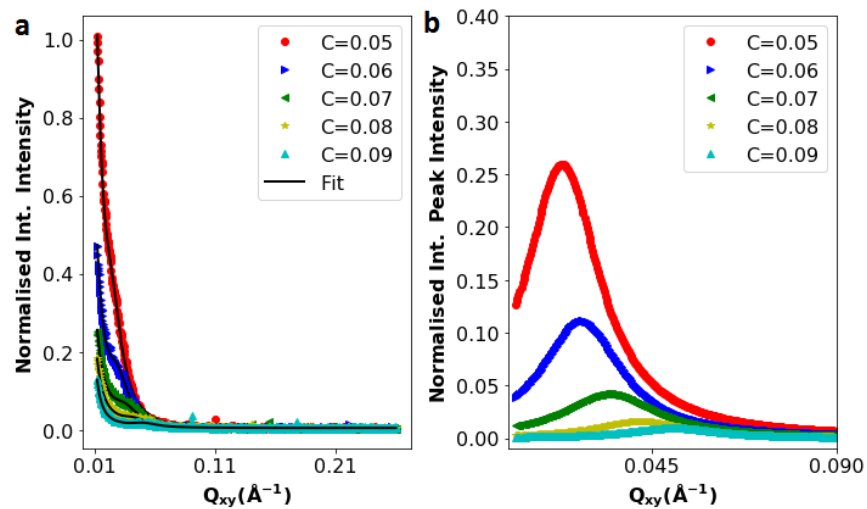


Figure 41. a) Fixed centers (Q_z) b) Area of peaks at interfacial potentials of -40 mV.

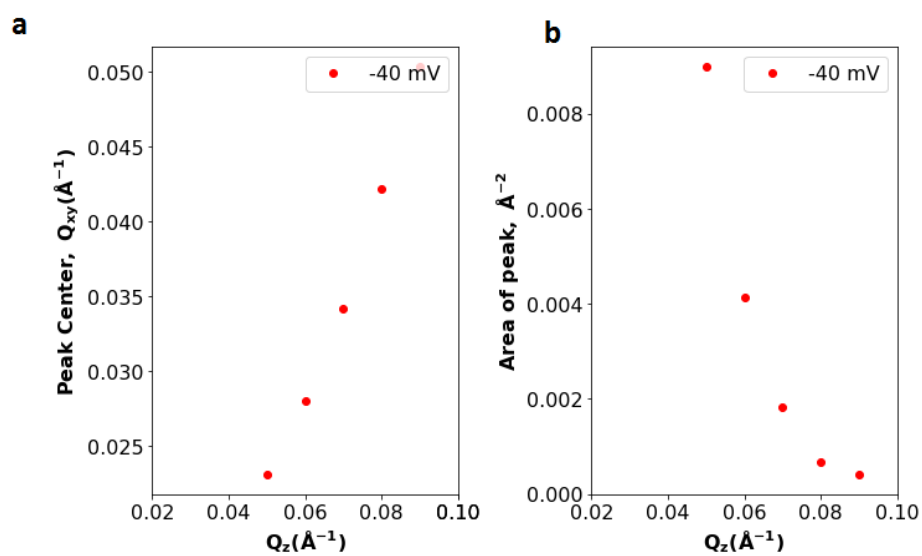


Figure 42. a) Peak centers versus fixed centers b) Area of peaks versus fixed centers at interfacial potential of -40 mV.

Like previous analysis, the vertical axis centre, Q_z at interfacial potential, -40 mV was fixed and the intensity integrated along the Q_{xy} plane. The results of the fits are shown in Figures 43, 44 and 45.

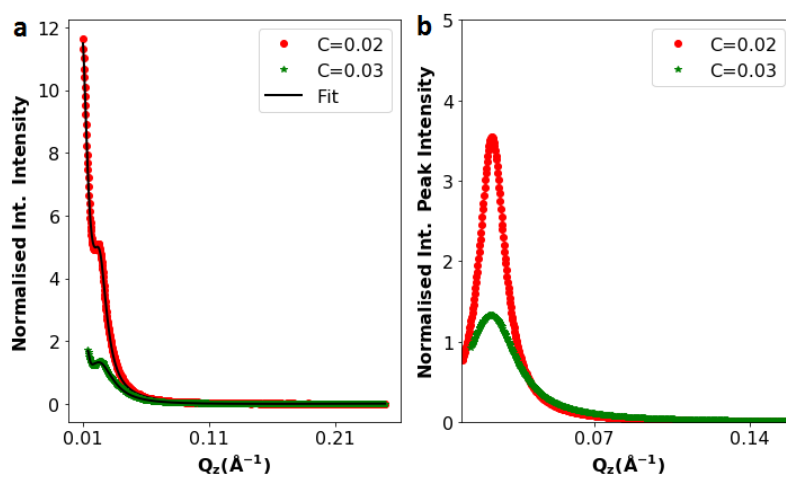


Figure 43. a) Fixed centers, $C(Q_{xy})$ b) Area of peaks at interfacial potential of -40 mV.

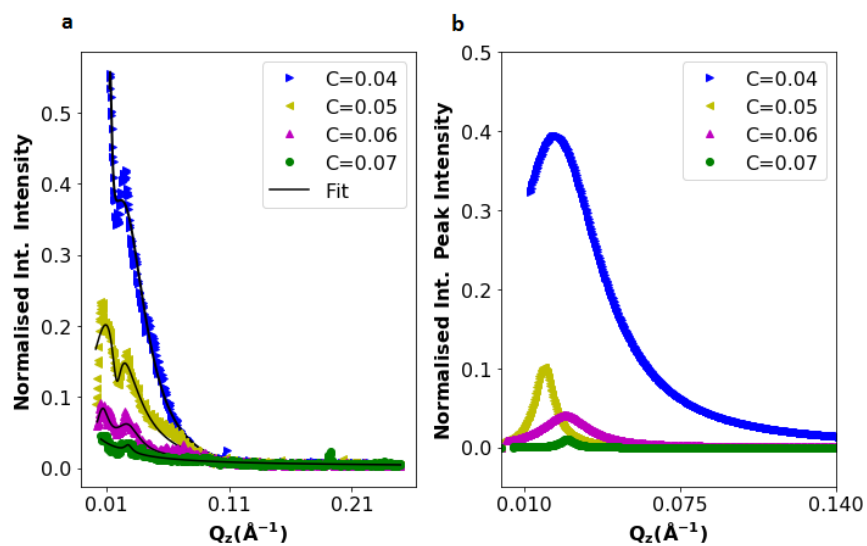


Figure 44. a) Fixed centers, $C(Q_{xy})$ b) Area of peaks at interfacial potential, -40 mV

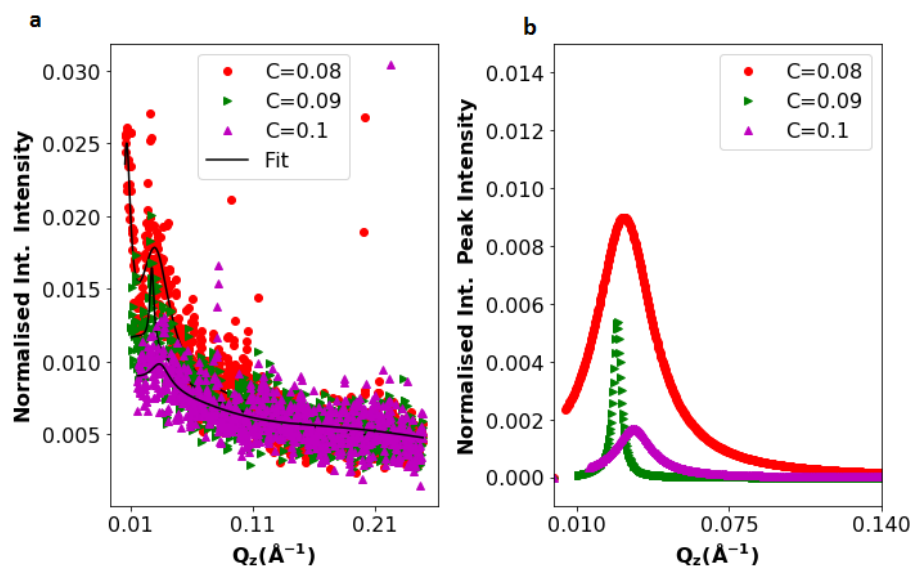


Figure 45. a) Fixed centers, $C(Q_{xy})$ b) Area of peaks at interfacial potential, -40 mV.

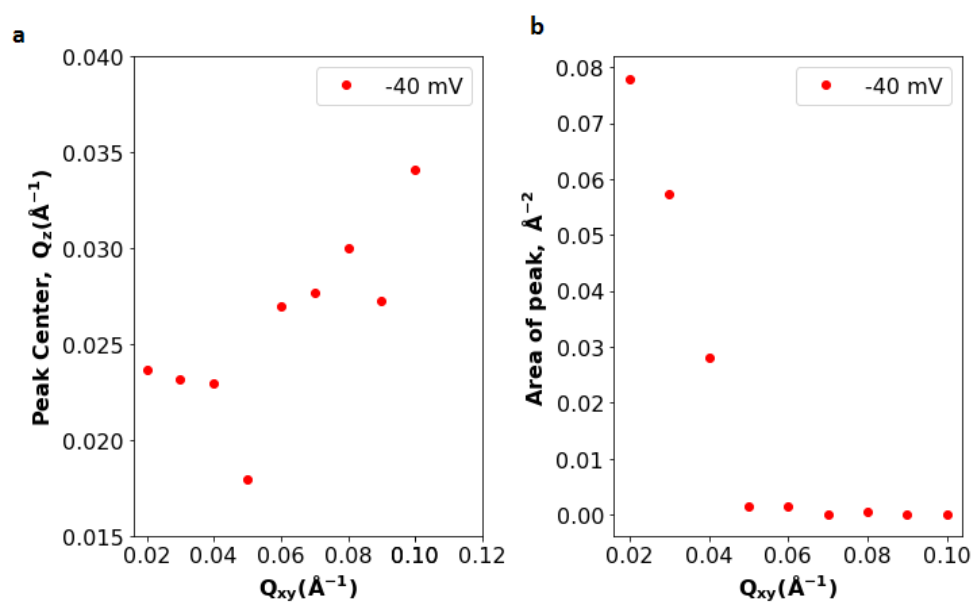


Figure 46. a) Peak center versus fixed center b) Area of peak versus fixed center at -40 mV.

The corresponding fit centers and peak areas of Figures 43, 44 and 45 are shown in Figure 46. In summary, the results of the analyses of the integrated centres at interfacial potentials of 10 mV and -40 mV show peak centres vary along the diagonal of the reciprocal space axes. Literature study of GISAXS analysis of the scattering intensities of particles is consistent with the form factor of a pyramidal structure (10, 109).

5.3 XR Measurements

The X-ray reflectivity, R_F from a flat water/DCE interface can be calculated as:

$$R_F(Q_z) = \left| \frac{Q_z - \sqrt{Q_z^2 - Q_c^2}}{Q_z + \sqrt{Q_z^2 - Q_c^2}} \right|^2 \quad (5.3.1)$$

The Fresnel reflectivity, $R_F(Q_z)$ is the reflectivity at a sharp flat interface (104). This Fresnel was used to normalize our reflectivity data (R) from the interface. The results of the normalised data is shown in Figure 47.

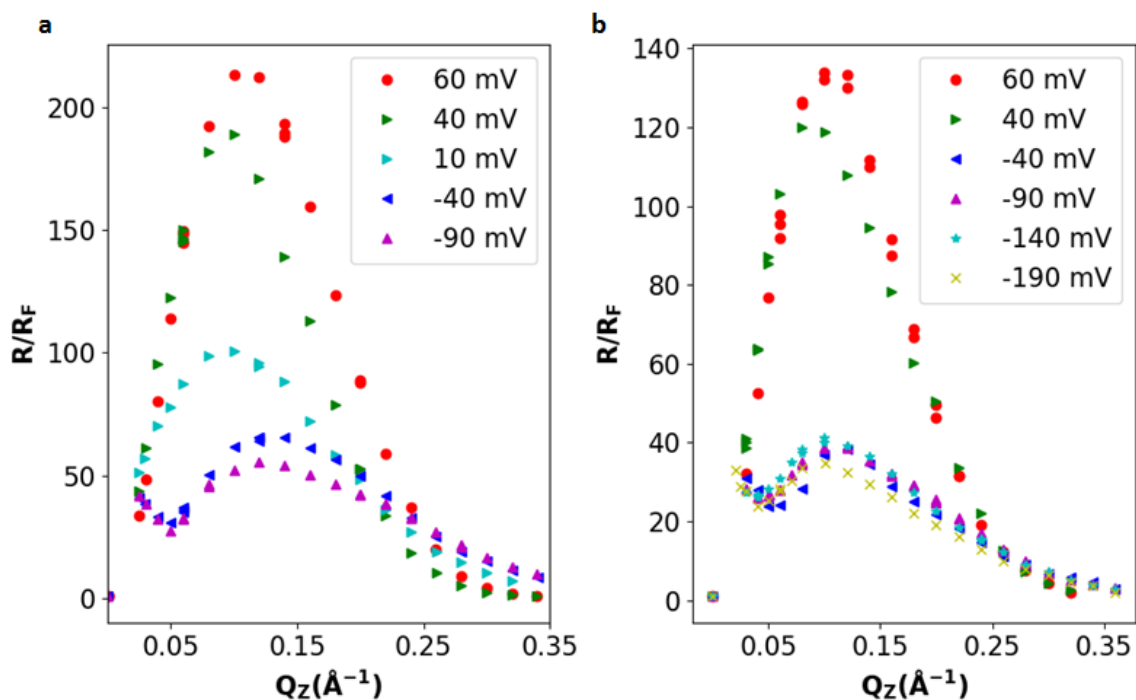


Figure 47. Fresnel (R_F) normalized reflectivity with a) 60 nM nanoparticle concentration in aqueous phase and b) 35 nM nanoparticle concentration in aqueous phase.

The results in Figure 47 show X-ray measurements for bulk nanoparticles in the aqueous phase. In the Figure 47, there are two peak positions. One peak position at high $Q_z \sim 0.1 \text{ \AA}^{-1}$ and another peak position at low $Q_z \sim 0.04 \text{ \AA}^{-1}$. These two peaks positions indicate two domain sizes. The peak position at the high Q_z represents a small nanoparticle while the peak position at low Q_z represents a large nanoparticle initially not present. From the Figure 47, there are two transitions where the interfacial potentials at 60 mV and 40 mV have a single peak and interfacial potentials from 10 mV and below have two peaks indicating two domain sizes. The analysis of the *XR* curves are explained in the following sections.

5.3.1 2D Spherical Nanoparticle Model Analysis

A 2D hexagonal closed packed (HCP) model of nanoparticles adsorbed at the water-DCE accounting for physical features at the interface is used. The physical features at the interface consist of the gold nanoparticle's core radius R , the lattice spacing, D , interfacial roughness, σ , the average position of the nanoparticle's center away from the interface, H , the coverage of the gold nanoparticles, C and the distribution of the nanoparticles' immersion depth, ξ . The height distribution function, $P(h)$ of the nanoparticles at the water/DCE interface is :

$$\begin{aligned}
 P(h) &= (N/xi) \exp((h - H)/\xi) \text{ for } H \leq 0 \text{ and } h \leq 0 \\
 &= \left(\frac{N}{xi}\right) \exp\left(\frac{H-h}{\xi}\right) \text{ for } H > 0 \text{ and } h > 0 \\
 &= 0 \text{ elsewhere}
 \end{aligned} \tag{5.3.1.1}$$

H is the most probable height of the nanoparticles and N is a normalisation constant. There is a thermally induced capillary wave fluctuation at the interface which also changes the depth of the nanoparticles at the interface. The capillary wave thermal fluctuation is a Gaussian distribution function of the form, $\exp(-z^2/2\sigma^2)/\sqrt{2\pi}\sigma$ which is used to convolute the functional form of the 2D nanoparticle's average electron density in equation (5.3.1.2). The interfacial roughness is estimated as follows:

$\sigma^2 = \frac{k_B T}{4\pi\gamma} \ln \left[\frac{q_{max}^2}{q_{res}^2} \right]$ for which $q_{max} = \frac{\pi}{r_A}$, $q_{res} = 2\pi/\lambda \Delta\alpha_d \sin \alpha_i$, $\Delta\alpha_d = l/D_S = 5.6 \times 10^{-4} \text{ \AA}^{-1}$. $\Delta\alpha_d$ is the vertical angular acceptance of the CCD detector, l is the vertical electronic slit, $30 \times 60 \text{ \mu m}^2$ ($V \times H$) which defines the resolution of the detector and D_S is the distance from the sample's center to the detector. The angular resolution of the Pilatus detector is $9.5 \times 10^{-4} \text{ \AA}^{-1}$

while the angular resolution of the CCD detector is $2.81 \times 10^{-4} \text{ \AA}^{-1}$. Typically, r_A is the average radius of the molecules at the interface, for example, water molecules at the interface. The average electron density at the interface is a contribution of the solvent and the nanoparticles in a hexagonal lattice. Bera et. al. studying a similar system, showed that the contribution of the nanoparticle's ligand to the reflectivity is negligible compared with the solvent in which the nanoparticle is immersed (45). The average electron density, $\langle \rho(z) \rangle$ is given as:

$$\begin{aligned} \langle \rho(z) \rangle = & (100 - C)/100 (1 - f(z))\rho_s(z) \\ & + C \left(\frac{2\pi\rho_P f(z)[R^2 - (z - h)^2]}{\sqrt{3}D^2} \right) \otimes P(h) \\ & + C \left(\frac{\sqrt{3}\rho_s(z)D^2}{\sqrt{3}D^2} \right) \otimes P(h) \end{aligned} \quad (5.3.1.2)$$

Where ρ_s is the electron density of the solvent (DCE or water) depending on the position of the nanoparticles, H and $f(z) = 1$ for $h - R < z < h + R$ else $f(z) = 0$. The average density, $\langle \rho(z) \rangle$, is convoluted with the interfacial roughness, σ . The first term of equation (5.3.1.2) on the right accounts for the part of the interface not covered by the nanoparticles. The second term accounts for the nanoparticles in a HCP lattice. The third term accounts for the part of the solvent within the nanoparticle's HCP lattice, $f(z)$ is a Boolean operator satisfying the depth of the nanoparticles. The size of the nanoparticle, R , the roughness, σ together with the electron densities of the solvents are variable's known where R is 12 \AA ; σ is calculated from interfacial tension measurements. The electron densities of the solvents, $\rho_{DCE} = 0.38 e^-/\text{\AA}^3$ and $\rho_w = 0.333 e^-/\text{\AA}^3$ where ρ_{DCE} is the electron density of the DCE and ρ_w is the electron density of the water. The electron density of the nanoparticles, $\rho_P = 4.65 e^-/\text{\AA}^3$. The size of the nanoparticle,

R , used in fitting the 2D reflectivity is 12 Å. Although this is not the most probable radius from the TEM fit, which was approximately ~ 10 Å, our model would only fit with radii of 12 Å and 13 Å. Any size greater than 13 Å or less than 12 Å would not fit our reflectivity data accurately. When the radius in the model was allowed to fit freely, we obtained values between 12 Å and 13 Å. Here we fix the average size of the nanoparticles' radius to be 12 Å at all interfacial potentials for the 2D analysis. Our simple calculation showed that the energy gain in using 12 Å is significant when compared with 10 Å. Using the energy of adsorption equation, ΔE (72):

$$\Delta E = -\pi R^2 / \gamma_{O/W} [\gamma_{O/W} - (\gamma_{P/W} - \gamma_{P/O})]^2 \quad (5.3.1.3)$$

Which reduces to $\Delta E = -\pi R^2 [1 - \cos \theta]^2$ using Laplace-Young equation (79, 110) :

$$\theta = (\gamma_{P/W} - \gamma_{P/O}) / \gamma_{O/W} \quad (5.3.1.4)$$

Where $\gamma_{O/W}$ is the interfacial tension between the oil (DCE) and water, $\gamma_{P/W}$ is the interfacial tension between the nanoparticle and water and $\gamma_{P/O}$ is the interfacial tension between the nanoparticle and oil.

Assuming the contact angle for 10 Å and 12 Å sizes are the same, there is about 40% gain in energy when 12 Å is used instead of 10 Å. Hence, the interface can select the 12 Å particles over smaller nanoparticles at the interface to attain the most stable equilibrium condition. We did not consider 13 Å. Our size distribution from the TEM analysis shows that the amount of 13 Å

nanoparticles may not be sufficient for a full monolayer. The number of 13 Å nanoparticles from our TEM analysis is less than 30 nanoparticles from the total distribution.

Using Parratt Algorithm (107) for multilayer analysis and choosing 1 Å thick of each layer over a range of depth, Z , the reflectivity data was fitted with the reflectivity model. We fixed parameters D and R (obtained from the GISAXS and TEM respectively), the electron density of the gold nanoparticles, $\rho_p = 4.65 e^-/\text{Å}^3$, the electron density of the water, $\rho_w = 0.333 e^-/\text{Å}^3$ and the electron density of the DCE, $\rho_{DCE} = 0.38 e^-/\text{Å}^3$. Our model, M , has the parameters, $M = f(R, D, H, C, \rho_p, \rho_w, \rho_{DCE}, \sigma, \xi)$. The unknown parameters H, C and ξ would be obtained from the fits. Even though, σ can also be estimated from the interfacial tension measurements, we considered it a fitting parameter and compared it with the estimated parameter value from the capillary wave function. The results of our fitted X-ray reflectivity is shown in Figure 48.

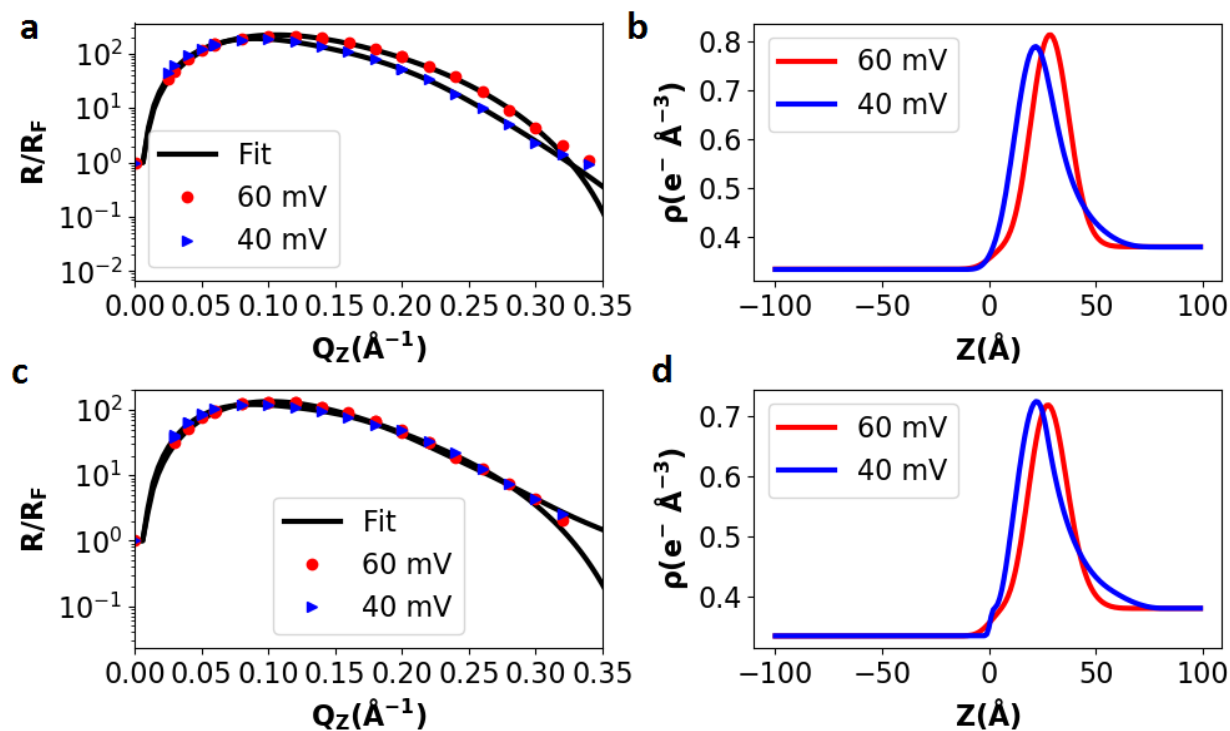


Figure 48. a) X-ray data and fit with 60 nM nanoparticle concentration in aqueous phase. b) Corresponding electron density profile from fit of 60 nM nanoparticle concentration in aqueous phase. c) X-ray data and fit with 35 nM nanoparticle concentration in aqueous phase. d) Corresponding electron density profile from fit of 35 nM nanoparticle concentration in aqueous phase.

TABLE II. FIT PARAMETERS OF 2D ARRAYS OF NANOPARTICLES WITH 60 nM NANOPARTICLE CONCENTRATION IN BULK WATER PHASE.

$\Delta\phi^{w-o}$ (mV)	D (\AA)	H (\AA)	C (%)	ξ (\AA)	σ_{Fit} (\AA)	σ (\AA)
60	58.6	26.5(6)	90.9(6)	4.5(5)	5.5(1)	4.25
40	57.9	15.6(3)	100(1)	11.2(6)	3.9(2)	4.62

TABLE III. FIT PARAMETERS OF 2D ARRAYS OF GOLD NANOPARTICLES WITH 35 nM NANOPARTICLE CONCENTRATION IN BULK WATER PHASE

$\Delta\phi^{w-o}$ (mV)	D (Å)	H (Å)	C (%)	x_i (Å)	σ_{Fit} (Å)	σ (Å)
60	62.5	23.4(7)	81.7(8)	6.1(2)	4.75(2)	4.1
40	60.77	15.4(5)	91(1)	13.3(6)	1.0(8)	4.3

The fit parameters of the 2D model are shown in TABLES II and III. The results show that as the concentration of the bulk phase nanoparticles increased, the interfacial coverage of the nanoparticles increased. Considering the interfacial coverage for the same interfacial potential but different bulk nanoparticle concentration, the change in interfacial coverage is about 10% more for the 60 nM bulk nanoparticle concentration relative to the 35 nM bulk nanoparticle concentration. The nanoparticles positions, H remained almost the same for the different amount bulk phase nanoparticle concentrations of nanoparticles used. The decay lengths which describe the distribution of the immersion depths of the nanoparticles remained almost the same for the different bulk phase concentration of nanoparticles used.

On the other hand, the positions, coverages and decay lengths changed significantly when the potentials were changed for each bulk phase nanoparticle concentration. For example, for the bulk phase nanoparticle concentration of 60 nM, the nanoparticles' position changed from 26 Å to 15 Å when the interfacial potential was tuned from 60 mV to 40 mV. Similarly, for the bulk phase nanoparticle concentration of 35 nM, the nanoparticle's position changed from 23 Å to 15 Å corresponding to interfacial potentials of 60 mV and 40 mV respectively.

On the nanoparticle's coverage, the interfacial coverage increased with decreased interfacial potential for all the bulk phase concentrations. In the GISAXS analyses, increased coverage was accompanied with decreased nearest neighbour distance between the nanoparticles. The immersion height distributions of the nanoparticles also increased with decreased interfacial potential. Similar model would be used to address the supposed cluster (3D) reflectivity data.

5.3.2 3D Spherical Nanoparticle Model Analysis

We consider a single nanoparticle and cluster nanoparticles at the interface. The single nanoparticle will have a functional form of the electron density similar to the equation 5.3.1.2. used in the 2D analysis. The functional form of the electron density of the 3D structure is:

$$\begin{aligned}
 \langle \rho(z) \rangle_1 = & \left[\frac{(100 - C1)}{100} (1 - f(z)) \rho_s(z) \right] \\
 & + C1 \left(\frac{2\pi \rho_c f(z) [R_1^2 - (z - h^*)^2]}{\sqrt{3} D_1^2} \right) \otimes P(h^*) \\
 & + C1 \left(\frac{\sqrt{3} \rho_s(z) D_1^2}{\sqrt{3} D_1^2} \right) \otimes P(h^*)
 \end{aligned} \tag{5.3.2.1}$$

Where $C1$ is the coverage of the 3D cluster. R_1 is a spherical radius of the cluster, ρ_c is the electron density of the cluster, D_1 is the lattice spacing of the cluster which was obtained from the GISAXS analysis, h^* is the height of the cluster. The probable height of the cluster is H^* .

We assume a number of scenarios at which the single nanoparticles and the cluster adsorb at the interface:

- (i) The 2D and 3D nanoparticles are homogenously and the average of their electron density estimated. We add weights contributions, α_1, α_2 and $1-\alpha_1 - \alpha_2$ for the 3D, 2D and bare interface respectively.

Then the average electron density for both the cluster and single nanoparticle is:

$$\begin{aligned}
\langle \rho(z) \rangle = & \left[\frac{(100 - C_1)}{100} (1 - f(z)) \rho_s(z) \right] * \alpha_1 \\
& + \left(\frac{2\pi \rho_c f(z) [R_1^2 - (z - h^*)^2]}{\sqrt{3} D_1^2} \right) \otimes P(h^*) * \alpha_1 \\
& + \left(\frac{\sqrt{3} \rho_s(z) D_1^2}{\sqrt{3} D_1^2} \right) \otimes P(h^*) * \alpha_1 \\
& + \frac{(100 - C)}{100} (1 - f(z)) \rho_s(z) * \alpha_2 \\
& + \left(\frac{2\pi \rho_p f(z) [R^2 - (z - h)^2]}{\sqrt{3} D^2} \right) \otimes P(h) * \alpha_2 \\
& + \left(\frac{\sqrt{3} \rho_s(z) D^2}{\sqrt{3} D^2} \right) \otimes P(h) * \alpha_2 \\
& + \rho_s(z) * (1 - \alpha_1 - \alpha_2)
\end{aligned} \tag{5.3.2.2}$$

The first three terms (1-3) are contributions to the reflectivity from the cluster. The next 4-6 terms on the right are the contributions to the reflectivity from the single nanoparticle. Then the last term is a contribution to the reflectivity from the bare interface. We consider three possibilities in analyzing the 3D structure.

Then we use Parratt algorithm to calculate the overall reflectivity. In the second case, we

(ii) Calculate the reflectivity each using their electron densities in equations 5.3.1.1 and 5.3.2.1 in addition to the reflectivity for bare interface. Thus, the single nanoparticle (R_P), the cluster (R_C) and the bare interface (R_S) and weigh their contributions to the overall reflectivity, R . Thus, $R = \alpha_1 R_C + \alpha_2 R_P + (1 - \alpha_1 - \alpha_2) R_S$.

(iii) The third case is similar to case (ii) except that we calculate the reflectivity amplitudes of the single nanoparticle (r_p), cluster (r_c) and bare interface, (r_s) instead of the reflectivity. We then weigh their contributions to the overall reflectivity amplitudes, r .

That is, $r = \alpha_1 r_c + \alpha_2 r_p + r_s(1 - \alpha_1 - \alpha_2)$.

To obtain the reflectivity, we multiply the total amplitude of reflectivity from the Parratt calculation, r , and the conjugate of the amplitude of reflectivity, r^* .

Our model for the cluster is of the form, $M = f(R, R_1, D, D_1, H, H^*, C, C_1, \rho_c, \rho_p, \rho_w, \rho_{DCE}, \sigma, \xi, \xi^*, \alpha_1, \alpha_2)$. There are 17 parameters and $R, \rho_p, \rho_w, \rho_{DCE}, \sigma, D_1$ are known. We did mesh calculation to find the global minimum of some of the unknown parameters using chi square calculated from the reflectivity model and data. By knowledge of the chi-square values, we fixed some of the unknown parameters to reduce the number of unknown parameters. For example, Figures 49 show a mesh calculation performed to find the range of global parameter space of the size of the cluster and the position of the cluster with the least chi-square values.

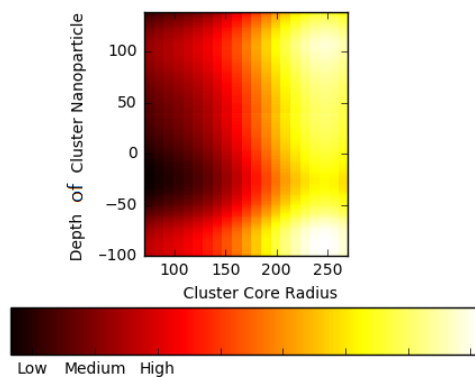


Figure 49. Mesh calculation of size versus depth (position).

To obtain Figure 49, we fixed all the other variables and varied the position, H^* , of the cluster and the size, R_l , of the cluster. It can be seen that the upper limit of the size of the cluster favourable and possibly physical to the model is $\sim 150 \text{ \AA}$ and below. Another example of mesh calculation is shown in Figure 50.

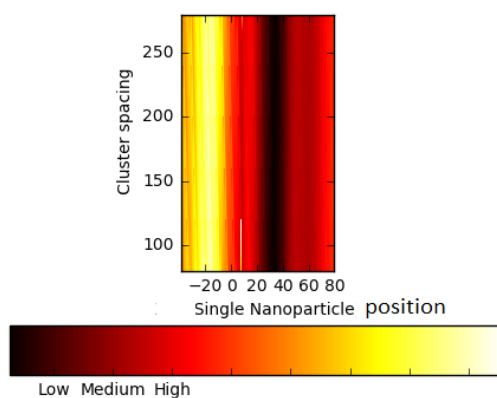


Figure 50. Mesh calculation of size of cluster versus depth (position) of single nanoparticle.

The result of the mesh calculation in Figure 50 for the position of the single nanoparticle and the cluster spacing shows that the position, H , of the single nanoparticle must be between 20 Å and 40 Å. Based on the mesh calculations, we fixed the position of the single nanoparticle to be ~ 20 Å at all interfacial potentials in the 3D analysis. We also fixed the lattice spacing (~ 59 Å) of the single nanoparticles for all interfacial potentials. Fitting the model with a 12 Å single nanoparticle gave the following reflectivity and electron density profile in Figure 51.

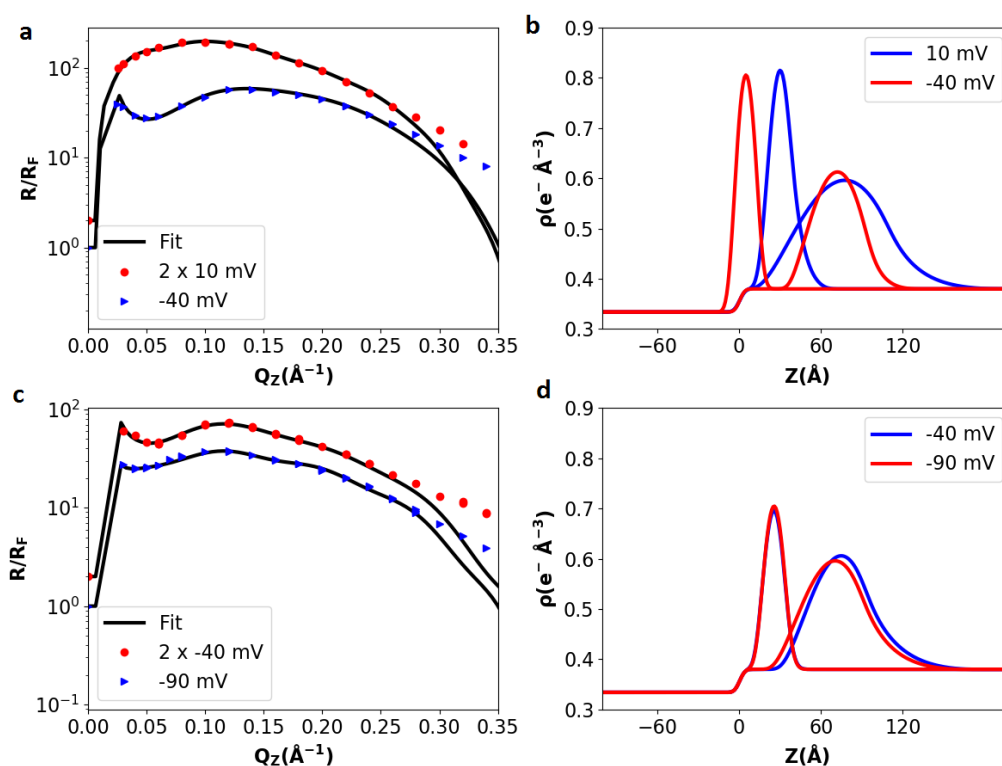


Figure 51. 3D model XR fit a) 60 nM nanoparticle concentration in bulk phase b) Corresponding electron density profile from the fit of the 60 nM nanoparticle concentration in bulk phase c) 35 nM nanoparticle concentration in the bulk phase d) Corresponding electron density profile from the fit of the 35 nM nanoparticle concentration in bulk phase.

The fit in Figure 51 is a structure of an inhomogeneous two phase system where the 2D nanoparticles are isolated from the 3D nanoparticles. The model does not fit well at the high Q_z when a 3D spherical nanoparticle cluster was assumed. The narrow width of the electron density profile corresponds to the 2D nanoparticle while the broader and shorter electron density corresponds to the 3D structure.

The size of the nanoparticle that fitted the XR data for interfacial potential of 10 mV from Figure 51 of the 60 nM nanoparticle concentration in the aqueous bulk phase was $\sim 48 \text{ \AA}$ while the size (radius) that fitted the XR at interfacial potential of -40 mV was $\sim 30 \text{ \AA}$. For sample 35 nM of nanoparticle concentration in the aqueous phase, the average cluster size that fitted the XR data was $\sim 34 \text{ \AA}$ at interfacial potential of -40 mV while the average cluster size that fitted the XR data at interfacial potential of -90 mV was $\sim 34 \text{ \AA}$.

When an average size of the single nanoparticle $\sim 10 \text{ \AA}$ was considered, the XR reflectivity data fitted slightly better than in Figure 51 at the high Q_z as shown in Figure 52. However, we cannot use different sizes for the 2D model and 3D model.

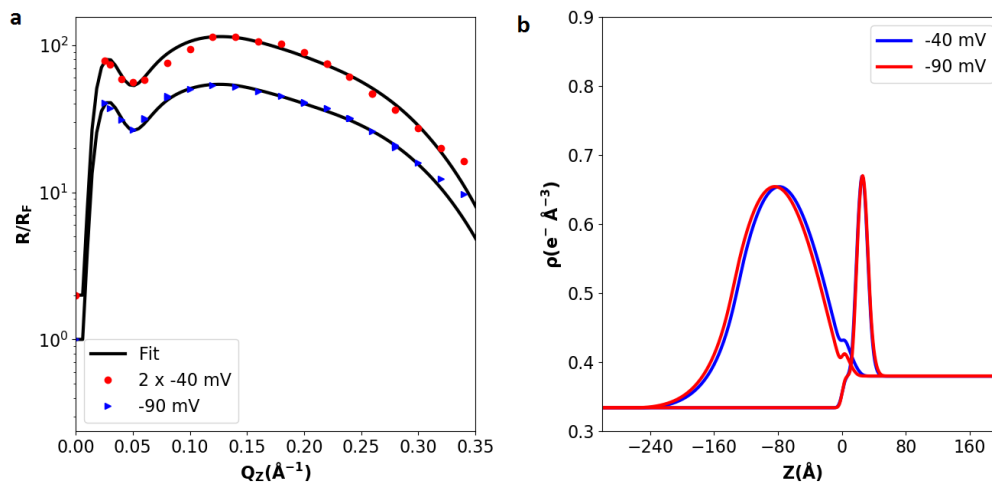


Figure 52. a) X-ray reflectivity fit at interfacial potentials -40 and -90 mV of 60 nM nanoparticles in bulk phase b) Corresponding electron density from fit with nanoparticle's average size ~ 10 \AA .

We propose a new model where clusters are considered as diffused single nanoparticles. We use a Gaussian function to describe the immersion distribution depth of the nanoparticles at the interface for each slab of nanoparticle layer considered. A cartoon of the diffused nanoparticles co-existing with single nanoparticles is shown in Figure 53.

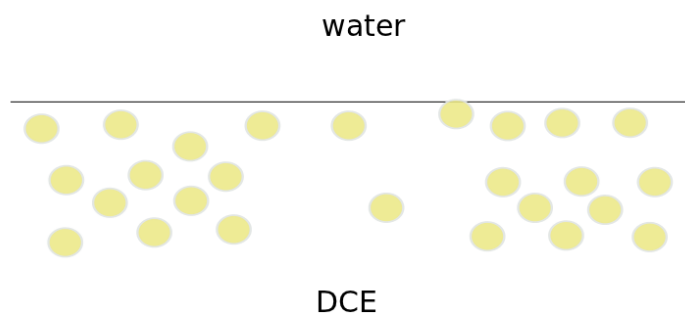


Figure 53. Diffused assembly of single nanoparticles as clusters at the interface.

The model does not discriminate on the position of the nanoparticles. However, for the sake of explanation, the nanoparticles have been shown to adsorb on the DCE of the interface as in Figure 53. It could also be on the water side of the interface. We use multilayer slabs in analysing the diffused layer model with each slab consisting of a 2D spherical nanoparticle and a Gaussian distribution function of their positions at the interface. The Gaussian immersion distribution function, $P(h)$ is of the form:

$$P(h) = \left(\frac{N}{\xi}\right) \exp\left(-\frac{1}{2}\left(\frac{h-H}{\xi}\right)^2\right) \quad (5.3.2.3)$$

The results of the fit is shown in Figure 54. In the Figure 54, it can be seen that the Gaussian distribution function provides a symmetric electron density profile in both the water phase and the DCE phase which does not represent the physical characteristic of the adsorbed nanoparticle at any side of the interface. The Gaussian function cannot discriminate a nanoparticle in water (negative part of the z-axis) or DCE (positive part of the z-axis) for a wide distribution of nanoparticle clusters.

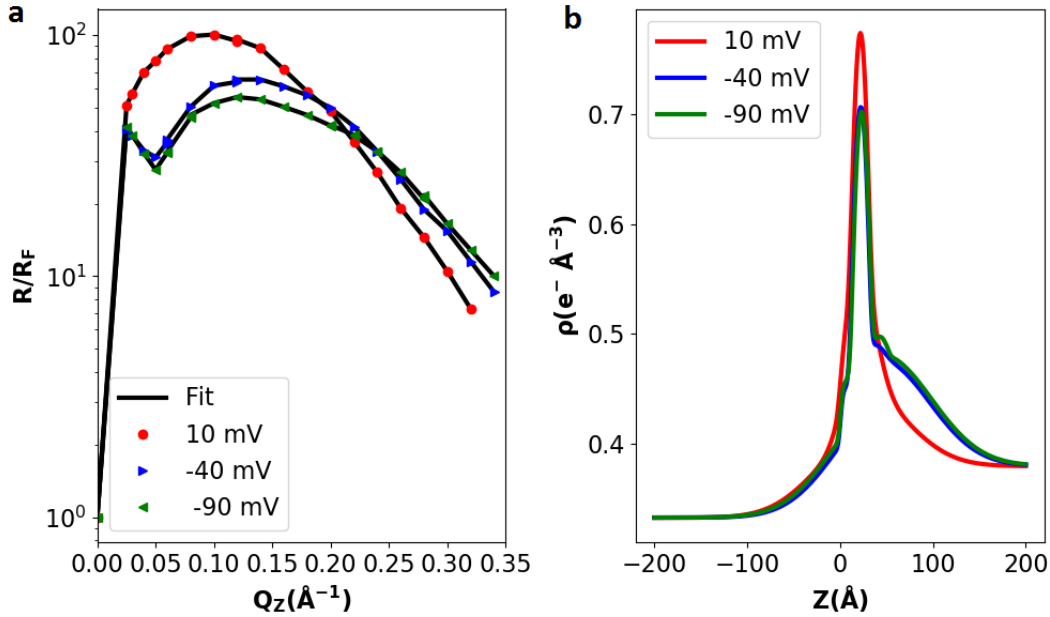


Figure 54. a) XR reflectivity fit with a Gaussian depth distribution function of 60 nM nanoparticle concentration in the bulk aqueous phase. b) Corresponding electron density profile from fit.

5.3.3 Slab Model

A generic slab model is proposed to model the reflectivity data from interfacial potential from 10 mV and below. The average electron density profile, $\langle \rho(z) \rangle$, of the structure (s) is a sum of error functions of the form:

$$\langle \rho(z) \rangle = \frac{1}{2} \sum_{i=0}^{N-1} \operatorname{erf} \left(\frac{z-z_i}{\sqrt{2}\sigma_i} \right) (\rho_i - \rho_{i+1}) + \frac{\rho_o + \rho_w}{2} \quad (5.3.3.1)$$

where $\operatorname{erf}(z) = (2/\sqrt{\pi}) \int_0^z 2/\sqrt{\pi} \int_0^2 e^{-t^2} dt$, N is the number of internal interfaces, ρ_i is the electron density of slab i with $\rho_o = 0.38 \text{ e}^-/\text{\AA}^3$ and $\rho_w = 0.333 \text{ e}^-/\text{\AA}^3$, z_i is the i th position of the internal layer at the interface and σ_i is the corresponding roughness of the i th layer. The

thickness d_i , is defined as $|z_i - z_{i-1}|$. Parratt formalism was used to calculate the reflectivity. We used three slabs in the model, which gave the best fit and the corresponding average electron density of the three slabs is:

$$\begin{aligned} \langle \rho(z) \rangle = & \frac{1}{2}(\rho_1 - \rho_w) \operatorname{erf} \left(\frac{z}{\sqrt{2}\sigma_0} \right) + \frac{1}{2}(\rho_1 - \rho_2) \operatorname{erf} \left(\frac{z - L_2}{\sqrt{2}\sigma_1} \right) \\ & + \frac{1}{2}(\rho_2 - \rho_{DCE}) \operatorname{erf} \left(\frac{z - L_1 - L_2}{\sqrt{2}\sigma_2} \right) + \frac{1}{2}(\rho_w + \rho_{DCE}) \end{aligned} \quad (5.3.3.2)$$

σ_0 is the roughness between the water phase and domain size $L1$, σ_1 is the roughness between the domain sizes $L1$ and $L2$, σ_2 is the roughness between domain $L2$ and DCE.

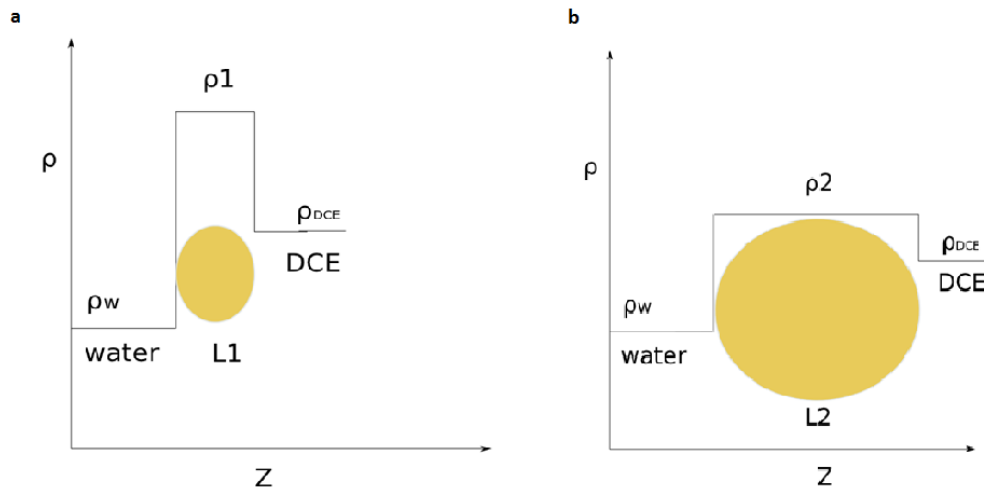


Figure 55. Slab model for XR analysis a) domain size, $L1$ b) domain size, $L2$

The Figure 55 shows a cartoon of the domains $L1$ and $L2$ at the interface. The variables-roughness (σ), the domain sizes (L) and electron densities (ρ) -were fitting parameters except the electron densities of the water and DCE, which were fixed. The results of the fitted parameters of this model are summarized in Tables IV and V.

TABLE IV. FIT PARAMETERS OF SLAB MODEL WITH 60 nM NANOPARTICLE CONCENTRATION IN BULK WATER PHASE.

$\Delta\phi^{w-o}$ (mV)	L_1 (Å)	L_2 (Å)	H (Å)	ρ_1 ($e^-/\text{Å}^3$)	ρ_2 ($e^-/\text{Å}^3$)	σ_0 (Å)	σ_1 (Å)	σ_2 (Å)
60	9.2	28	4.7	1.46(2)	0.42(4)	8.5	8.5	8.5
40	7.7	28.7	5.7	1.65(2)	0.42(4)	8.5	8.5	8.5
10	15.1	36.1	9.0	0.86(2)	0.55(5)	5.3	14.8	38.5
-40	11.88	87.3	7.0	0.76(9)	0.51(2)	4.5	8.9	46.3
-90	8.499	100.8	7.7	0.75(6)	0.50(2)	4.2	16.5	40.5

TABLE V. FIT PARAMETERS OF SLAB MODEL WITH 35 nM NANOPARTICLE CONCENTRATION IN BULK WATER PHASE.

$\Delta\phi^{w-o}$ (mV)	L_1 (Å)	L_2 (Å)	H (Å)	ρ_1 (e ⁻ / Å ³)	ρ_2 (e ⁻ / Å ³)	σ_0 (Å)	σ_1 (Å)	σ_2 (Å)
60	10	21	5.9	1.1(1)	0.45(4)	8.0(8)	8.0(8)	8.0(8)
40	7.5	29	5.0	1.3(1)	0.48(5)	8.3(8)	8.3(8)	8.3(8)
-40	14.8	66.4	8.3	0.63(4)	0.49(4)	4.4	10.1	36.0
-90	10.7	73.6	8.3	0.68(6)	0.51(8)	4.7	14.8	58.1
-140	17.2	65.3	9.3	0.65(2)	0.51(8)	4.4	13.2	65.3
-190	15.6	99.0	8.8	0.63(1)	0.50(4)	4.5	15.0	65.7

In the TABLES IV and V, the results show two domain lengths, L_1 and L_2 and their corresponding electron densities ρ_1 and ρ_2 . The corresponding XR fits and electron density profile is shown in Figure 56. The electron density profiles at interfacial potentials of 60 mV and 40 mV of Figure 56 are narrow-consistent with the width and amplitude of the 2D non-generic model. At the low potentials of 10 mV and below, there are two electron density profile peaks. A narrow peak corresponding to a 2D nanoparticle and an adjacent broad peak corresponding to a 3D structure. The symbol H in Tables IV and V represent the position of the peak centers from the electron density profiles in Figure 56.

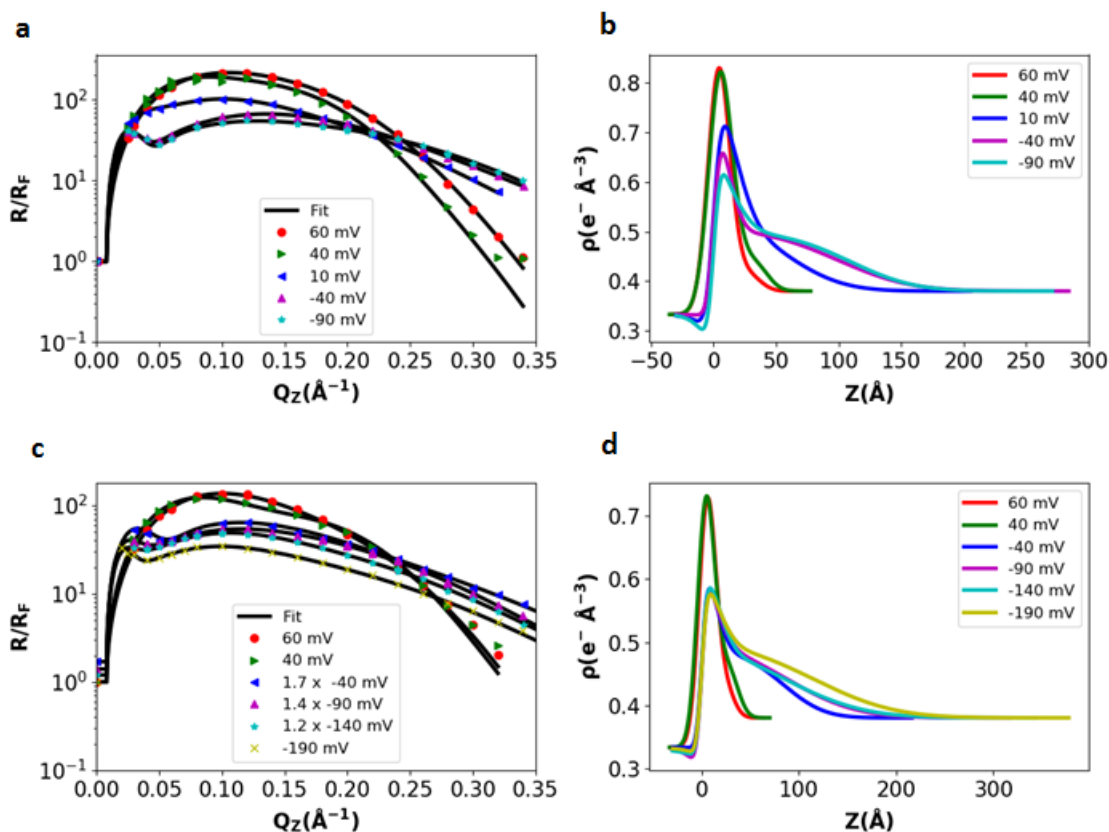


Figure 56. 3D slab model fit of a) 60 nM nanoparticle concentration in aqueous phase b) Corresponding electron density profile of the 60 nM nanoparticle concentration in aqueous phase. c) 35 nM nanoparticle concentration in aqueous phase d) Corresponding electron density profile of the 35 nM nanoparticle concentration in aqueous phase.

5.3.4 Proposed Structure of the 2D Spherical and 3D Slab Nanoparticle Models

GISAXS measurements showed the existence of 2D arrays of nanoparticles. Subsequent tuning of the interfacial potential led to the formation of a 3D structure. The 2D GISAXS data analysis at interfacial potentials of 60 mV and 40 mV is consistent with a 2D triangular lattice structure of a spherical nanoparticle. XR model analysis of the 2D HCP fitted well with the spherical gold nanoparticle.

The 3D formed from the interfacial potentials of 10 mV and below showed GISAXS scattering patterns not consistent with the scattering from the 2D triangular lattice of a spherical nanoparticle at interfacial potentials of 60 mV and 40 mV. Our X-ray model analysis also confirmed that the 3D cluster formed is non-spherical. In the model, a 3D spherical nanoparticle was assumed which could not fit the reflectivity data well at the high Q_z .

The nanoparticles initially at the positive interfacial potentials (60 mV and 40 mV) have counter-ions around them on the DCE side of the interface. When the interfacial potential was tuned to 10 mV and below, the counter-ions depleted leading to enhanced positive ions on the DCE side of the interface. The initial stability of the nanoparticles in the DCE was due to the electrostatic screening by the counter-ions on the DCE side of the interface. Since the counter-ions are partially depleted, the heavily charged nanoparticles in the DCE are no longer well screened and become unstable in the low permittivity medium of the DCE. For the nanoparticles to be stable in the DCE, they have to form clusters to maximize their screening with the fewer counter-ions as shown in the Figure 57.

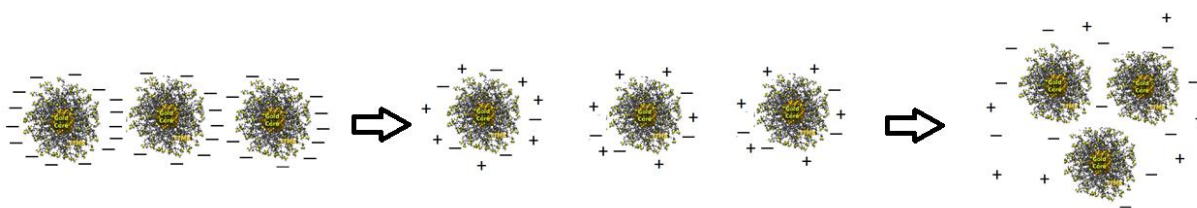


Figure 57. Coulombic interactions between charged nanoparticles and ions at the interface for the 2D structure transition to 3D structure.

Based on the above mechanism of counter-ion enhancement and depletion at different interfacial potential leading to 2D and 3D structures of the nanoparticles, the following cartoons in Figures 58 and 59 describe the equilibrium structures of the 2D and 3D structures respectively.

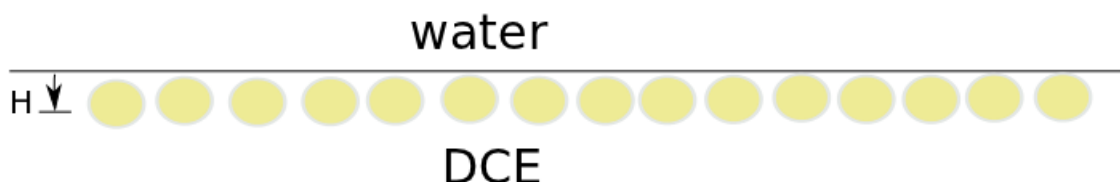


Figure 58. Proposed model (side view) of the 2D HCP formed due to counter-ion enhancement on the DCE side of the interface.

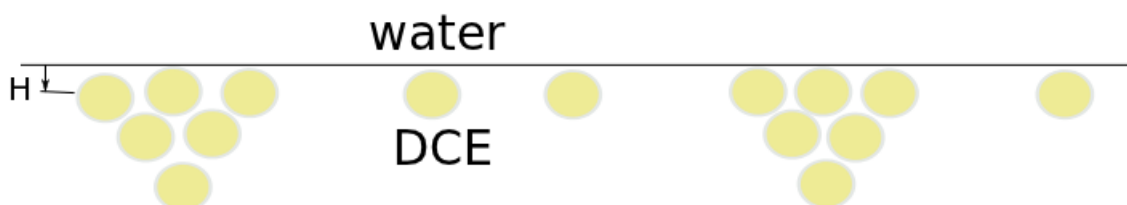


Figure 59. Proposed model (side view) of the 3D structure formed due to counter-ion depletion on the DCE side of the interface

The base of the 3D pyramid structure is hexagonal because of the initial 2D HCP formed. We expect that the 2D nanoparticles re-arrange to form the 3D structure without increased nanoparticle density or coverage at the interface because the electron density profiles of the Figure 56 whose electron density for the single nanoparticles decrease as the clusters are formed.

CHAPTER 6

CONCLUSION

We have demonstrated voltage-tunable 2D and 3D structures at a water/DCE interface. XR and GISAXS measurements showed the formation of 2D arrays of spherical nanoparticles at interfacial potentials of 40 mV and 60 mV for bulk water phase nanoparticle concentrations of 60 nM and 35 nM . On further decreasing the interfacial potential, a 3D cluster is formed at the water/DCE interface.

A model of XR that utilized a spherical nanoparticle showed that the nanoparticles adsorb on the DCE side of the interface when potentials of 60 mV and 40 mV were applied across the water/DCE interface. On further decreasing the potentials to 10 mV and below, a 3D structure was formed at the interface. Analysing the XR data under the assumption that the 3D structure was spherical did not provide a good fit, thereby suggesting that the 3D structure was not spherical.

A slab model was used to analyse the 2D and 3D structures. The electron density profiles of the 2D structures determined by the slab model were consistent with the peak widths and amplitudes determined by the spherical model. Overall, the slab model fitted well for the XR data while the spherical model fitted well with only the 2D data of the XR data. However, the spherical model is a better model for single nanoparticle structures since we can justifiably assume that the single nanoparticles are close to spherical. In that case, the spherical model describes the physical characteristics of the structures at the water/DCE interface, which include the inter-particle spacing, average position of the nanoparticles from the interface, immersion depth distribution of

the nanoparticles at the interface, and coverage of the nanoparticles at the interface. Both the slab and spherical models provide accurate electron density profiles of the structures at the interface. The slab model proved to be more convenient for a first analysis of 3D nanoparticle clusters since we did not know beforehand the shape of the cluster.

Varying the electrochemical potential at the interface produced significant changes in the position, coverage and immersion depth distribution of nanoparticles for both concentrations. For example, decreasing the interfacial potential from 60 mV to 40 mV moved nanoparticles that were initially at 26 Å on the DCE side of the interface to ~15 Å, according to the XR analysis. A decrease in interfacial potential was accompanied by increased interfacial coverage from ~ 90% to 100% for the 60 nM nanoparticle concentration in the bulk phase and ~80% to ~90% for the 35 nM nanoparticle concentration in the bulk phase. GISAXS analysis also showed that decreasing the interfacial potential from 60 mV to 40 mV led to a decrease in nearest neighbour distance of the nanoparticles. Hence, as the nanoparticle nearest neighbour distance decreased, nanoparticle coverage increased for both bulk nanoparticle concentrations.

Overall, increased bulk phase nanoparticle concentration increased nanoparticle coverage and reduced nearest neighbour distance but did not change the position and distribution of the immersion depth of the nanoparticles at the interface. Decreasing the interfacial potential from 60 mV to 40 mV increased nanoparticle coverage, decreased nanoparticle position, increased immersion depth distribution, and decreased nearest neighbour distance between the nanoparticles at the interface. From the analysis, it is clear that reducing the interfacial potential changes the interfacial structure, especially from a 2D structure to a 3D structure.

The observed increase in nanoparticle coverage at the interface as a function of decreased interfacial potentials from 60 mV and 40 mV is not consistent with our previous study of voltage tunable arrays of gold nanoparticles at water/1,2-dichloroethane interface using 5 mM NaCl and 5 mM BTTPATPFB in DCE. What is different in our previous study and this study are the NaCl salt concentration in the aqueous phase of which the current concentration is 10 times the previous NaCl concentration used and the nanoparticle concentration in the bulk phase was ~ 10 nM. Other variables such as stirring speed and equilibration times were significantly different. We do not expect the concentration of the nanoparticles in the bulk phase or the NaCl electrolyte to be the reason why previous and current results of interfacial coverage changed as a function of interfacial potential differ. Neither do we expect relaxation times to be the reason since in both cases, X-ray measurements continued until a stable data was obtained.

Another difference between the previous study and the current study is the 3D cluster formation which was not observed in the previous study for the same potentials. Typical relaxation times for the initial equilibration potential (60 mV) may take ~ 7 hours of continuous stirring and subsequent tuning (interfacial potential of 40 mV) takes ~ 1 hour or less. However, at an interfacial potential of ~ 10 mV, relaxation time is over 15 hours. Further tuning of the interfacial to -40 mV has a typical relaxation time of ~ 6 hours. From interfacial potential of -90 mV and below, typical relaxation time is $\sim 1-2$ hours for X-ray measurements. We did not observe such long relaxation times in our previous study or the formation of the supposed 3D pyramidal structure at similar interfacial potentials. In Argonne National Laboratory, our typical initial equilibration times is ~ 18 hours at an interfacial potential of 60 mV-even though ~ 6 hours is enough to achieve an equilibrium structure for XR measurements- including optical alignment and X-ray beam optimisation. We believe the long relaxation times at 10 mV and below is the

reason for the formation of the 3D structure which was not observed at similar interfacial potentials in previous study. Thus, the initial 2D structure from which the 3D structure was formed was in a metastable state.

The assembly of nanoparticles at an oil/water is an emerging technology which has practical applications and scientific interests. In this study, our results have shown that by changing the interfacial potential across the water and DCE phase, it is possible to obtain 2D array and on further interfacial potential tuning towards the negative potentials, 3D structure is formed.

This study has shown a proof of concept of voltage-tunable 2D and 3D structures and the effect bulk conditions can have on interfacial structures of the nanoparticles. Understanding the role of the bulk conditions and interfacial potentials can provide useful insight into making 2D and 3D films at a water/oil interface.

Chapter 7

CHALLENGES AND FUTURE WORK

We have demonstrated a voltage tunable 2D and 3D structures by tuning the interfacial potentials. The increase in NaCl concentration –with respect to our previous study- was expected to change the Debye length (screening length) and subsequently make the nanoparticles preferentially adsorb and stabilize on the water side of the interface.

In our analysis, we used several X-ray models to analyze and characterize the structure of the nanoparticles at the interface. Our proposed spherical 2D nanoparticle model was able to fit the XR data from which we managed to extract important physical parameters of the nanoparticles such as nearest neighbor separation distance, nanoparticle position, nanoparticle distribution depths and coverages. Our 3D spherical nanoparticle models were not either able to fit the 3D data or provide meaningful physical properties.

Our slab model was able to fit the 3D data and provide useful information like the electron density profile. However, we lost important information such as the particle's shape, size, position and coverage which characterize the structure of the nanoparticles at the interface.

Overall, this study was a success because we achieved a voltage tunable 2D and 3D structures. The counter-ions through coulombic interactions with the nanoparticles at the interface were the driving force in tuning the 2D to 3D structure. We hope that future work can be done more on the role of ion concentrations on the structure of the nanoparticles at the interface. Using divalent or trivalent ions in the aqueous phase could be interesting since they can provide different strength

of coulombic interactions and screening on the heavily charged nanoparticles and therefore provide a different kind of ordering, position and structure at the interface.

MD simulation study will also be useful in understanding the mechanism of the interactions between the ions and the nanoparticles leading to the formation of the 3D structure. This will help elucidate the dynamics and kinetic of the transition of the nanoparticles' structure from 2D to 3D and enable us to explore other electrochemically induced structures. That is, to what extent can we tune the interface to achieve different 3D shapes, sizes, aspect ratio and so on?

The role of solvent presents a compelling case. For example, replacing the DCE with nitrobenzene or Toluene whose dielectric constants are ~ 35 and ~ 30 respectively can decrease the electrostatic correlation between the counter-ions on the DCE side of the interface and the nanoparticles initially present in the bulk phase of the water. This may cause the nanoparticles to order on the water side of the interface instead of the oil if the electrostatic correlation is tuned with solvent. Bringing the nanoparticles to the water side of the interface will provide a different structure. The relative dielectric values of water and DCE are ~ 80 and ~ 10 respectively meaning that the electrostatic correlation between the nanoparticles and the ions in the DCE is ~ 8 times stronger than the electrostatic correlation between the nanoparticles and the ions in the water. Using nitrobenzene instead of DCE will reduce the effect of electrostatic correlation between the ions and the nanoparticles in the oil side by a factor of ~ 2.3 and instead, improve the likelihood of the nanoparticles ordering on the water side of the interface.

We are not sure of the role of ionic size on the structure of the nanoparticles at the interface. For example, to what extent will the ordering change if the monovalent BTPPATPFB salt is replaced with a monovalent salt of tetrabutylammonium tetraphenylborate (TBATPB)? Literature study has demonstrated that ionic radius related to ionic charge density plays important role in ion

hydration energy which can influence ion condensation and screening on the heavily charged nanoparticles. For the same monovalent ions but different ionic radii, it will be interesting to see how the charge density affects the ion condensation on the surface of the nanoparticles and the structure of the nanoparticles.

The role of the ligands could also be interesting. The ligand used in this study has a TMA terminal, which does not depend on pH. Hence, whether in the DCE or water phase, there are still ~100 electronic charges from the ~ 100 ligands distributed over the surface of the 2 nm gold nanoparticle. Literature study has shown that some ligands with functional groups, for example, -COOH terminal demonstrate different surface charges in different pH media. Hence it will be expected that the surface charge density of the nanoparticles with a -COOH terminal will have higher surface charge density in the water phase than in the DCE phase. In addition, the pH of the water phase could be adjusted to modulate the surface charge density of the nanoparticles in the water phase. Therefore, pH adjustment together with pH sensitive ligand will play a significant role in the structure and density of the nanoparticles at the interface.

Future study and model analysis could address the functional form of the average electron density needed to fit the supposed 3D pyramid to validate our claim of pyramidal structure and provide real space information such as depth, distribution and orientation of the nanoparticles if any. Understanding why the nanoparticles will form a 3D pyramid is still not clear even though forming a spherical 3D structure may require more counter-ions, which are not available at the interfacial potentials at which the 3D structure was formed. It will be interesting to know the extent to which the interfacial ions can be tuned to obtain different 3D structures and aspect ratios.

Understanding the surface chemistry of the nanoparticles, their interactions and their environments are key in the developments of 2D and 3D films for functional devices

APPENDICES

APPENDIX A

INTERFACIAL TENSION MEASUREMENT AND ROUGHNESS.

Sample: Without Nanoparticles (w/o NP)

$\Delta\phi^{w-0}$ (mV)	Interfacial tension, γ (mN/m)
410	17.3 \pm 0.1
360	19.9 \pm 0.1
310	22.3 \pm 0.1
260	24.3 \pm 0.1
210	25.7 \pm 0.1
160	26.5 \pm 0.1
110	27.1 \pm 0.1
60	27.6 \pm 0.1
10	27.7 \pm 0.1
-40	27.8 \pm 0.1
-90	27.7 \pm 0.1
-140	27.4 \pm 0.1
-190	26.4 \pm 0.1

Sample: With Nanoparticles (w/ NP). 35 nM Nanoparticle in bulk aqueous phase

$\Delta\phi^{w-0}$ (mV)	γ (mN/m)	σ (Å)
60	20.8 \pm 0.3	4.1
40	18.6 \pm 0.1	4.3
10	16.1 \pm 0.1	4.6
-40	14.6 \pm 0.2	4.9
-90	4.3 \pm 0.1	4.9
-140	14.5 \pm 0.1	4.9
-190	16.5 \pm 0.2	4.6

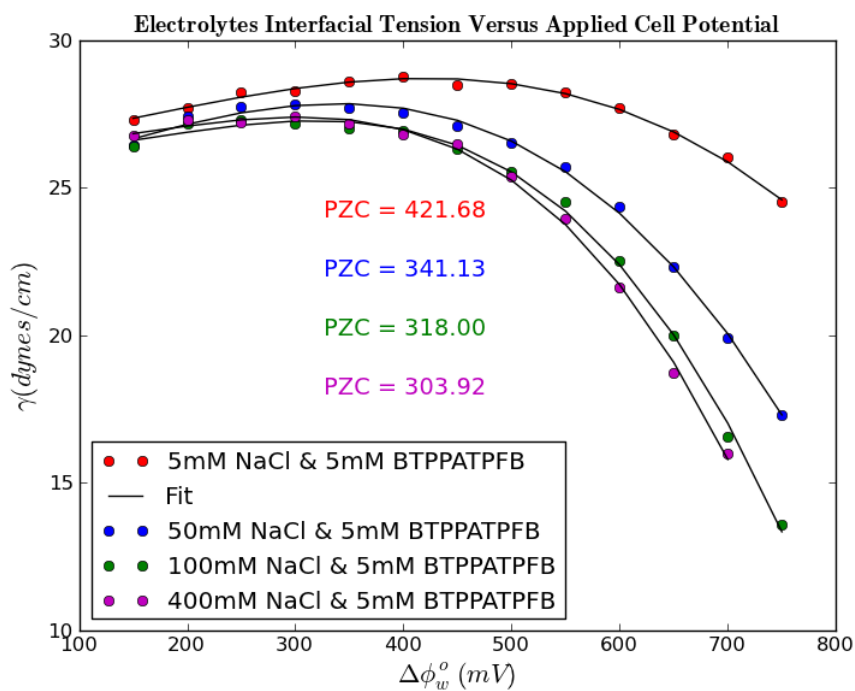
APPENDIX A (Continued)**INTERFACIAL TENSION MEASUREMENT AND ROUGHNESS.****Sample: With Nanoparticles (w/ NP). 60 nM Nanoparticle in bulk aqueous phase.**

(mV)	γ (mN/m)	σ (Å)
60	19.1 \pm 0.1	4.25
40	16.2 \pm 0.1	4.62
10	14.1 \pm 0.1	4.95
-40	12.7 \pm 0.1	5.22
-90	12.2 \pm 0.1	5.32
-140	12.6 \pm 0.1	5.24
-190	14.4 \pm 0.1	4.90

APPENDIX A (Continued)

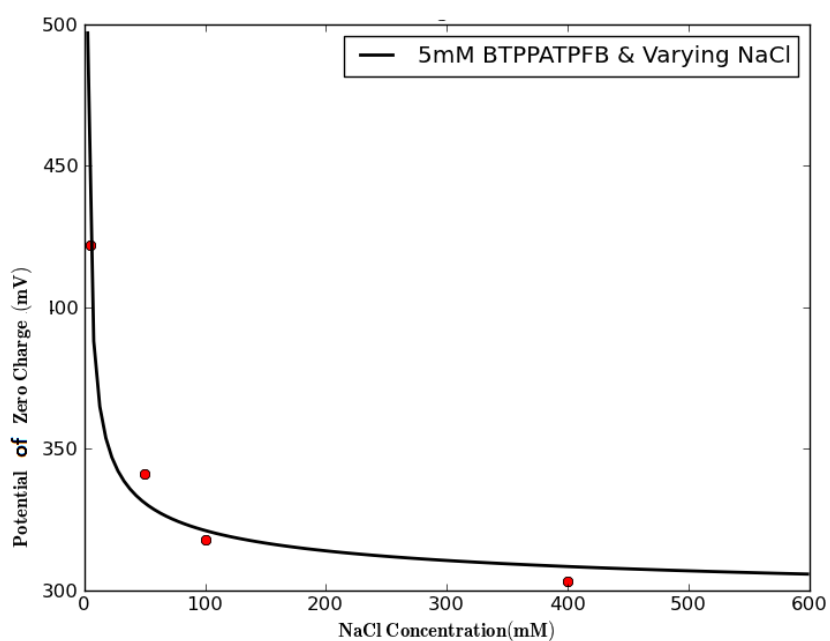
X NaCl Concentration and 5 mM BTPPATPFB in DCE. X= 5, 50, 100 and 400 mM NaCl

How potential of zero charge (PZC) was extracted from the interfacial tension versus applied cell's potential ($\Delta\phi_w^0$). We measured interfacial tension as a function of external potential of the sample cell for different concentrations of electrolytes. Then fitted the tension to a polynomial. The apex of the interfacial tension curve's corresponding interfacial is the PZC.



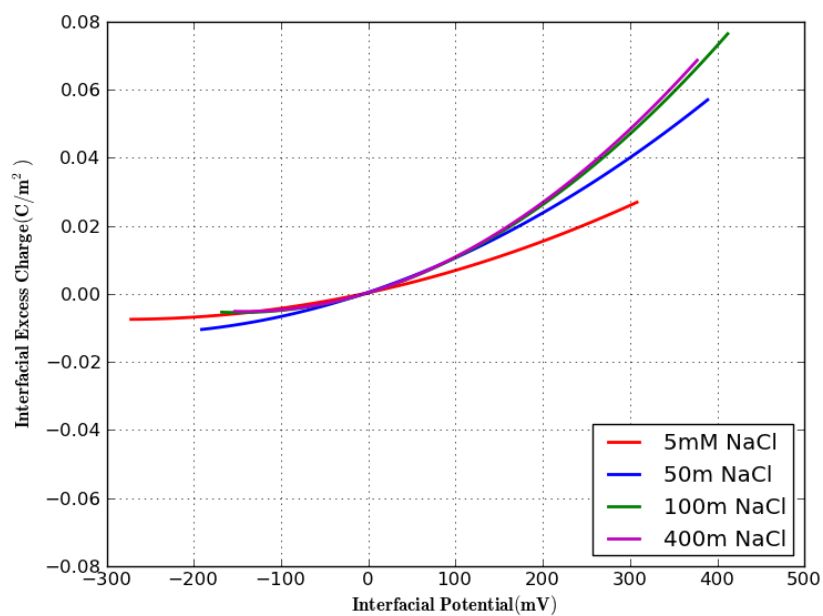
APPENDIX A (Continued)**X NaCl Concentration and 5 mM BTPPATPFB in DCE. X= 5, 50, 100 and 400 mM NaCl**

Potential of Zero Charge as a function of NaCl concentration. The concentration of the BTPPATPFB in DCE was fixed for all the NaCl concentrations. The PZC charge was obtained from the fits of the apex of the interfacial tension curves for the different electrolyte concentrations.



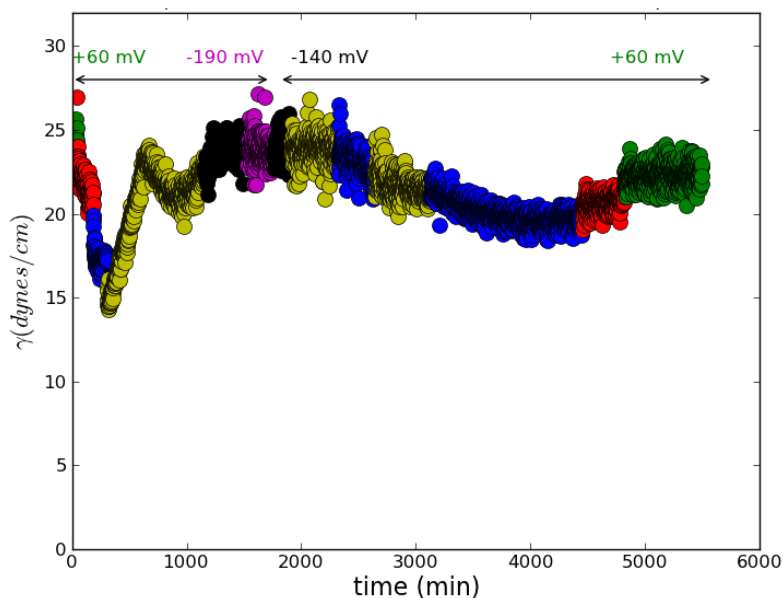
APPENDIX A (Continued)**X NaCl Concentration and 5 mM BTPPATPFB in DCE. X= 5, 50, 100 and 400 mM NaCl**

We calculated the interfacial surface charge of the electrolyte ions from the fits and interpolation of the slope of the interfacial tension fits for different aqueous NaCl concentrations with fixed 5mM BTPPATPFB in DCE.



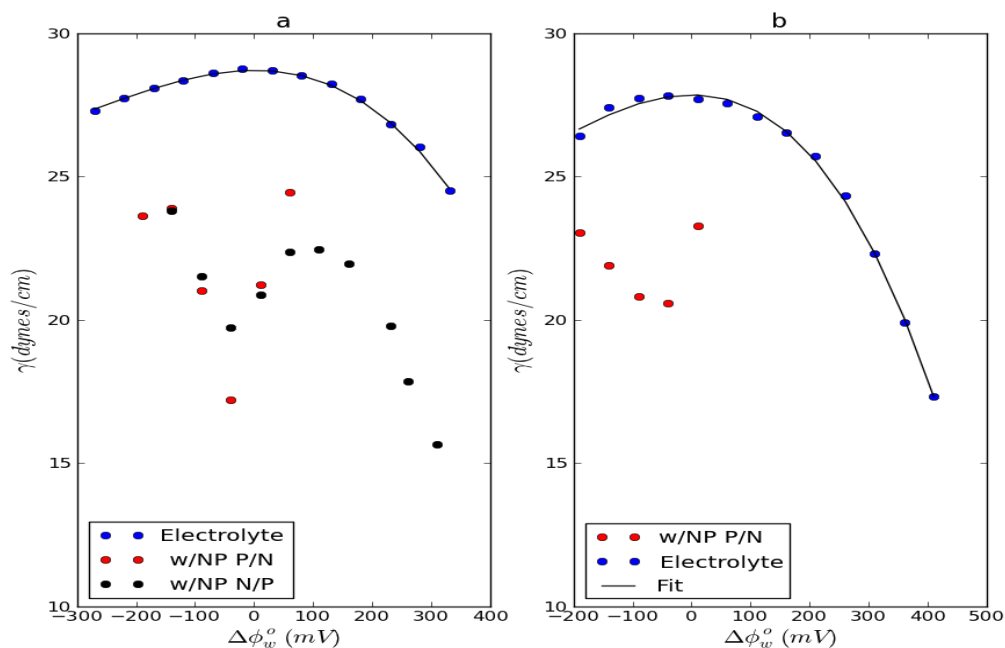
APPENDIX A (Continued)

SOME PRELIMINARY INTERFACIAL TENSION MEASUREMENTS

5 mM NaCl Concentration and 5 mM BTPPATPFB in DCE with 10 nM Nanoparticle Concentration

We considered 5 mM NaCl aqueous concentration and 5 mM BTPPATPFB in DCE with 10 nM nanoparticle bulk concentration in the water phase. Sample was initially equilibrated at 60 mV interfacial potential, moved towards the negative interfacial potentials in a step of -50 mV up to an interfacial potential of -190 mV. Then sample moved towards the positive interfacial in a step of 50 mV back to interfacial potential of 60 mV.

APPENDIX A (Continued)



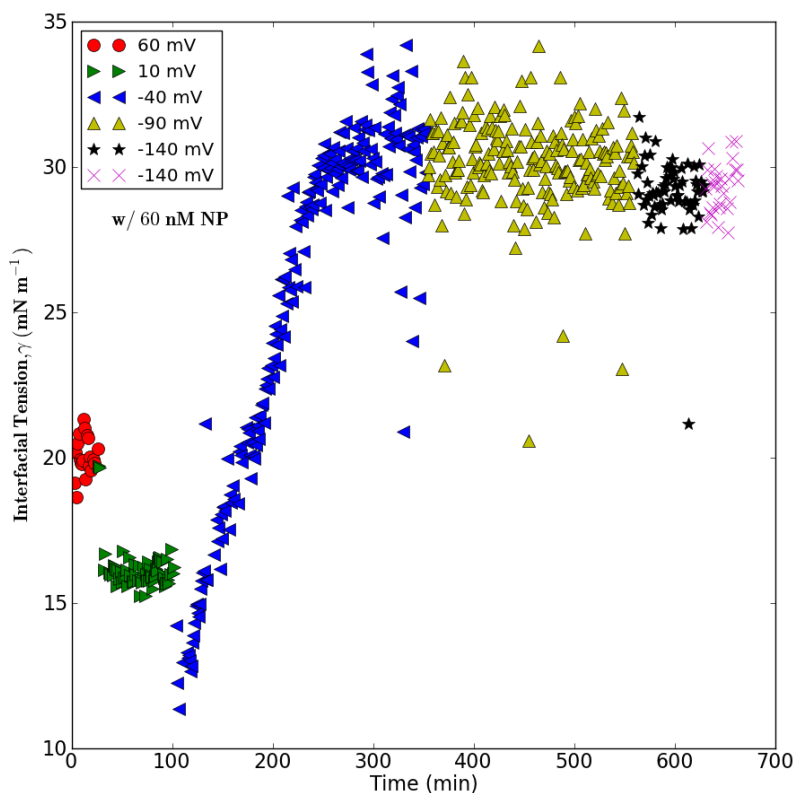
a: is a 5 mM NaCl concentration and 5 mM BTTPATPFB in DCE Electrolytes with 10 nM Nanoparticle Concentration in aqueous phase initially equilibrated at 60 mV interfacial potential and moved towards the negative interfacial potentials in a step of -50 mV to a final interfacial potential of -190 mV. Then moved back towards the positive interfacial in a step of 50 mV to interfacial potential of 300 mV P/N means from positive to negative interfacial potential and N/P means from negative to positive interfacial potentials. We begin with P/N and then move from N/P.

b: is a 50 mM NaCl concentration and 5 mM BTTPATPFB in DCE electrolytes with 10 nM nanoparticle bulk concentration initially equilibrated at 10 mV interfacial potential and moved towards the negative interfacial potentials in a step of -50 mV.

Stirrer speed used is ~ 130 rpm in the equilibration for all interfacial potentials.

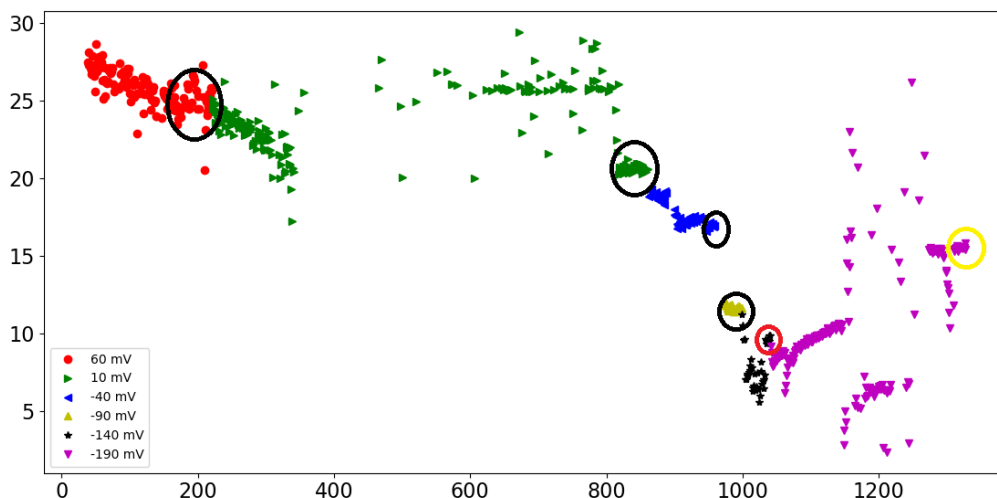
APPENDIX A (Continued)**50 mM NaCl and 5 mM BTTPATPFB in DCE with 60 nM Nanoparticle Concentration.**

This measurement was abandoned but it was consistent with some of the observed interfacial tension measurements at certain potentials (for example, at -40 mV here) taking a long time to relax. The interfacial relaxation time can be oscillatory. That is tension continuous to go up for some time and down for a while and then ends at a final value during relaxation. The dynamics of the initial equilibration potential times (60 mV) were not recorded here. Only the final equilibration tension were recorded briefly. Experimental condition was with 50 mM NaCl concentration and 5 mM BTTPATPFB in DCE electrolytes with 60 nM nanoparticle bulk concentration in aqueous phase. System was initially equilibrated at 60 mV interfacial potential and moved towards the negative interfacial potentials.



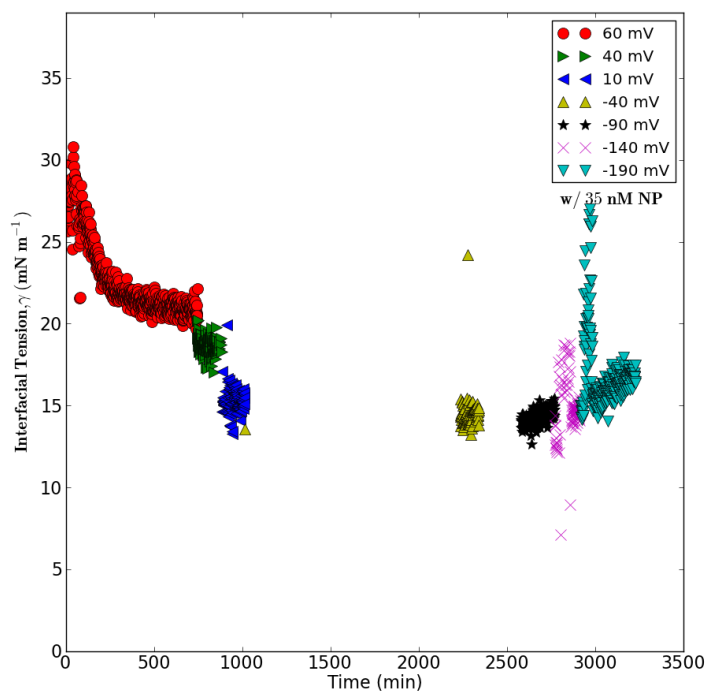
APPENDIX A (Continued)**5 mM NaCl and 5 mM BTTPATPFB in DCE with 10 nM Nanoparticle Concentration.**

This measurement was done with 5 mM aqueous NaCl concentration and 5 mM BTTPATPFB in DCE electrolytes with 10 nM nanoparticle bulk concentration in aqueous phase. The idea was to test the effect of stirring and waiting time on the equilibrium tension values. The values in the circles are the final tension values recorded. The fluctuations in the some of the tension values at certain potentials is due to the stirrer close to the interface disturbing the interface and affecting the tension values. The final values in circles are values measured when stirring was continues. In addition, at certain potentials, for example, -40 mV and -90 mV, there was no stirring. Potentials 10 mV and -190 mV were stirred for very long time compared with potential -140 mV.



APPENDIX A (Continued)**50 mM NaCl Concentration and 5 mM BTPPATPFB in DCE Electrolytes with 35 nM Nanoparticle Bulk Concentration**

This measurement was done with 50 mM aqueous NaCl concentration and 5 mM BTPPATPFB in DCE electrolytes with 35 nM nanoparticle bulk concentration in aqueous phase. Stirring was immediately started when the interfacial potential was at -40 mV without waiting because I observed changing the interfacial tension, waiting for a while can lower the interfacial tension and subsequent stirring and waiting can bring the interfacial tension up with time. The initial highly dispersed values of interfacial tension at -190 mV was due to stirring which perturbed the interface. Stirring speed was later slowed and interface was no more disturbed.



Missing part of the measurements at interfacial potentials was due to stirring at that time, the tension values being recorded was due to interfacial disturbance of the stirrer.

APPENDIX B

FIT PARAMETERS OF GISAXS ANALYSIS USING LORENTZIAN FUNCTION

A is area of the peak, subscripts

w is width of peak, Q is the parallel wave vector showing center of peak from fit

0, 1, 2 and 3 are first, second, third and fourth order peaks

IN-PLANE FIT WITH 60 nM NANOPARTICLE CONCENTRATION IN BULK

AQUEOUS PHASE.

$\phi^{w=0}$ (mV)	$A_0 \times 10^{-2}$ (\AA^{-2})	$A_1 \times 10^{-2}$ (\AA^{-2})	$A_2 \times 10^{-3}$ (\AA^{-2})	$A_3 \times 10^{-3}$ (\AA^{-2})	$Q_0 \times 10^{-1}$ (\AA^{-1})	$Q_1 \times 10^{-1}$ (\AA^{-1})	$Q_2 \times 10^{-1}$ (\AA^{-1})	$Q_3 \times 10^{-1}$ (\AA^{-1})	$w_0 \times 10^{-2}$ (\AA^{-1})	$w_1 \times 10^{-2}$ (\AA^{-1})	$w_2 \times 10^{-2}$ (\AA^{-1})	$w_3 \times 10^{-2}$ (\AA^{-1})
60		1.066	3.760	1.502		1.072	1.857	2.150		0.864	1.962	1.888
40	1.034	1.246	4.132	0.961	0.323	1.085	1.882	2.180	3.923	1.173	2.723	2.074
10	1.021				0.323				4.115			
-40	1.122				0.332				3.824			

APPENDIX B (Continued)

FIT PARAMETERS OF GISAXS ANALYSIS USING LORENTZIAN FUNCTION

A is area of the peak, subscripts

w is width of peak, Q is the parallel wave vector showing centre of peak

0, 1, 2 and 3 are first, second, third and fourth order peaks

**IN-PLANE FIT WITH 35 nM NANOPARTICLE CONCENTRATION IN BULK
AQUEOUS PHASE**

: RIGHT PEAK

ϕ^{w-o} (mV)	$A_0 \times 10^{-4}$ (\AA^{-2})	$A_1 \times 10^{-4}$ (\AA^{-2})	$A_2 \times 10^{-4}$ (\AA^{-2})	$Q_0 \times 10^{-1}$, (\AA^{-1})	$Q_1 \times 10^{-1}$, (\AA^{-1})	$Q_2 \times 10^{-1}$, (\AA^{-1})	$w_0 \times 10^{-2}$, (\AA^{-1})	$w_1 \times 10^{-2}$, (\AA^{-1})	$w_2 \times 10^{-2}$, (\AA^{-1})
60	8.077	2.250	2.184	1.005	1.743	1.998	0.8287	1.701	2.279
40	6.924	3.522	3.0889	1.030	1.7912	2.042	0.8915	2.537	2.64

APPENDIX B (Continued)

IN-PLANE FIT WITH 35 nM NANOPARTICLE CONCENTRATION IN BULK

AQUEOUS PHASE: LEFT PEAK

ϕ^{w-o} (mV)	$A_0 \times 10^{-4}$ (\AA^{-2})	$A_1 \times 10^{-4}$ (\AA^{-2})	$A_2 \times 10^{-4}$ (\AA^{-2})	$Q_0 \times 10^{-1}$ (\AA^{-1})	$Q_1 \times 10^{-1}$, (\AA^{-1})	$Q_2 \times 10^{-1}$, (\AA^{-1})	$w_0 \times 10^{-2}$, (\AA^{-1})	$w_1 \times 10^{-2}$, (\AA^{-1})	$w_2 \times 10^{-2}$, (\AA^{-1})
60	8.361	2.287	1.921	-1.005	-1.743	-2.014	0.873	1.830	2.472
40	7.515	5.840	3.089	-1.038	-1.806	-2.076	1.0301	3.785	2.1978

APPENDIX C

FIT PARAMETERS OF GISAXS ANALYSES USING LORENTZIAN AND LINEAR FUNCTIONS TO FIND THE PEAK CENTERS OF THE 3D STRUCTURE

Interfacial Potential of 10 mV with 60 nM Nanoparticle Concentration in Bulk Aqueous

Phase.

Center, Q_z , (\AA^{-1})	Fit Area, A (\AA^{-2})	Fit Center, Q_{xy} (\AA^{-1})	Fit Width, w_o (\AA^{-1})
0.02	0.0251	0.0125	0.00194
0.03	0.0224	0.0176	0.0089
0.04	0.014	0.0243	0.0626
0.05	0.0101	0.02168	0.02483
0.06	0.00301	0.029835	0.02472
0.07	0.001652	0.03633	0.02696
0.08	0.0009788	0.0432	0.028801
0.09	0.0006	0.04993	0.03096
0.1	0.000175	0.0616	0.0195645

Interfacial Potential of +10 mV with 60 nM Nanoparticle Concentration in Bulk Aqueous

Phase.

Center, Q_{xy} , (\AA^{-1})	Fit Area ,A (\AA^{-2})	Fit Center, Q_z (\AA^{-1})	Fit Width, w_o (\AA^{-1})
0.02	0.07979	0.01559	0.01970
0.03	0.01065	0.03233	0.030808
0.04	0.00581	0.04493	0.04474
0.05	0.00235	0.06128	0.0430
0.06	0.00123	0.0730	0.043278
0.07	0.00041	0.0893	0.03705
0.08	0.000336	0.102108	0.03602

APPENDIX C (Continued)

FIT PARAMETERS OF GISAXS ANALYSIS USING LORENTZIAN FUNCTION

Interfacial Potential of -40 mV with 60 nM Nanoparticle Concentration in Bulk Aqueous

Phase.

Center, Q_z (\AA^{-1})	Fit Area, A (\AA^{-2})	Fit Center, Q_{xy} , (\AA^{-1})	Fit Width, w_o (\AA^{-1})
0.05	0.00897993	0.0231328	0.02202
0.06	0.00412901	0.028029	0.0236482
0.07	0.00183	0.0341766	0.0277524
0.08	0.0006759	0.042182	0.027065
0.09	0.00041455	0.05033	0.0269464

Interfacial Potential of -40 mV with 60 nM Nanoparticle Concentration in Bulk Aqueous

phase.

Center, Q_{xy} , (\AA^{-1})	Fit Area ,A (\AA^{-2})	Fit Center, Q_z (\AA^{-1})	Fit Width, w_o (\AA^{-1})
0.02	0.077969	0.02365	0.0140
0.03	0.05734367	0.023196	0.0274
0.04	0.0281977	0.0230	0.0454
0.05	0.0015937	0.01796	0.00999
0.06	0.0015732	0.0271	0.02460
0.07	0.000116	0.0276	0.00730
0.08	0.000416	0.030	0.0294
0.09	0.000034	0.027	0.0040
0.1	0.00005	0.034	0.0195

APPENDIX D**X-RAY XR FITTING FUNCTIONS USED IN ANALYSIS 2D SPHERICAL NANOPARTICLE MODEL**

means comment in the program. Not to be executed

```
import sys
```

```
import os
```

```
sys.path.append('/home/daniel/Documents/XR-Analysis/Fortran_Routines/')
```

```
import pylab as pl
```

```
import numpy as np
```

```
from xr_ref import Parratt# calling xr_ref and using Parratt from its many functions
```

```
os.getcwd()# get working directory
```

```
global lam# making the wavelength lam accessible to all parts of the program
```

```
lam=0.41328
```

```
sys.path.append('/home/daniel/Documents/lmfit/lmfit-0.7.2/build/lib.linux-x86_64-2.7/lmfit/')#
```

```
access to data path
```

```
from lmfit import minimize, Parameters, conf_interval# need to have lmfit installed
```

```
from lmfit.printfuncs import *
```

```
from scipy.optimize import curve_fit
```

```
from scipy.optimize import optimize # Need to install scipy
```

APPENDIX D (Continued)

```

def Rf(q):#Fresnel Reflectivity from water/DCE system

    r1,r2=parratt(q,0.41328,[0.0,10.0],[0.334,0.38],[0.0,0.0])# wave vector, wavelength, number of
internal layers, electron densities and absorption coefficient

    return r1 # r1 is the reflectivity, r2 is the amplitude of reflectivity

#####

def ref_residual(par,x,y,yerr):# par has the physical properties of the nanoparticles at the interface

    Rc=par['Rc'].value# size of nanoparticle

    Z0=par['Z0'].value # position of nanoparticle

    D=par['D'].value # lattice spacing of nanoparticle

    cov=par['cov'].value# coverage of nanoparticle

    xi=par['xi'].value # distribution of immersion depth

    rhoc=par['rhoc'].value # electron density of gold nanoparticle

    sig=par['sig'].value# roughness at the interface

    rhos=[0.334,0.38] # electron density of water and DCE

    lam=0.41328# wavelength

```

APPENDIX D (Continued)

```

if Z0<0:

    z=arange(-100.0,50.0)# range of depth to calculate reflectivity

else:

    z=arange(-50,100.0)

d=ones_like(z)# size of the internal layers

edp=decayNp(z,Rc=Rc,z0=Z0,xi=xi,cov=cov,rhos=rhos,rhoc=rhoc,sig=sig,D=D)#    electron
density function

beta=np.zeros_like(z) # absorption of the solvent when X-ray passes through it

rho=np.array(edp,dtype='float') # arrays of electron density

refq,r2=parratt(x,lam,d,rho,beta)# reflectivity calculated using Parratt function

rf,r2=parratt(x,lam,[0.0,1e3],rhos,[0.0,0.0])# wave vector, wavelength, number of internal
layers, electron densities and absorption coefficient

if yerr==None: # error bars on reflectivity data

    return refq/rf-y/rf

else:

    return (refq-y)/yerr

#####

def ref_fun(par,x):# calculates reflectivity

    Rc=par['Rc'].value

    D=par['D'].value

```

APPENDIX D (Continued)

```

Z0=par['Z0'].value
cov=par['cov'].value
rhoc=par['rhoc'].value
xi=par['xi'].value
sig=par['sig'].value
rhos=[0.334,0.38]
lam=0.41328
if Z0<0:
    z=arange(-100.0,50.0)
else:
    z=arange(-50,100.0)
d=ones_like(z)
edp=decayNp(z,Rc=Rc,z0=Z0,xi=xi,cov=cov,rhos=rhos,rhoc=rhoc,sig=sig,D=D)
beta=np.zeros_like(z)
rho=np.array(edp,dtype='float')
refq,r2=parratt(x,lam,d,rho,beta)
rf,r2=parratt(x,lam,[0.0,1e3],rhos,[0.0,0.0])
return refq/rf # returns calculated reflectivity normalized by Fresnel reflectivity
#####
def decayNp(z,Rc=10,D=30.0,z0=0.0,xi=1.0,cov=100.0,rhoc=4.65,rhos=[0.334,0.38],sig=1.0):#
calculates the electron density
    z2=arange(z[0]-4*int(sig),z[-1]+4*int(sig)+1)

```

APPENDIX D (Continued)

```

intf=where(z2<=0,rhos[0],rhos[1])

if z0<=0:

    z1=arange(-4*xi+z0,z0)# range of nanoparticles positions distributed in space, z

    dec=exp((z1-z0)/xi)/xi# immersion distribution function

else:

    z1=arange(z0,z0+4*xi)

    dec=exp((z0-z1)/xi)/xi

rhoz=zeros_like(z2)# electron density of the nanoparticle

for i in range(len(z1)):

    rhoz=rhoz+rhoNPz(z2,z0=z1[i],rhoc=rhoc,Rc=Rc,D=D,rhos=rhos)*dec[i]/sum(dec)

# function which integrates the electron density of the nanoparticle

rhoz=cov*rhoz/100.0+(100-cov)*intf/100.0 # average electron density consisting of water and
nanoparticles. intf = electron density of solvent either water or DCE

rough=exp(-arange(-4*int(sig),4*int(sig)+1)**2/2.0/sig**2)/sqrt(2*pi)/sig# roughness as a
Gaussian function

return convolve(rhoz,rough,mode='valid') # convolutes electron density with roughness

#####

def rhoNPz(z,z0=0,rhoc=4.65,Rc=10.0,D=28.0,rhos=[0.334,0.38]):# electron density of the gold
nanoparticle

    rhob=where(z>0,rhos[1],rhos[0])

    return

    where(abs(z-z0)<=Rc,(2*pi*(rhoc-rhob)*(Rc**2-(z-
z0)**2)+1.732*rhob*D**2)/(1.732*D**2),rhob)

```

APPENDIX D (Continued)

```
#####

def
ref_err(ddir='/',fname='sample2_ref_0.60v',err='neq',parname=['D','Rc','Z0','cov','rhoc','sig','xi'],p
aram=[56,10.0,20,20,3.65,3.5,2.23],\
fit=[False,False,True,True,True,False,False],plt=0,tit="):
#  fname='sample_50mM_400mV_ref.txt'
#  parname=['D','Rc','Z0','cov','sigma','xi']
#fit=[False,True,True,True,False,True]
#  rcParams['font.size']=20
#  rc('text', usetex=True)

lam=0.41328

rhos=[0.334,0.38]#

data1=loadtxt(ddir+fname)# uploads reflectivity data

data=zeros_like(data1)# creates a size of the size of the X-ray data

data[:,1]=data1[data1[:,0].argsort(),1]# sorts the second column in increasing order

data[:,0]=data1[data1[:,0].argsort(),0]# sorts the first column in increasing order

data[:,2]=data1[data1[:,0].argsort(),2]# sorts the third column in increasing order
```

APPENDIX D (Continued)

```

rf=Rf(data[:,0])# inputs the first column(wave vector) into the Rf function.

if err=='eq':# satisfies a condition

    data[:,2]=np.array([max(data1[i,2],data1[i,1]*0.01) for i in range(len(data1[:,2]))])#
increases data1b y 1%

elif err==None:

    data[:,2]=None

else:

    pass

par=Parameters()# fitting parameters.Sets the parameter names and space for the fitting
functions

par.add(parname[0], value=param[0], min=0.0, max=300.0, vary=fit[0])#D
par.add(parname[1], value=param[1], min=10, max=300.0, vary=fit[1])#Rc
par.add(parname[2], value=param[2], min=-100.0, max=100.0, vary=fit[2])#ZO
par.add(parname[3], value=param[3], min=0.0, max=100.0, vary=fit[3])#cov
par.add(parname[4], value=param[4], min=0.332, max=5.65, vary=fit[4])#rhoc
par.add(parname[5], value=param[5], min=0.00, max=7, vary=fit[5])#sig

par.add(parname[6], value=param[6], min=0.1, max=40, vary=fit[6])#xi

minobj=minimize(ref_residual,par,args=(data[:,0],data[:,1],data[:,2]))# objective function

minobj.leastsq()# minimize the objective function using least square aka leastsq

chisq=sum(ref_residual(par,data[:,0],data[:,1],data[:,2])**2)# calculates chisquared

```

APPENDIX D (Continued)

if plt==1:# plotting. If the call function has plt=1, program is executed otherwise no.

```
figure(figsize=(12,4))
```

```
subplot(131)
```

```
yscale('log')# putting it on logscale
```

```
errorbar(data[:,0],data[:,1]/rf,data[:,2]/rf,fmt='ro')#plotting data
```

```
x=linspace(0.002,1.2*data[-1,0],100)# range in which the fitted data is to be plotted
```

```
y=ref_fun(par,x)# returns the calculated reflectivity from the optimized parameters, par and
```

x, the range of interest

```
plot(x,y,'b-',lw=2)
```

```
xlabel(r'$\mathbf{Q_z} (\AA^{-1})$')
```

```
ylabel(r'$\mathbf{R/R_f}$')
```

```
xticks([0.0,0.15,0.3,0.45],fontsize=16)
```

```
yticks([5e-1,1,10,300],fontsize = 16)
```

```
ylim(0.8,300)
```

```
xlim(0,0.35)
```

```
title(r'+tit+' $\chi^2$=% .2f%chisq,fontsize=16)# titles
```

```
grid()
```

```
subplot(132)
```

```
Rc=par['Rc'].value# plotting the optimized parameters from fits
```

```
D=par['D'].value
```

APPENDIX D (Continued)

```

Z0=par['Z0'].value
cov=par['cov'].value
sig=par['sig'].value
xi=par['xi'].value
rhoc=par['rhoc'].value
rhos=[0.334,0.38]
z=arange(-100,100)
edp=decayNp(z,Rc=Rc,z0=Z0,xi=xi,cov=cov,rhos=rhos,rhoc=rhoc,sig=sig,D=D)# electron
density convoluted with roughness and immersion depth distribution

```

```

plot(z,edp,'b-',lw=2)

```

APPENDIX D (CONTINUED)

```

xlabel(r'$\mathbf{z} \ (\AA^{\wedge})$')
ylabel(r'$\mathbf{\rho} \ (el^{\wedge}\AA^{\wedge}\{-3\})$')
xticks([-30,0,30,60,90],fontsize=16)
yticks([0.3,0.45,0.60,0.75])
title('Electron Density Profile',fontsize=16)
grid()
subplot(133)
axis('off')
#    tight_layout()
p_names=[parname[i] for i in range(len(fit)) if fit[i]]
print par

```

```

try:
    ci=conf_interval(minobj,p_names=p_names,sigmas=[0.68])# calculates confidence
interval to 1 sigma

    text(0.0,1.0,r'\underline{Fit Parameters for '+tit+'}',fontsize=16)

    fitpar={ }# list of fit parameters

    for i in range(len(p_names)):

        text(0.0,0.9-
i*0.1,p_names[i]+'='+'%.3f'%ci[p_names[i]][1][1]+'+'+'%.5f'%(nan_to_num(ci[p_names[i]][2][
1])-ci[p_names[i]][1][1])+\
        '/'+'%.5f'%(ci[p_names[i]][1][1]-nan_to_num(ci[p_names[i]][0][1])),fontsize=16)

        text(0.0,0.9-i*0.1,p_names[i]+'='+'%.3f
+/- %.5f'%(par[p_names[i]].value,par[p_names[i]].stderr),fontsize=16)

    fitpar[p_names[i]]={'value':ci[p_names[i]][1][1],'error':[nan_to_num(ci[p_names[i]][2][1])-
ci[p_names[i]][1][1],ci[p_names[i]][1][1]-nan_to_num(ci[p_names[i]][0][1])]}

        fitpar[p_names[i]]={'value':par[p_names[i]].value,'error':[-
par[p_names[i]].stderr,par[p_names[i]].stderr]}

    tight_layout()# separates two plotted figures so their texts do not mesh into each figures
full_output={'qz':data[:,0],'rrf':data[:,1]/rf,'rrf_err':data[:,2]/rf,'qzfit':x,'rrf_fit':y,'z':z,'edp':edp,'fitp
ar':fitpar}# output parameters

    return chisq,full_output# returns chisquared and output parameters

```

APPENDIX D (Continued)

except:# if cannot calculate error bars on the parameters based on confidence interval

print "Error couldnot be estimated"

return chisq # only returns the chi-squared from the fits

CALLING OUT FUNCTION

#####

ref2_038v_2016=ref_err(ddir=ddir,fname='sample_50mM_380_equilibrated_ref.txt',parname=['

D','Rc','Z0','cov','sig','xi','qoff'],param=[58.0,11.0,9.9,99.0,3.9,10.79,-

0.0009],fit=[False,False,True,True,False,True,False],plt=1,tit='380 mV_2016',err='eq')

#####

#Parratt Algorithm With. Fortran Code.

```

subroutine parratt_born(q, lambda, d, rho, beta, Rgen, M, N)
!*****
**
!Subroutine to calculate Specular Reflectivity using Parrat Algorithm with
!Born Approximation for roughness
!M = No. of data points
!N = No. of slabs
!lambda = wavelength
!d = thickness of each slab
!Rgen = generated reflectivtiy data

!q = change in wave vector
!*****
**
double precision :: q(0:M), Rgen(0:M)
double precision :: d(0:N+1), rho(0:N+1), beta(0:N+1), sigma(0:N+1),
qc(0:N+1)
double precision :: lambda
double complex :: X, fact1, fact2, r(0:N+1), k1, k2, fact
double precision, parameter :: re=2.814e-5, pi=3.14157

do j=0,N+1
    qc(j)=dsqrt(16.0d0*pi*re*rho(j))
enddo

```

APPENDIX D (Continued)

```

do i = 1,M
  r(N+1)=dcmplx(0.0d0,0.0d0)
  do j=N,0,-1
    k1=cdsqrt(dcmplx(q(i)**2-qc(j)**2,-32.0d0*beta(j)*pi**2/lambda**2))
    k2=cdsqrt(dcmplx(q(i)**2-qc(j+1)**2,-
32.0d0*beta(j+1)*pi**2/lambda**2))
    X=(k1-k2)*cdexp(-k1*k2*sigma(j+1)**2/2)/(k1+k2)
    fact1=dcmplx(dcos(dble(k2)*d(j+1)),dsin(dble(k2)*d(j+1)))
    fact2=dexp(-aimag(k2)*d(j+1))
    fact=fact1*fact2
    r(j)=(X+r(j+1)*fact)/(1.0+X*r(j+1)*fact)
  enddo
  Rgen(i)=cdabs(r(0))**2
enddo
end subroutine parratt_born

subroutine parratt(q,lambda,d,rho,beta,Rgen,M,N)
!*****
**
!
!M = No. of data points
!N = No. of slabs
!lambda = wavelength
!d = thickness of each slab
!Rgen = generated reflectivity data
!q = change in wave vector
!*****
**
double precision :: q(0:M), Rgen(0:M)
double precision :: d(0:N+1), rho(0:N+1), beta(0:N+1), qc(0:N+1)
double precision :: lambda
double complex :: X, fact1, fact2, r(0:N+1), k1, k2, fact
double precision, parameter :: re=2.814e-5, pi=3.14157

do j=0,N+1
  qc(j)=dsqrt(16.0d0*pi*re*rho(j))
enddo

do i = 1,M
  r(N+1)=dcmplx(0.0d0,0.0d0)
  do j=N,0,-1
    k1=cdsqrt(dcmplx(q(i)**2-qc(j)**2,-32.0d0*beta(j)*pi**2/lambda**2))
    k2=cdsqrt(dcmplx(q(i)**2-qc(j+1)**2,-
32.0d0*beta(j+1)*pi**2/lambda**2))
    X=(k1-k2)/(k1+k2)
    fact1=dcmplx(dcos(dble(k2)*d(j+1)),dsin(dble(k2)*d(j+1)))
    fact2=dexp(-aimag(k2)*d(j+1))
    fact=fact1*fact2
    r(j)=(X+r(j+1)*fact)/(1.0+X*r(j+1)*fact)
  enddo
  Rgen(i)=cdabs(r(0))**2

```

APPENDIX D (Continued)

```

enddo
end subroutine Parratt
#####
3D SPHERICAL NANOPARTICLE MODEL

def ref_residual(par,x,y,yerr):
    Rc1=par['Rc1'].value#single nanoparticle size
    Rc2=par['Rc2'].value#cluster of nanoparticle size
    rho1=par['rho1'].value#electron density of single nanoparticle
    rho2=par['rho2'].value#electron density of cluster
    D1=par['D1'].value# spacing of nanoparticles size
    D2=par['D2'].value# spacing of the cluster
    Z01=par['Z01'].value# depth of nanoparticles
    Z02=par['Z02'].value# depth of nanoparticles
    cov1=par['cov1'].value# coverage of single nanoparticle with respect to
water
    cov2=par['cov2'].value# coverage of nanoparticles with respect to water
    alpha1=par['alpha1'].value
    alpha2=par['alpha2'].value
    xi1=par['xi1'].value
    xi2=par['xi2'].value
    sig=par['sig'].value#roughness
    qoff=par['qoff'].value
    rhos=[0.334,0.38]# electron densities of water and DCE
    lam=0.41328
    rf,r2=parratt(x,lam,[0.0,1e3],rhos,[0.0,0.0]) # Frenel reflectivity

    x=x+qoff #qz offset

    if Z01 or Z02 <0:
        z=pl.arange(-3.0*Rc2,1.5*Rc2)# -500.0
    else:
        z=pl.arange(-1.5*Rc2,3.0*Rc2)
    d=pl.ones_like(z)

edp1=decayNp1(z,Rc1=Rc1,Z01=Z01,xi1=xi1,cov1=cov1,rhos=rhos,rho1=rho1,si
g=sig,D1=D1)
beta=np.zeros_like(z)
rho1=np.array(edp1, dtype='float')

```

APPENDIX D (Continued)

```

    refq1,r2=parratt(x,lam,d,rho1,beta)# square of the amplitude for single
nanoparticle

edp2=decayNp2(z,Rc2=Rc2,Z02=Z02,xi2=xi2,cov2=cov2,rhos=rhos,rhoc2=rhoc2,si
g=sig,D2=D2)
    rho2=np.array(edp2, dtype='float')

    refq2,r2=parratt(x,lam,d,rho2,beta)# square of the amplitude for
cluster
#    rf,r2=parratt(x,lam,[0.0,1e3],rhos,[0.0,0.0])
    refq=(alpha1/100.0*refq1)+(alpha2/100.0*refq2)+(100.0-alpha1-
alpha2)/100.0*rf # Total inhomogenous reflectivity

    if yerr==None:
        return refq/rf-y/rf
    else:
        return (refq-y)/yerr

#pl.figure(figsize=(10,10))
#####
def ref_fun(par,x):
    Rc1=par['Rc1'].value#single nanoparticle size
    Rc2=par['Rc2'].value#cluster of nanoparticle size
    rhoc1=par['rhoc1'].value#electron density of single nanoparticle
    rhoc2=par['rhoc2'].value#electron density of cluster
    D1=par['D1'].value#
    D2=par['D2'].value# spacing of the cluster

    Z01=par['Z01'].value# depth of nanoparticles
    Z02=par['Z02'].value# depth of nanoparticles
    cov1=par['cov1'].value# coverage of single nanoparticle with respect to
water
    cov2=par['cov2'].value# coverage of nanoparticles with respect to water
    alpha1=par['alpha1'].value
    alpha2=par['alpha2'].value
    xi1=par['xi1'].value
    xi2=par['xi2'].value
    sig=par['sig'].value#roughness
    qoff=par['qoff'].value
    rhos=[0.334,0.38]# electron densities of water and DCE
    lam=0.41328
    rf,r2=parratt(x,lam,[0.0,1e3],rhos,[0.0,0.0]) # Frensel reflecity
x=x+qoff #qz offset

```

APPENDIX D (Continued)

```

if Z01 or Z02 <0:
    z=pl.arange(-3.0*Rc2,2.5*Rc2)
else:
    z=pl.arange(-2.5*Rc2,3.0*Rc2)
d=pl.ones_like(z)

spacing of nanoparticles size

edp1=decayNp1(z,Rc1=Rc1,Z01=Z01,xi1=xi1,cov1=cov1,rhos=rhos,rhoc1=rhoc1,si
g=sig,D1=D1)
    beta=np.zeros_like(z)
    rho1=np.array(edp1, dtype='float')

    refq1,r2=parratt(x,lam,d,rho1,beta)# sqaure of the amplitude for single
nanoparticle

edp2=decayNp2(z,Rc2=Rc2,Z02=Z02,xi2=xi2,cov2=cov2,rhos=rhos,rhoc2=rhoc2,si
g=sig,D2=D2)
    rho2=np.array(edp2, dtype='float')

    refq2,r2=parratt(x,lam,d,rho2,beta)# square of the amplitude for
cluster
# rf,r2=parratt(x,lam,[0.0,1e3],rhos,[0.0,0.0])
    refq=(alpha1/100.0*refq1)+(alpha2/100.0*refq2)+(100.0-alpha1-
alpha2)/100.0*rf # Total inhomogenous reflectivity
    return refq/rf

#####
def
decayNp2(z,Rc2=10,D2=30.0,Z02=0.0,xi2=1.0,cov2=100.0,rhoc2=4.65,rhos=[0.33
4,0.38],sig=1.0):
    z2=pl.arange(z[0]-4*int(sig),z[-1]+4*int(sig)+1)
    intf=pl.where(z2<=0,rhos[0],rhos[1])
    if Z02<=0:
        z1=pl.arange(-4*xi2+Z02,Z02)
        dec=pl.exp((z1-Z02)/xi2)/xi2
    else:
        z1=pl.arange(Z02,Z02+4*xi2)
        dec=pl.exp((Z02-z1)/xi2)/xi2

    rhoz=pl.zeros_like(z2)
    for i in range(len(z1)):

rhoz=rhoz+rhoNPz2(z2,Z02=z1[i],rhoc2=rhoc2,Rc2=Rc2,D2=D2,rhos=rhos)*dec[i]
/sum(dec)
    rhoz=cov2*rhoz/100.0+(100-cov2)*intf/100.0
    rough=pl.exp(-pl.arange(-
4*int(sig),4*int(sig)+1)**2/2.0/sig**2)/pl.sqrt(2*pi)/sig
    return pl.convolve(rhoz,rough,mode='valid')

```

APPENDIX D (Continued)

```
#####

def
decayNp1(z,Rc1=10,D1=30.0,Z01=0.0,xi1=1.0,cov1=100.0,rhoc1=1.65,rhos=[0.33
4,0.38],sig=1.0):
    z2=pl.arange(z[0]-4*int(sig),z[-1]+4*int(sig)+1)
    intf=pl.where(z2<=0,rhos[0],rhos[1])
    if Z01<=0:
        z1=pl.arange(-4*xi1+Z01,Z01)
        dec=pl.exp((z1-Z01)/xi1)/xi1
    else:
        z1=pl.arange(Z01,Z01+4*xi1)
        dec=pl.exp((Z01-z1)/xi1)/xi1
    rhoz=pl.zeros_like(z2)
    for i in range(len(z1)):

rhoz=rhoz+rhoNPz1(z2,Z01=z1[i],rhoc1=rhoc1,Rc1=Rc1,D1=D1,rhos=rhos)*dec[i]
/sum(dec)
    rhoz=cov1*rhoz/100.0+(100-cov1)*intf/100.0
    rough=pl.exp(-pl.arange(-
4*int(sig),4*int(sig)+1)**2/2.0/sig**2)/pl.sqrt(2*pi)/sig
    return pl.convolve(rhoz,rough,mode='valid')

#####

def rhoNPz1(z,Z01=0,rhoc1=4.65,Rc1=10.0,D1=28.0,rhos=[0.334,0.38]):
    rhob=pl.where(z>0,rhos[1],rhos[0])
    return pl.where(abs(z-Z01)<=Rc1,(2*pi*(rhoc1-rhob)*(Rc1**2-(z-
Z01)**2)+1.732*rhob*D1**2)/(1.732*D1**2),rhob)

#####

def rhoNPz2(z,Z02=0,rhoc2=1.65,Rc2=10.0,D2=28.0,rhos=[0.334,0.38]):
    rhob=pl.where(z>0,rhos[1],rhos[0])
    return pl.where(abs(z-Z02)<=Rc2,(2*pi*(rhoc2-rhob)*(Rc2**2-(z-
Z02)**2)+1.732*rhob*D2**2)/(1.732*D2**2),rhob)

#####

def
ref_err(ddir='/',fname='sample2_ref_0.60v',err='neq',parname=['D1','D2','R
c1','Rc2','Z01','Z02','cov1','cov2','alpha1','alpha2','rhoc1','rhoc2','xi1
','xi2','sig','qoff'],param=[57.0,130,10.0,90.0,20,20,50,50,30,70,4.65,1.0
,2.3,2.3,4.0,0],\
fit=[False,False,False,False,True,True,True,True,True,True,True,False,True
,True],plt=0,tit=''):
    lam=0.41328
    rhos=[0.334,0.38]
```

APPENDIX D (Continued)

```

data1=pl.loadtxt(d_dir+f_name)
data=pl.zeros_like(data1)
data[:,1]=data1[data1[:,0].argsort(),1]
data[:,0]=data1[data1[:,0].argsort(),0]
data[:,2]=data1[data1[:,0].argsort(),2]
rf=Rf(data[:,0])

if err=='eq':
    data[:,2]=np.array([max(data1[i,2],data1[i,1]*0.01) for i in
range(len(data1[:,2]))])
elif err==None:
    data[:,2]=None
else:
    pass

par=Parameters()

par.add(parname[0], value=param[0], min=50.0, max=70.0,
vary=fit[0])#Single spacing
par.add(parname[1], value=param[1], min=100.0, max=230.0,
vary=fit[1])#Cluster spacing
par.add(parname[2], value=param[2], min=8, max=13,
vary=fit[2])#single size
par.add(parname[3], value=param[3], min=60, max=120.0,
vary=fit[3])#cluster size
par.add(parname[4], value=param[4], min=-60.0, max=60.0,
vary=fit[4])# single position
par.add(parname[5], value=param[5], min=-100.0, max=100.0,
vary=fit[5])#cluster position
par.add(parname[6], value=param[6], min=0.0, max=100.0,
vary=fit[6])#single coverage
par.add(parname[7], value=param[7], min=0.0, max=100.0,
vary=fit[7])#cluster coverage
par.add(parname[8], value=param[8], min=0.0, max=100.0,
vary=fit[8])#single domain
par.add(parname[9], value=param[9], min=0.0, max=100.0,
vary=fit[9])#cluster domain

par.add(parname[10], value=param[10], min=0.0, max=4.65,
vary=fit[10])#single electron density
par.add(parname[11], value=param[11], min=0.0, max=1.0,
vary=fit[11])# cluster electron density

par.add(parname[12], value=param[12], min=0.1, max=5,
vary=fit[12])#decay length of single
par.add(parname[13], value=param[13], min=0.1, max=40.0,
vary=fit[13])#decay length of cluster
par.add(parname[14], value=param[14], min=0.1, max=7.0,
vary=fit[14])#roughness
par.add(parname[15], value=param[15], min=-0.01, max=0.01,
vary=fit[15])#qoff

```

APPENDIX D (Continued)

```

minobj=minimize(ref_residual,par,args=(data[:,0],data[:,1],data[
        :,2]),method='leastsq')

chisq=pl.sum(ref_residual(par,data[:,0],data[:,1],data[:,2])**2)

rhos=[0.334,0.38]
if plt==1:
    pl.figure(figsize=(10,10))
#    fig=pl.figure(figsize=(10,10))
    pl.subplot(2,1,1)
#    pl.yscale('log')
    z=pl.arange(-500,500)
    d=pl.ones_like(z)
    Rc1=par['Rc1'].value
    Rc2=par['Rc2'].value
    D1=par['D1'].value
    D2=par['D2'].value
    Z01=par['Z01'].value
    Z02=par['Z02'].value
    cov1=par['cov1'].value
    cov2=par['cov2'].value
    alpha1=par['alpha1'].value
    alpha2=par['alpha2'].value
    rhoc1=par['rhoc1'].value
    rhoc2=par['rhoc2'].value
    sig=par['sig'].value
    xi1=par['xi1'].value
    xi2=par['xi2'].value
    rhos=[0.334,0.38]

edp1=decayNp1(z,Rc1=Rc1,Z01=Z01,xi1=xi1,cov1=cov1,rhos=rhos,rhoc1=rhoc1,si
g=sig,D1=D1)
    rho1=np.array(edp1,dtype='float')
    beta=np.zeros_like(z)
    x=pl.linspace(0.002,1.2*data[-1,0],100)
    refq1,r2=parratt(x,lam,d,rho1,beta)

edp2=decayNp2(z,Rc2=Rc2,Z02=Z02,xi2=xi2,cov2=cov2,rhos=rhos,rhoc2=rhoc2,si
g=sig,D2=D2)
    rho2=np.array(edp2,dtype='float')
    refq2,r2=parratt(x,lam,d,rho2,beta)
    y=ref_fun(par,x)
    pl.plot(x,y,'b-',lw=2)

```

APPENDIX D (Continued)

```

pl.errorbar(data[:,0],data[:,1]/rf,data[:,2]/rf,fmt='ro')
pl.xlabel(r'$\mathbf{Q_z \ (\AA^{-1})}$')
pl.ylabel(r'$\mathbf{R/R_f}$')
pl.xticks([0.0,0.15,0.3,0.45],fontsize=16)
#   pl.yticks([5e-1,1,10,100,200,300],fontsize=16)
#   pl.ylim(0.8,300)
#   pl.xlim(0,0.35)
pl.title(r''+tit+' $\chi^2$=%.2f'%chisq,fontsize=16)
pl.grid()
pl.subplot(2,1,2)
z=pl.arange(-500,500)
d=pl.ones_like(z)
Rc1=par['Rc1'].value
Rc2=par['Rc2'].value
D1=par['D1'].value
D2=par['D2'].value
Z01=par['Z01'].value
Z02=par['Z02'].value
cov1=par['cov1'].value
cov2=par['cov2'].value
alpha1=par['alpha1'].value
alpha2=par['alpha2'].value
rhoc1=par['rhoc1'].value
rhoc2=par['rhoc2'].value
sig=par['sig'].value
xi1=par['xi1'].value
xi2=par['xi2'].value

edp1=decayNp1(z,Rc1=Rc1,Z01=Z01,xi1=xi1,cov1=cov1,rhos=rhos,rhoc1=rhoc1,si
g=sig,D1=D1)

edp2=decayNp2(z,Rc2=Rc2,Z02=Z02,xi2=xi2,cov2=cov2,rhos=rhos,rhoc2=rhoc2,si
g=sig,D2=D2)
pl.plot(z,edp1,'b-',lw=2)
pl.plot(z,edp2,'r-',lw=2)

#   pl.xlabel(r'$\mathbf{z \ (\AA)}$')
#   pl.ylabel(r'$\mathbf{\rho \ (e1/\AA^{-3})}$')

report_fit(minobj)

```

```
#####
```

APPENDIX D (Continued)

OUTPUT CALLING FUNCTION

```

ddir='C:\\Users\\damoan2\\Documents\\2016nov\\'

ref_035v=ref_err(ddir=ddir,fname="sample_50mM_350_first_data_ref.txt",
                parname=['D1','D2','Rc1','Rc2','Z01','Z02','cov1','cov2','alpha1','alpha2',
                        'rhoc1','rhoc2','xi1','xi2','sig','qoff'],param=[65.0,179,10.0,79.7,22.5,-47.0,
                        94.0,90,80.0,15.0,4.65,0.8,3.72,28.0,3.65,-0.0000],fit=[False,False,False,True,False,True,
                        True,True, False,True,False,True,False,False,False,False],plt=1,tit=",err='eq')
#####

```

MESH CALCULATION

In the ref_err() function in the models, you make it return the chisquared calculated. In this function, I made a list([]) out of the ref_err() function and appended all chi-squared calculated in the erf function with the list created out of it. So it returns an array of chi-squared

```
ddir='C:\\Users\\damoan2\\Documents\\2016nov\\'
```

```
Z01=21;D2=200;del1=60;del2=80
```

```
var=[]# List for Z01 and Z02 pairs used in order
```

```
for i in pl.arange(Z01-del1, Z01+del1,1.0):
```

```
    for k in pl.arange(D2-del2,D2+del2,1.0):
```

```
        var.append((i,k))
```

the ref_err() returns output parameters (par) and the chisquared rerr. I am interested in the rerr.

You can also make the function return only the chisquared, rerr.

```
par, rerr=ref_err(ddir=ddir,fname='sample_50mM_350_first_data_ref.txt',
```

APPENDIX D (Continued)

```

parname=['D1','D2','Rc1','Rc2','Z01','Z02','cov1','cov2','alpha1','alpha2',
        'rhoc1','rhoc2','xi1','xi2','sig','qoff'],param=[65.0,k,10.0,89.9,i,20,
        100.0,100.0,
        68,13.5,4.65,0.77,
        3.26,2.26,3.8,0.0000],fit=[False,False,False,False,False,False,False,False,False,False,False,
False,False,False,False],plt=1,tit='0.35V',err='eq')
x=pl.arange(Z01-del1, Z01+del1,1)
y=pl.arange(D2-del2, D2+del2,1)
Z = [[rerr[i*len(y)+j] for i in range(len(x))] for j in range(len(y))]
print '*****'
fig=plt.figure()
cax=plt.imshow(Z, cmap='hot',interpolation='nearest',extent=[min(x),max(x),min(y),max(y)])
cbar=fig.colorbar(cax, shrink=0.9, aspect=10, orientation='horizontal')
cbar.ax.set_xticklabels(['Low', 'Medium', 'High'])
plt.title('Depths of single Nanoparticles versus Spacing of cluster')
pl.xlabel('Z01(Single Nanoparticle)')
pl.ylabel('D2(Cluster spacing)')

```

APPENDIX D (Continued)

#GAUSSIAN SLAB MODEL FOR 3D NANOPARTICLE ANALYSIS. CLUSTERS ARE ASSUMED TO BE DIFFUSED ASSEMBLY OF SINGLE NANOPARTICLES.

```

from lmfit import Parameters
import numpy as np
import sys
import os
sys.path.append(os.path.abspath('.'))
sys.path.append(os.path.abspath('./Functions'))
sys.path.append(os.path.abspath('./Fortran_routines/'))
#####Please do not remove lines above#####

#####Import your modules below if needed#####
from xr_ref import parratt

class MultiSphereAtInterface: #Please put the class name same as the function name
def
__init__(self,x=0.1,E=10.0,Rc=10.0,rhoc=4.68,Tsh=20.0,rhosh=0.0,rhoup=0.333,rhdown=0.38,
sig=3.0,          mpar={'Z0':[20],'cov':[1.0],'Z0sig':[0.0]},Nlayers=111,rrf=1,qoff=0.0,zmin=-
10,zmax=100,Nc=20):
"""
Calculates X-ray reflectivity from multilayers of core-shell spherical nanoparticles assembled near
an interface
-----
Variable Description
-----
x array of wave-vector transfer along z-direction
E Energy of x-rays in inverse units of x
Rc Radius of the core of the nanoparticles
rhoc Electron density of the core
Tsh Thickness of the outer shell
rhosh Electron Density of the outer shell. If 0, the electron density the shell region will be assumed
to be filled by the bulk phases depending upon the position of the nanoparticles
rhoup Electron density of the upper bulk phase
rhdown Electron density of the lower bulk phase
sig Roughness of the interface

```

APPENDIX D (Continued)

`mpar` The layer parameters where, `d`: thickness of each layer, `rho`: Electron ensity of each layer, `beta`: Absorption coefficient of each layer, `sig`: roughness of interface separating each layer. The upper and lower thickness should be always fixed. The roughness of the topmost layer should be always kept 0.

`Nlayers` The number of layers in which the layers will be subdivided for applying Parratt formalism

`rrf` 1 for Frensel normalized refelctivity and 0 for just reflectivity

`qoff` q-offset to correct the zero q of the instrument

`zmin` minimum depth for electron density calculation

`zmax` maximum depth for electron density calculation

`Nc` Number of points for convoluting interface roughness and electron density profile

"""

```
if type(x)==list:
```

```
self.x=np.array(x)
```

```
else:
```

```
self.x=x
```

```
self.E=E
```

```
self.Rc=Rc
```

```
self.rhoc=rhoc
```

```
self.Tsh=Tsh
```

```
self.rhosh=rhosh
```

```
self.rhoup=rhoup
```

```
self.rhodown=rhodown
```

```
self.zmin=zmin
```

```
self.zmax=zmax
```

```
self.Nc=Nc
```

```
self.sig=sig
```

```
self.__mpar__=mpar
```

```
self.Nlayers=Nlayers
```

```
self.rrf=rrf
```

```
self.qoff=qoff
```

```
self.choices={'rrf':[1,0]}
```

```
self.init_params()
```

```
def init_params(self):
```

```
"""
```

```
Define all the fitting parameters like
```

```
self.param.add('sig',value=0,vary=0)
```

```
"""
```

```
self.params=Parameters()# SETTING PARAMETER SPACE
```

```
self.params.add('Rc',value=self.Rc,vary=0,min=-
```

```
np.inf,max=np.inf,expr=None,brute_step=None)
```

APPENDIX D (Continued)

```

self.params.add('rhoc',value=self.rhoc,vary=0,min=-
np.inf,max=np.inf,expr=None,brute_step=None)
self.params.add('Tsh',value=self.Tsh,vary=0,min=-
np.inf,max=np.inf,expr=None,brute_step=None)
self.params.add('rhosh',value=self.rhosh,vary=0,min=-
np.inf,max=np.inf,expr=None,brute_step=None)

self.params.add('sig',value=self.sig,vary=0,min=-
np.inf,max=np.inf,expr=None,brute_step=None)
for key in self.__mpar__.keys():
for i in range(len(self.__mpar__[key])):
self.params.add('__%s__%03d'%(key,i),value=self.__mpar__[key][i],vary=0,min=-
np.inf,max=np.inf,expr=None,brute_step=None)
self.params.add('qoff',self.qoff,vary=0,min=-np.inf,max=np.inf,expr=None,brute_step=None)

#####
def
NpRho(self,z,Rc=10,rhoc=4.68,Tsh=20,rhosh=0.0,Z0=20,rhoup=0.333,rhdown=0.38,cov=1.0):
D=Rc+Tsh
Atot=2*np.sqrt(3)*D**2# HEXAGONAL AREAR
rhos=np.where(z>0,rhdown,rhoup)# take the first number(rhdown) if condition satisfied else
take the second
Acore=np.pi*np.sqrt(np.where(z>Z0+Rc,0.0,Rc**2-(z-Z0)**2)*np.where(z<Z0-Rc,0.0,Rc**2-
(z-Z0)**2))# Area of the core nanoparticle
ANp=np.pi*np.sqrt(np.where(z>Z0+D,0.0,D**2-(z-Z0)**2)*np.where(z<Z0-D,0.0,D**2-(z-
Z0)**2))
if rhosh<1e-3:# electron density of the ligand
return (1-cov)*rhos+cov*((Atot-ANp)*rhos+Acore*(rhoc-rhos)+ANp*rhos)/Atot
else:
return (1-cov)*rhos+cov*((Atot-ANp)*rhos+Acore*(rhoc-rhosh)+ANp*rhosh)/Atot

#####
def
NpRhoGauss(self,z,Rc=10,rhoc=4.68,Tsh=20,rhosh=0.0,Z0=[20],cov=[1.0],Z0sig=[0.0],rhoup=
0.333,rhdown=0.38,sig=3.0,Nc=20):
if sig<1e-3:
zt=z
else:
Nmax=len(z)+Nc
zmin=z[0]-(z[1]-z[0])*Nc/2
zmax=z[-1]+(z[1]-z[0])*Nc/2

```

APPENDIX D (Continued)

```

zt=np.linspace(zmin,zmax,Nmax)
rhosum=np.zeros_like(zt)
for i in range(len(Z0)):
if Z0sig[i]<1e-3:
rhosum=rhosum+self.NpRho(zt,Rc=Rc,rhoc=rhoc,Tsh=Tsh,rhosh=rhosh,Z0=Z0[i],rhoup=rhoup,
rhodown=rhodown,cov=cov[i])
else:
Z1=np.linspace(Z0[i]-5*Z0sig[i],Z0[i]+5*Z0sig[i],101)
dist=np.exp(-(Z1-Z0[i])**2/2/Z0sig[i]**2)
norm=np.sum(dist)

tsum=np.zeros_like(len(zt))
for j in range(len(Z1)):
tsum=tsum+self.NpRho(zt,Rc=Rc,rhoc=rhoc,Tsh=Tsh,rhosh=rhosh,Z0=Z1[j],rhoup=rhoup,rhod
own=rhodown,cov=cov[i])*dist[j]
rhosum=rhosum+tsum/norm
rhos=np.where(zt>0,rhodown,rhoup)
rho=rhosum-(len(Z0)-1)*rhos
if sig<1e-3:
return rho
else:
x=np.arange(-Nc/2,Nc/2+1)*(z[1]-z[0])
rough=np.exp(-x**2/2/sig**2)/np.sqrt(2*np.pi)/sig
return np.convolve(rho,rough,mode='valid')*(x[1]-x[0])

#####
def calcProfile(self):
"""
Calculates the electron and absorption density profiles
"""
Z0=np.array([self.params['__Z0__%03d'%i].value for i in range(len(self.__mpar__['Z0'])])
cov=np.array([self.params['__cov__%03d'%i].value for i in range(len(self.__mpar__['cov'])])
Z0sig=np.array([self.params['__Z0sig__%03d'%i].value for i in
range(len(self.__mpar__['Z0sig'])])
self.__z__=np.linspace(self.zmin,self.zmax,self.Nlayers)
self.__d__=(self.__z__[1]-self.__z__[0])*np.ones_like(self.__z__)
self.__rho__=self.NpRhoGauss(self.__z__,Rc=self.Rc,rhoc=self.rhoc,Tsh=self.Tsh,rhosh=self.rh
osh,Z0=Z0,cov=cov,Z0sig=Z0sig,rhoup=self.rhoup,rhodown=self.rhodown,sig=self.sig,Nc=self.
Nc)
self.output_params['Total density profile']={'x':self.__z__, 'y':self.__rho__}
for i in range(len(Z0)):

```

APPENDIX D (Continued)

```
rho=self.NpRhoGauss(self.__z__,Rc=self.Rc,rhoc=self.rhoc,Tsh=self.Tsh,rhosh=self.rhosh,Z0=[
Z0[i]],cov=[cov[i]],Z0sig=[Z0sig[i]],rhoup=self.rhoup,rhodown=self.rhodown,sig=self.sig,Nc=s
elf.Nc)
self.output_params['Layer %d contribution'%(i+1)]={'x':self.__z__, 'y':rho}
```

```
#####
```

```
def y(self):
    """
```

```
Define the function in terms of x to return some value
```

```
"""
```

```
self.output_params={}
self.calcProfile()
x=self.x+self.qoff
lam=6.62607004e-34*2.99792458e8*1e10/self.E/1e3/1.60217662e-19
refq,r2=parratt(x,lam,self.__d__,self.__rho__,np.zeros_like(self.__rho__))
if self.rrf>0:
    rhos=[self.__rho__[0],self.__rho__[-1]]
    betas=[0,0]
    ref,r2=parratt(x,lam,[0.0,1.0],rhos,betas)

refq=refq/ref
return refq
```

```
if __name__=='__main__':
    x=np.arange(0.001,1.0,0.1)
    fun=MultiSphereAtInterface(x=x)
    print(fun.y())
```

APPENDIX D (Continued)

The function below is similar to the first 2D spherical model used in fitting. Except that, it has a Gaussian immersion distribution depth.

```
#####
```

```
#####Please do not remove lines below#####
```

```
from lmfit import Parameters
import numpy as np
APPENDIX D (CONTINUED)
```

```
import sys
import os
sys.path.append(os.path.abspath('.'))
sys.path.append(os.path.abspath('./Functions'))
sys.path.append(os.path.abspath('./Fortran_routines/'))
#####Please do not remove lines above#####
```

```
#####Import your modules below if needed#####
```

```
from xr_ref import parratt
```

```
class SphereAtInterface: #Please put the class name same as the function name
def __init__(self,x=0.1,lam=1.0,R=10,Rsig=0.0,rhoc=1.0,D=60.0,
cov=100,Zo=20.0,decay=3.0,rho_up=0.333,rho_down=0.38,zmin=-
50,zmax=100,Nlayers=151,Nc=20,roughness=3.0,rrf=1,mpar={ },qoff=0):
"""
```

Calculates X-ray reflectivity from a system of nanoparticle at an interface between two media

x : array of wave-vector transfer along z-direction

lam : wavelength of x-rays in invers units of x

R : Radius of nanoparticles in inverse units of x

rhoc : Electron density of the nanoparticles

cov : Coverate of the nanoparticles in %

D : The lattice constant of the two dimensional hcp structure formed by the particles

Zo : Average distance between the center of the nanoparticles and the interface

decay : Assuming exponential decay of the distribution of nanoparticles away from the interface

rho_up : Electron density of the upper medium

rho_down : Electron density of the lower medium

zmin : Minimum z value for the electron density profile

zmin : Maximum z value for the electron density profile

Nlayers : The total number of layers in which the electron density profile will be divided to apply Parratt Formalism

APPENDIX D (Continued)

Nc : The number of points used for convolution of interfacial roughness with electron density profile

roughness : Roughness of the interface

rrf : 1 for Frensel normalized reflectivity and 0 for just reflectivity

qoff : offset in the value of qz due to alignment errors

"""

```
if type(x)==list:
```

```
self.x=np.array(x)
```

```
else:
```

```
self.x=x
```

```
self.R=R
```

```
self.lam=lam
```

```
self.rhoc=rhoc
```

```
self.Zo=Zo
```

```
self.cov=cov
```

```
self.D=D
```

```
self.decay=decay
```

```
self.rho_up=rho_up
```

```
self.rho_down=rho_down
```

```
self.zmin=zmin
```

```
self.zmax=zmax
```

```
self.Nlayers=Nlayers
```

```
self.Nc=Nc
```

```
self.roughness=roughness
```

```
self.rrf=rrf
```

```
self.qoff=qoff
```

```
self.choices={ }
```

```
self.output_params={ }
```

```
self.__mpar__=mpar
```

```
def init_params(self):
```

```
"""
```

```
Define all the fitting parameters like
```

```
self.param.add('sig',value=0,vary=0)
```

```
"""
```

```
self.params=Parameters()
```

```
self.params.add('R',value=self.R,vary=0,min=-np.inf,max=np.inf,expr=None,brute_step=None)
```

```
self.params.add('rhoc',value=self.rhoc,vary=0,min=-
```

```
np.inf,max=np.inf,expr=None,brute_step=None)
```

```
self.params.add('Zo',value=self.Zo,vary=0,min=-
```

```
np.inf,max=np.inf,expr=None,brute_step=None)
```

```
self.params.add('D',value=self.D,vary=0,min=-np.inf,max=np.inf,expr=None,brute_step=None)
```

APPENDIX D (Continued)

```

self.params.add('cov',value=self.cov,vary=0,min=-
np.inf,max=np.inf,expr=None,brute_step=None)
self.params.add('decay',value=self.decay,vary=0,min=-
np.inf,max=np.inf,expr=None,brute_step=None)
self.params.add('roughness',value=self.roughness,vary=0,min=-
np.inf,max=np.inf,expr=None,brute_step=None)

self.params.add('qoff',value=self.qoff,vary=0,min=-
np.inf,max=np.inf,expr=None,brute_step=None)

def
decayNp(self,z,Rc=10,D=30.0,z0=0.0,xi=1.0,cov=100.0,rhoc=4.65,rhos=[0.334,0.38],sig=1.0,N
c=20):
if sig<1e-3:
z2=z
else:
Nmax=len(z)+Nc
zmin=z[0]-(z[1]-z[0])*Nc/2
zmax=z[-1]+(z[1]-z[0])*Nc/2
z2=np.linspace(zmin,zmax,Nmax)
intf=np.where(z2<=0,rhos[0],rhos[1])
if z0<=0:
z1=np.arange(-4*xi+z0,z0)
dec=np.exp((z1-z0)/xi)/xi
else:
z1=np.arange(z0,z0+4*xi)
dec=np.exp((z0-z1)/xi)/xi
rhoz=np.zeros_like(z2)
for i in range(len(z1)):
rhoz=rhoz+self.rhoNPz(z2,z0=z1[i],rhoc=rhoc,Rc=Rc,D=D,rhos=rhos)*dec[i]/sum(dec)
rhoz=cov*rhoz/100.0+(100-cov)*intf/100.0
x=np.arange(-Nc/2,Nc/2+1)*(z[1]-z[0])
if sig>1e-3:
rough=np.exp(-x**2/2.0/sig**2)/np.sqrt(2*np.pi)/sig
return np.convolve(rhoz,rough,mode='valid')
else:
return rhoz

```

APPENDIX D (Continued)

```

def rhoNPz(self,z,z0=0,rhoc=4.65,Rc=10.0,D=28.0,rhos=[0.334,0.38]):
    rhob=np.where(z>0,rhos[1],rhos[0])
    #D=D/2
    return np.where(np.abs(z-z0)<=Rc,(2*np.pi*(rhoc-rhob)*(Rc**2-(z-
z0)**2)+1.732*rhob*D**2)/(1.732*D**2),rhob)

def y(self):
    """
    Define the function in terms of x to return some value
    """
    Rc=self.params['R'].value
    D=self.params['D'].value
    Zo=self.params['Zo'].value
    cov=self.params['cov'].value
    sig=self.params['roughness'].value
    xi=self.params['decay'].value
    rhoc=self.params['rhoc'].value
    qoff=self.params['qoff'].value
    rhos=[self.rho_up,self.rho_down]
    lam=self.lam
    z=np.linspace(self.zmin,self.zmax,self.Nlayers)
    d=np.ones_like(z)
    edp=self.decayNp(z,Rc=Rc,z0=Zo,xi=xi,cov=cov,rhos=rhos,rhoc=rhoc,sig=sig,D=D,Nc=self.Nc
    )
    self.output_params['EDP']={'x':z,'y':edp}
    beta=np.zeros_like(z)
    rho=np.array(edp,dtype='float')
    refq,r2=parratt(self.x+qoff,lam,d,rho,beta)
    if self.rrf>0:
        ref,r2=parratt(self.x+qoff,lam,[0.0,1.0],rhos,[0.0,0.0])
        refq=refq/ref
    return refq

if __name__=='__main__':
    x=np.arange(0.001,1.0,0.1)
    fun=SphereAtInterface(x=x)
    print(fun.y())

```

APPENDIX D (Continued)

GAUSSIAN FUNCTION USED IN THE IMMERSION DEPTH DISTRIBUTION FUNCTION IN THE 3D XR GAUSSIAN MODEL

```

import numpy as np
from lmfit import Parameters

class Gaussian:
def __init__(self,x=0.0,mu=0.5,sig=0.1,norm=1.0,bkg=0.0,mpar={ }):
    """
    Provides Gaussian function
    x: Scalar or array of values
    mu: Peak position
    sig: Width
    norm: Normalization constant
    bkg: Constant background
    """
    self.x=x
    self.mu=mu
    self.sig=sig
    self.norm=norm
    self.bkg=0.0
    self.__mpar__=mpar
    self.choices={}
    self.output_params={}

def init_params(self):
    self.params=Parameters()
    self.params.add('mu',value=self.mu,vary=0,min=-
np.inf,max=np.inf,expr=None,brute_step=None)
    self.params.add('sig',value=self.sig,vary=0,min=-
np.inf,max=np.inf,expr=None,brute_step=None)
    self.params.add('norm',value=self.norm,vary=0,min=-
np.inf,max=np.inf,expr=None,brute_step=None)
    self.params.add('bkg',value=self.bkg,vary=0,min=-
np.inf,max=np.inf,expr=None,brute_step=None)

#####
def y(self):
return self.norm*np.exp(-(self.x-self.mu)**2/2.0/self.sig**2)/self.sig/2.5066+self.bkg

```

APPENDIX E

GISAXS ANALYSIS .LOG NORMAL DISTRIBUTION FUNCTION IN THE FORM FACTOR
ANALYSIS.

```

import numpy as np
from lmfit import Parameters
#####
class LogNormal:
    """
    Provides log-normal function
    """
    def __init__(self,x=0.0,mu=0.5,sig=0.1,norm=1.0,bkg=0.0,mpar={ }):
        """
        Provides log-normal function  $y=norm*\exp(-(\log(x)-\log(\mu))^{**2}/2/sig^{**2})/\sqrt{2*\pi}/sig/x+bkg$ 
        x: scalar or array of values
        mu: Peak of the Gaussian part of the distribution
        sig: Width of the Gaussian part of the distribution
        norm: Normalization constant
        bkg: Constant background
        """
        self.x=x
        self.mu=mu
        self.sig=sig
        self.norm=norm
        self.bkg=bkg
        self.__mpar__=mpar
        self.choices=None
        self.output_params={}
        #####
        def init_params(self):
            self.params=Parameters()
            self.params.add('mu',value=self.mu,vary=0,min=-
            np.inf,max=np.inf,expr=None,brute_step=None)
            self.params.add('sig',value=self.sig,vary=0,min=-
            np.inf,max=np.inf,expr=None,brute_step=None)
            self.params.add('norm',value=self.norm,vary=0,min=-
            np.inf,max=np.inf,expr=None,brute_step=None)

```

APPENDIX E (Continued)

```
self.params.add('bkg',value=self.bkg,vary=0,min=-
np.inf,max=np.inf,expr=None,brute_step=None)
```

```
#####
def y(self):
return self.norm*np.exp(-(np.log(self.x)-
np.log(self.mu))**2/2.0/self.sig**2)/self.x/self.sig/2.5066+self.bkg
```

```
#####
```

FORM FACTOR ANALYSIS OF THE INTEGRATED INTENSITY FOR THE 3D

CLUSTER

```
# import necessary modules for the class
from lmfit import Parameters #Please do not remove this line
import numpy as np
import sys
import os
sys.path.append(os.path.abspath('./Functions'))# Gives you access to the 'Functions' containing
the lognormal and Gaussian functions
from FormFactors import Sphere
```

```
#####
class Rod_Sphere: #Please put the class name same as the function name
def __init__(self,x=0, R=10.0, Rsig=0.0, dist='Gaussian', qc=0.0217, qpar=0.1,
qparsig=0.0,norm=1.0, bkg=0.0,mpar={ }):
"""
```

Provides rod scan from spherical objects dispersed on a substrate

x: array of Qz values of rod scan

R: Mean radius of spheres in inverse units of Qz

Rsig: Width of distribution of spheres in inverse units of Qz

dist: 'Gaussian' or 'LogNormal'

qc: Critical wave-vector for the substrate on which sphere are aranged

qpar: In-plane wave-vector at which the rod was measured

qparsig: The width of the peak at which the rod was measured

norm: Normalization constant

bkg: Constant background

APPENDIX E (Continued)

```

"""
if type(x)==list:

self.x=np.array(x)
else:
self.x=x
self.R=R
self.Rsig=Rsig
self.dist=dist
self.qc=qc
self.qpar=qpar
self.qparsig=qparsig
self.norm=norm
self.bkg=bkg
self.N=50
self.__mpar__=mpar
self.choices={'dist':['Gaussian','LogNormal']}
self.output_params={}

def init_params(self):
"""
Define all the fitting parameters like
self.param.add('sig',value=0,vary=0)
"""
self.params=Parameters()
self.params.add('R',value=self.R,vary=0,min=-np.inf,max=np.inf,expr=None,brute_step=None)
self.params.add('Rsig',value=self.Rsig,vary=0,min=-
np.inf,max=np.inf,expr=None,brute_step=None)
self.params.add('qc',value=self.qc,vary=0,min=-np.inf,max=np.inf,expr=None,brute_step=None)
self.params.add('norm',value=self.norm,vary=0,min=-
np.inf,max=np.inf,expr=None,brute_step=None)
self.params.add('bkg',value=self.bkg,vary=0,min=-
np.inf,max=np.inf,expr=None,brute_step=None)

def trans(self,qz,qc):
"""
Calculates the transmission Coefficient
"""

```

APPENDIX E (Continued)

```

tr=2.0*qz/(qz+np.sqrt(qz**2-qc**2+0j))
return np.abs(tr)**2

def y(self):
    """
    Define the function in terms of x to return some value
    """
    if self.qparsig>1e-3:
        qpar=np.linspace(self.qpar-5*self.qparsig,self.qpar+5*self.qparsig,10)
        peak=np.exp(-(qpar-self.qpar)**2/2.0/self.qparsig**2)
        peaksum=np.sum(peak)
        distsum=np.zeros_like(self.x)
        for i in range(len(qpar)):
            q=np.sqrt(self.x**2+qpar[i]**2)
            sphere=Sphere.Sphere(x=q,R=self.R,Rsig=self.Rsig,dist=self.dist)
            sphere.N=self.N
            distsum=distsum+sphere.y()*peak[i]
        res=self.norm*distsum*self.trans(self.x,self.qc)/peaksum+self.bkg
    else:
        q=np.sqrt(self.x**2+self.qpar**2)
        sphere=Sphere.Sphere(x=q,R=self.R,Rsig=self.Rsig,dist=self.dist)
        sphere.N=self.N
        res=self.norm*sphere.y()*self.trans(self.x,self.qc)+self.bkg
    if self.Rsig>1e-3:
        self.output_params['Distribution']=sphere.output_params['Distribution']
    return res

if __name__=='__main__':
    x=np.arange(0.001,1.0,0.1)
    fun=Rod_Sphere(x=x)
    print(fun.y())

```

APPENDIX E (Continued)

```
#####
```

SPHERICAL NANOPARTICLE FORM FACTOR FUNCTION

```
import numpy as np
from lmfit import Parameters
import sys
import os
sys.path.append(os.path.abspath('.'))
sys.path.append(os.path.abspath('./Functions'))

from utils import find_minmax
from PeakFunctions import Gaussian, LogNormal

#####
class Sphere:
def __init__(self, x=0.001, R=1.0, Rsig=0.0, dist='Gaussian', N=50, rhoc=1.0, rhosol=0.0,
norm=1.0, bkg=0.0, mpar={}):
"""
Calculates the form factor of a solid sphere with size distribution
x: Array of q-values in the same reciprocal unit as R and Rsig
R: Mean radius of the solid spheres
Rsig: Width of the distribution of solid spheres
dist: Gaussian or LogNormal
N: No. of points on which the distribution will be calculated
rhoc: Electron density of the particle
rhosol: Electron density of the solvent or surrounding environment
"""
if type(x)==list:
self.x=np.array(x)
else:
self.x=x
self.R=R
self.Rsig=Rsig
self.dist=dist
self.rhoc=rhoc
self.rhosol=rhosol
self.norm=norm
self.bkg=bkg
self.N=N
self.__mpar__=mpar
```

APPENDIX E (Continued)

```

self.choices={'dist':['Gaussian','LogNormal']}
self.output_params={}

#####
def init_params(self):
self.params=Parameters()
self.params.add('R',value=self.R,vary=0,min=-np.inf,max=np.inf,expr=None,brute_step=None)
self.params.add('Rsig',value=self.Rsig,vary=0,min=-
np.inf,max=np.inf,expr=None,brute_step=None)

self.params.add('rhoc',value=self.rhoc,vary=0,min=-
np.inf,max=np.inf,expr=None,brute_step=None)
self.params.add('rhol',value=self.rhol,vary=0,min=-
np.inf,max=np.inf,expr=None,brute_step=None)
self.params.add('norm',value=self.norm,vary=0,min=-
np.inf,max=np.inf,expr=None,brute_step=None)
self.params.add('bkg',value=self.bkg,vary=0,min=-
np.inf,max=np.inf,expr=None,brute_step=None)

#####
def y(self):
rho=self.rhoc-self.rhol
if self.Rsig<1e-3:
return self.norm*rho**2*(np.sin(self.x*self.R)-
self.x*self.R*np.cos(self.x*self.R))**2/self.x**6+self.bkg
else:
if self.dist=='Gaussian':
gau=Gaussian.Gaussian(x=0.001,mu=self.R,sig=self.Rsig)
rmin,rmax=find_minmax(gau,self.R,self.Rsig)
r=np.linspace(rmin,rmax,self.N)
gau.x=r
dist=gau.y()
sumdist=np.sum(dist)
self.output_params['Distribution']={'x':r,'y':dist/sumdist}
if type(self.x)==np.ndarray:
ffactor=[]
for x in self.x:
f=np.sum((np.sin(x*r)-x*r*np.cos(x*r))**2*dist/x**6)
ffactor.append(f/sumdist)
return self.norm*rho**2*np.array(ffactor)+self.bkg

```

APPENDIX E (Continued)

```

else:
return self.norm*rho**2*np.sum((np.sin(self.x*r)-
self.x*r*np.cos(self.x*r))**2*dist/self.x**6)/sumdist+self.bkg
elif self.dist=='LogNormal':
lgn=LogNormal.LogNormal(x=0.001,mu=self.R,sig=self.Rsig)
rmin,rmax=find_minmax(lgn,self.R,self.Rsig)
r=np.linspace(rmin,rmax,self.N)
lgn.x=r
dist=lgn.y()
sumdist=np.sum(dist)
self.output_params['Distribution']={'x':r,'y':dist/sumdist}
if type(self.x)==np.ndarray:
ffactor=[]
for x in self.x:
f=np.sum((np.sin(x*r)-x*r*np.cos(x*r))**2*dist/x**6)
ffactor.append(f/sumdist)
return self.norm*rho**2*np.array(ffactor)+self.bkg
else:
return self.norm*rho**2*np.sum((np.sin(self.x*r)-
self.x*r*np.cos(self.x*r))**2*dist/self.x**6)/sumdist+self.bkg
else:
return np.ones_like(x)

```

```
#####
```

APPENDIX F

LORENTZIAN FUNCTION FIT FOR GISAXS IN-PLANE AND OUT-OF PLANE ANALYSIS.

```
def func_Lorentzian(q, fac0,q0,w0):# Lorentzian function

    return fac0*w0/((q-q0)**2+(w0/2)**2)/2/pi

#####
def func_Polynomial(q,a0,a1):# Actually a linear function but initially a polynomial was used.

    return a0+(a1*q)

#####

def sum_LorentzianPeak_PolynomialBac(x,fac2,fac3,fac4,q02,q03,q04,w2,w3,w4,a0,a1):

# Add all the linear and Lorentian functions

    p1=func_Polynomial(x,a0,a1)

    p2=func_Lorentzian(x,fac2,q02,w2)

    p3=func_Lorentzian(x,fac3,q03,w3)

    p4=func_Lorentzian(x,fac4,q04,w4)

    return p1+p2+p3+p4

#####

def peak_residue_Lorentzian_Polynomial(x,y,fac2,fac3,fac4,q02,q03,q04,w2,w3,w4,a0,a1):

# residual from the fit functions

    p1=func_Polynomial(x,[a0,a1])

    p2=func_Lorentzian(x,[fac2,q02,w2])

    p3=func_Lorentzian(x,[fac3,q03,w3])
```

APPENDIX F (Continued)

```

p4=func_Lorentzian(x,[fac4,q04,w4])

return y-(p1+p2+p3+p4)

tfont=16

def
peak_fit(data,qmin=0,qmax=0.29,tit=",col=",Fit=","plt=[0,1],fname='potential_400mV',ddir='\'):
    if plt[0]==0:
        ind=nonzero(where(data[:,0]>qmin,data[:,0],0)*where(data[:,0]<qmax,1.0,0))
        x=data[:,0][ind];y=data[:,1][ind];y_err=data[:,2][ind]
        x=pl.array(x);y=pl.array(y);y_err=pl.array(y_err)
        fac2,fac3,fac4,q02,q03,q04,w2,w3,w4,a0,a1
        =(1.0,0.108,0.1,0.1004,0.173,0.202,0.02,0.02,0.012,0.75,-6.978)
        p0 = (fac2,fac3,fac4,q02,q03,q04,w2,w3,w4,a0,a1)
        popt,pcov=curve_fit(sum_LorentzianPeak_PolynomialBac,x,y,p0,maxfev=80000000)
        fac2,fac3,fac4,q02,q03,q04,w2,w3,w4,a0,a1 =popt
        "fac2_err,fac3_err,fac4_err,q02_err,q03_err,q04_err,w2_err,w3_err,w4_err,a0_err,a1_err,a2_err,
a3_err=", pcov[0]
        print popt
        subplot(121)
        pl.plot(0,0,'k-',label=Fit)

```

APPENDIX F (Continued)

```

plot(x,y,col,label=tit)#original

plot(x,sum_LorentzianPeak_PolynomialBac(x,*popt),color='k')

xlabel(r'$\mathbf{Q}_{xy}(\AA^{-1})$',fontsize=tfont)

ylabel(r'$\mathbf{Normalised\ Int.\ Intensity}$',fontsize=tfont)

qmin = round(qmin, 2)

qmax = round(qmax, 2)

xticks(linspace(qmin,qmax,3),fontsize=tfont)

yticks(linspace(0,0.15,4),fontsize=tfont)

pl.title(r'$\mathbf{Right\ Peak}$',fontsize=tfont)

pl.legend(loc='best',fontsize=16)

x=pl.array(x)

y=pl.array(y)

y_fit=pl.array(sum_LorentzianPeak_PolynomialBac(x,*popt))

y_err=pl.array(y_err)

np.savetxt('C:\Users\damoan2\Documents\December_Analysis_2017\Save_GISAXS_In_Plane_
Fits\RightPeak'+fname, np.vstack((x, y,y_err, y_fit)).T)

if plt[1]==1:

    ind=nonzero(where(data[:,0]>-qmax,data[:,0],0)*where(data[:,0]<-qmin,1.0,0))

    x=data[:,0][ind];y=data[:,1][ind];y_err=data[:,2][ind]

    x=pl.array(x);y=pl.array(y);y_err=pl.array(y_err)

```

APPENDIX F (Continued)

```

fac2,fac3,fac4,q02,q03,q04,w2,w3,w4,a0,a1          =(1.0,0.108,0.1,-0.1004,-0.173,-
0.202,0.02,0.02,0.012,-0.75,6.978)

p01 = (fac2,fac3,fac4,q02,q03,q04,w2,w3,w4,a0,a1)

popt1,pcov1=curve_fit(sum_LorentzianPeak_PolynomialBac,x,y,p01,maxfev=80000000)

fac2,fac3,fac4,q02,q03,q04,w2,w3,w4,a0,a1=p01

print popt1

#   print "fac2,fac3,fac4,q02,q03,q04,w2,w3,w4,a0,a1=", popt1

subplot(122)

pl.plot(0,0,'k-',label=Fit)

plot(x,y,col,label=tit)

plot(x,sum_LorentzianPeak_PolynomialBac(x,*popt1),color='k')

xlabel(r'$\mathbf{Q}_{xy}(\AA^{-1})$',fontsize=tfont)

ylabel(r'$\mathbf{Normalised Int. Intensity}$',fontsize=tfont)

qmin = round(qmin, 2)

qmax = round(qmax, 2)

xticks(linspace(-qmin,-qmax,3),fontsize=tfont)

yticks(linspace(0,0.15,4),fontsize=tfont)

```

APPENDIX F (Continued)

```

pl.title(r'\mathbf{Left\ Peak }$', fontsize=tfont)

pl.legend(loc='best', fontsize=16)

x=pl.array(x)

y=pl.array(y)

y_fit=pl.array(sum_LorentzianPeak_PolynomialBac(x,*popt1))

y_err=pl.array(y_err)

np.savetxt('C:\Users\damoan2\Documents\December_Analysis_2017\Save_GISAXS_In_Plane_
Fits\LeftPeak'+fname, np.vstack((x, y,y_err, y_fit)).T)

q0,q0_err,w0,w0_err=(popt[3]+abs(popt1[3]))/2.0,(pcov[0][3]+abs(pcov1[0][3]))/2.0,(popt[6]+a
bs(popt1[6]))/2.0,(pcov[0][6]+abs(pcov1[0][6]))/2.0

return q0,q0_err,w0,w0_err

plt.tight_layout()

os.chdir('C:\Users\damoan2\Documents\Analysing_Cuts__2016_2018\August2017_Analysis_UI
C\GISAXS')

```

OUTPUT/CALLING FUNCTION

```

data=pl.loadtxt('gisaxs_cut_400mVS# 229_sumcut.txt')

fac040=peak_fit(data,qmin=0.06, qmax=0.24,tit='400(+60) mV',col='r',fname='400mV_2017')

#####

```

APPENDIX F (Continued)

THIS PROGRAM FITS THE LOW Q 3D DATA FOR THE PEAK CENTERS.

```

def sum_1_Lorentzian_one_constant(x,fac2,q02,w2,fac3,q03,w3,a0,a1):

    p1=func_Lorentzian(x,fac2,q02,w2)

    p2=func_Polynomial(x,a0,a1)

    p3=func_Lorentzian(x,fac3,q03,w3)

    return p1+p3+p2

#####

def peak_fit1(data,qmin=0,qmax=0.29,lim=0.6,tit=",plt=0,col='ro',fname="):

    if plt==3:# polynomial background

        tfont=16

        ind=nonzero(where(data[:,0]>qmin,data[:,0],0)*where(data[:,0]<qmax,1.0,0))

        x=data[:,0][ind];y=data[:,1][ind]

        x=pl.array(x);y=pl.array(y)

        fac2,q02,w2,fac3,q03,w3,a0,a1=(1.2,0.015,0.019,1.6,0.01,0.0015,0.7,1.0)#q02=0.0188

        p0 = (fac2,q02,w2,fac3,q03,w3,a0,a1)

        popl,pcov=curve_fit(sum_1_Lorentzian_one_constant,x,y,p0,maxfev=50000000)

        print popl

    #   fac2,q02,w2,fac3,q03,w3=popl

    #   return popl,pcov

    subplot(121)

    plot(x,y,col,label=fname)

```

APPENDIX F (Continued)

```

plot(x,sum_1_Lorentzial_one_constant(x,*popt),color='k',lw=2)
ylabel(r'$\mathbf{Normalised\ Int.\ Intensity}$',fontsize=tfont)
xticks(linspace(round(qmin,2),round(0.12,2),3),fontsize=tfont)
#   yticks(linspace(0,0.15,4),fontsize=tfont)
yticks(fontsize=tfont)
#   pl.xlim(0.01,0.16)
xticks(linspace(round(qmin,2),round(0.21,2),3),fontsize=tfont)
#   pl.legend(loc='best',fontsize=tfont)
xlabel(r'$\mathbf{Q_{z}(\AA^{-1})}$',fontsize=16)
pl.legend(loc='best',fontsize=tfont)
#   popt=abs(popt)
popt=abs(popt)
subplot(122)
#   x_peak=pl.arange(-0.01,0.09,0.01)
pl.plot(x,sum_1_Lorentzial_one_constant_residue(x,*popt),col,lim)
pl.plot(0,0,col,label=fname)
#   pl.plot(x,sum_1_Lorentzial_one_constant_residue(x,*popt),'bo',lim)
#   plot(x,func_Polynomial(x,*popt[5:9]))
xlabel(r'$\mathbf{Q_{z}(\AA^{-1})}$',fontsize=tfont)
ylabel(r'$\mathbf{Normalised\ Int.\ Peak\ Intensity}$',fontsize=tfont)
xticks(linspace(0,0.14,3),fontsize=tfont)

```

APPENDIX G

```
#####
```

FITTING THE TEM NANOPARTICLE SIZES WITH LOGNORMAL DISTRIBUTION

FUNCTION

```
import pylab as pl
from scipy.optimize import leastsq
import numpy as np
pl.figure(figsize=(10,10))

fname =
pl.loadtxt('/home/daniel/Documents/2015apr_TMA/Length_Distribution_Bin_15.
txt')
x = fname[:, 0]/2.0
x = pl.array(x)
print x
#####
def logNormal(par, x):
    R, Rsig, fac =par
    sig =np.sqrt(np.log(1.0+Rsig**2/R**2))
    mu =np.log(R)-0.5*sig**2
    if type(x) is np.ndarray:
        return fac*np.exp(-(np.log(x)-
mu)**2/2.0/sig**2)/np.sqrt(2*np.pi)/x/sig
    else:
        return fac*np.exp(-(np.log(x)-
mu)**2/2.0/sig**2)/np.sqrt(2*np.pi)/x/sig

y = fname[:, 1]
print y
def residue(par, x, y):
    return y-logNormal(par, x)

R,Rsig, fac = (1.0, 0.90, 10)
p0 = [R, Rsig, fac]

par = leastsq(residue, p0, args=(x, y))
```

APPENDIX G (Continued)

```
R, Rsig, fac = par[0]
print par[0]

#pl.annotate(" R, Rsig = 1.14034845, 0.32818181", color="r", xy =
(0.7,150),fontsize=16)
pl.annotate(" R, Rsig = 1.11954556 0.19850886", color="k", xy =
(0.7,230),fontsize=16)

barw = x[1]-x[0]
pl.bar(x-barw/2, y, barw)
xlog = np.arange(0.1, x[-1], 0.01)
pl.plot(xlog, logNormal(par[0], xlog), 'r-')
pl.ylabel('Number of particles')
pl.xlabel('Particle size (nm)')
pl.xticks(np.arange(0.1, 3.5, 0.6))
pl.yticks(np.arange(0, 250, 50))
pl.title("A plot of number of nanoparticles versus particle size from TEM
image")
pl.show()
```

```
#####
```

APPENDIX H

```
#PLYNOMIAL FIT OF ZCP
```

```
def func(par,volt):
```

```
    a,b,c,d = par
```

```
    return a*(volt**3)+(b*volt**2)+c*(volt)+d
```

```
def residue(par,volt,tension):
```

```
    return tension-func(par,volt)#[0] had to comment it out to get realistic answer
```

```
a,b,c,d = (2,3,1,0.5)
```

```
p0 = [a,b,c,d]
```

```
par= leastsq(residue,p0,args=(volt,tension),full_output=1)
```

```
print par
```

```
print "par[1]=",par[1]
```

```
a,b,c,d = par[0]
```

```
print 'a,b,c,d=',a,b,c,
```

```
# Testing values again
```

```
i = 150
```

```
print a*(i**3)+b*(i**2)+c*(i)+d
```

```
B = (2*b)/(3*a)
```

```
C = c/(3*a)
```

```
V1 = (-B+(B**2-(4*C*1))**0.5)/2
```

```
V2 = (-B-(B**2-(4*C*1))**0.5)/2
```

APPENDIX H (Continued)**EXCESS SURFACE CHARGE INTERPOLATION AND ESTIMATION OF THE ELECTROLYTES**

```
import numpy as np
```

```
from scipy.interpolate import interp1d
```

```
from scipy.interpolate import InterpolatedUnivariateSpline
```

```
import matplotlib.pyplot as plt
```

```
from scipy.optimize import leastsq
```

```
import numpy as np
```

```
import pylab as pl
```

```
import matplotlib.pyplot as plt
```

```
import sys
```

```
import os
```

```
import pylab as pl
```

```
import numpy as np
```

```
import matplotlib.pyplot as plt
```

```
from scipy.optimize import leastsq
```

```
tension_50NP=arrays of tension measurements
```

```
tension_50NP=pl.array(tension_50NP)
```

```
volt_50NP = [400,380,350,300,250,200,150]# interfacial potential of the cells in mV
```

APPENDIX H (Continued)

```
volt_50NP=pl.array(volt_50NP)
volt=volt_50NP
tension=input_value (arrays)
z_salt = np.polyfit(volt ,tension, 4)# 1D polynomial to the fourth order
f = np.poly1d(z_salt)
# calculate new x's and y's
volt5_new = np.linspace(volt[0], volt[-1])
tension_new = f(volt5_new)
volt5_new=pl.array(volt5_new)
tension_new =pl.array(tension_new )

Z_salt_300= np.polyfit(volt,tension_50NP,4)
f_300 = np.poly1d(Z_salt_300)
volt5_new2=np.linspace(volt[0], volt[-1])
tension_new2 = f_300(volt5_new2)
```

APPENDIX I

XR Measurements with 60 nM nanoparticle concentration at Argonne National Lab

$\Delta\phi^{w-0}$ (mV)	Measurements' Time (hrs)
60	26.83
40	5.2
10	18.2
-40	6.3
-90	2.1
-140	0.5
-190	0.5

XR Measurements with 35 nM nanoparticle concentration at Argonne National Lab

$\Delta\phi^{w-0}$ (Mv)	Measurements' Time (hrs)
60	16
40	6.8
10	Skipped after 4 hours (Still not equilibrated)
-40	5.7
-90	4
-140	3.5
-190	1

VITA

DANIEL AMOANU

773-754-5111

800 South Wells, Chicago, IL 60607 damoan2@uic.edu

Education**Ph.D.** Chemical Engineering; **University of Illinois at Chicago**, USA

Area of Specialization: Liquid-liquid Interfacial Studies, May 2018

MSc. Chemical Engineering; **Lappeenranta University of Technology**, Finland

Thesis: Design of Fiber Coalescers June 2009

BSc. Chemical Engineering; **Kwame Nkrumah University of Science and Technology**,
Ghana Jan. 2003

Project: Designed a process plant to produce a million tons of caustic soda, Nov. 2003

Relevant Course Work

Ph.D.: Partial Differential Equations, Applied Differential Equations, Computational Statistics, Heat Transfer, Microhydrodynamics, Fluid Phase Equilibria, Nanotechnology, Nanoscale Semiconductor Structures, Transport Phenomena, Numerical Methods, Machining Scientific Equipment, Selected Courses in Chemical Engineering, Written Communication

Msc.: Creative Design, Product Design, Modelling Methodology in Process Engineering, R&D Methodology, Process Simulation, Production Planning, Process Intensification, Modelling of Process Intensification, Chemical Engineering Unit Operations, Filtration and Mixing, Treatment Process of Industrial Discharges, Chemical Separation Methods, Advanced Course in Environmental Technology, Bioenergy, Project on Process Plant Design, English for Negotiating, Machines and Processes, Properties of Gases and Liquids

Professional Experience

Argonne National Laboratory

Research Assistant (X-ray User)

March 2012-2018

- Investigate formations of gold nanoparticles at an electrified water/oil interface using X-ray to probe the structure of the clusters
- Investigate plasmon resonance of gold nanoparticle arrays using X-ray to probe the structure
- Investigate arrays of triptycene based compounds at water/oil interface using X-ray
- Monitor equilibration times of gold and triptycene-based compound using quasi-elastic light scattering technique (QELS)
- Assemble engineering controls for laser hazard prevention
- Take stock of wastes generated after experimental run and properly dispose them

University of Illinois at Chicago, Department of Physics

Research Assistant

March 2012-2018

- Write proposals to Argonne National Laboratory to request experiment time allocation
- Give weekly report on research progress to advisor and group members
- Synthesize organic salt for interfacial experiment measurements
- Analyze nanoparticles' sizes and distribution from TEM images using ImageJ software
- Purify crystalline salt and solvents using distillation and chromatographic techniques
- Align and optimize laser for interfacial tension measurement
- Measure interfacial tension of adsorbed gold nanoparticles and triptycene-based compounds using QELS

- Perform electrochemistry experiment using cyclic voltammetry, potential static and potential dynamic techniques
- Organize laboratory cleaning, waste disposal, material purchasing and requests for repairs in the laboratory
- Train undergraduate students in methods of scientific research

Argonne National Laboratory, ChemMatCARS (University of Chicago)

Summer Intern

May-June 2017

Modelled nanoparticle interactions with X-ray at an electrified interface

- Qualitatively analyzed X-ray data
- Wrote relevant functions to quantify X-ray interaction with nanoparticles at water/oil interface
- Tested model integrity and parameter sensitivity using X-ray principles, theories, experience and intuitions
- Fitted experimental data and investigated error on extracted parameters
- Provided reports and presentations on project progress to staff and supervisors

Aalto University, Finland

Research Assistant

Jan. 2010-Sept. 2010

This project was a collaboration between Outotec- Finnish company providing technology solutions and services to the metal and mineral processing industries- and the Department of Material Science and Engineering at Aalto University. I compared the material and exergy consumption of three competing copper smelting technologies using HSC software.

- Calculated the exergy and material input and output of the copper smelting processes
- Selected the best copper smelting process based on material and exergy efficiency
- Organized meetings with Outotec to discuss progress of the project

Lappeenranta University of Technology, Finland

Research Assistant (MSc. Thesis)

Fall 2006- Spring 2009

Investigated the separation efficiency of different fiber coalescers varying emulsion flowrate, emulsion phase ratios used and coalescer thickness

- Designed and purchased design materials such as static mixers and pumps for creating the emulsion
- Used high-resolution Hamamatsu camera to study the images of the emulsion droplets
- Characterized the separation efficiencies of the fiber coalescers based on droplet size distributions of the feed and the emulsions through the fiber coalescer

University of Illinois at Chicago, Department of Physics

Teaching Assistant

Spring 2012-Present

- Guide 40-45 undergraduate students per semester to perform laboratory experiments on magnetism, electricity and mechanics
- Tutor undergraduate students in physics 5 hours per week

University of Illinois at Chicago, Department of Chemistry

Teaching Assistant

Spring 2011-Summer 2012

- Guided 40 undergraduate students to perform experiments on general chemistry
- Tutored undergraduate students in chemistry 4 hours per week

Publications

- Nanoscale View of Assisted Ion Transport Across the Liquid-Liquid Interface
Zhu Liang, Wei Bu, Karl J. Schweighofer, David J. Walwark, Jeffrey S. Harvey, Glenn R. Hanlon, **Daniel Amoanu**, Cem Erol, Ilan Benjamin and Mark L. Schlossman, PNAS, 1-6 (2018)
- X- ray Studies of Interfacial Strontium–Extractant Complexes in a Model Solvent Extraction System, Wei Bu, Miroslav Mihaylov, **Daniel Amoanu**, Binhua Lin, Mati Meron, Ivan Kuzmenko, L. Soderholm, Mark L. Schlossman, Journal of Physical Chemistry B 118, 12486-12500 (2014)
- Interfacial Localization and Voltage-Tunable Arrays of Charged Nanoparticles, M. K. Bera, H. Chan, D. F. Moyano, H. Yu, S. Tatur, **D. Amoanu**, W. Bu, V. M. Rotello, M. Meron, P. Král, B. Lin, and M. L. Schlossman, Nano Letters 14, 6816-6822 (2014)
- Studies of Liquid/Liquid Separation with Fiber Coalescence, **Daniel Amoanu** (2009)

Skills

- Python, Fortran and R
- ImageJ, HSC Chemistry
- Corrware and Corrview for electrochemical experiments
- Windows and Linux operating systems
- Basic Command of Finnish Language

Services and Activities

Physics Department, **University of Illinois at Chicago**

Invited Speaker

March 9, 2016

- Presented “Voltage Tunable Nanoparticles Arrays” to an audience of about 30 graduate research students discussing how gold nanoparticles order at an electrified water/oil interface and their potential applications

Invited Speaker

March 2, 2018

- Physics Festival, March 2018, Presented “ X-ray Study of Electrostatic Induced 2D and 3D Assembly of Charged Nanoparticles at Water/1,2-dichloroethane Interface”

Panelist

March 2, 2018

- Physics Career Panel for Graduate Students, 27 April 2018. Shared some tips and experience on job search for graduate students looking forward to working in industries and answered questions from the audience and the host.

University of Ghana, Legon

August 2004-Jan 2005

Volunteer Researcher

- Investigated the health status of certain communities in Ghana using proxy indicators such as sources of water, waste disposal systems, life styles and occupations
- Interacted with community members, clinics and hospitals to identify their health and social challenges
- Communicated final data to relevant authorities to help improve health measures

Interests

- Reading books, playing and watching sports, travelling and listening to music

REFERENCES

1. Flatte M, Kornyshev A, Urbakh M. Electrovariable nanoplasmonics and self-assembling smart mirrors. *The Journal of Physical Chemistry C*. 2010;114(4):1735-47.
2. Huang X, El-Sayed MA. Gold nanoparticles: optical properties and implementations in cancer diagnosis and photothermal therapy. *Journal of advanced research*. 2010;1(1):13-28.
3. Schmid G. *Nanoparticles: from theory to application*. 2004. Wiley-VCH, Weinheim.
4. Waite TD, Schäfer AI, Fane AG, Heuer A. Colloidal fouling of ultrafiltration membranes: impact of aggregate structure and size. *Journal of Colloid and Interface Science*. 1999;212(2):264-74.
5. Giner-Casares JJ, Henriksen-Lacey M, Coronado-Puchau M, Liz-Marzan LM. Inorganic nanoparticles for biomedicine: where materials scientists meet medical research. *Materials Today*. 2016;19(1):19-28.
6. Taylor R, Coulombe S, Otanicar T, Phelan P, Gunawan A, Lv W, et al. Small particles, big impacts: a review of the diverse applications of nanofluids. *Journal of Applied Physics*. 2013;113(1):1.
7. Yen Y-T, Lu T-Y, Lee Y-C, Yu C-C, Tsai Y-C, Tseng Y-C, et al. Highly reflective liquid mirrors: Exploring the effects of localized surface plasmon resonance and the arrangement of nanoparticles on metal liquid-like films. *ACS applied materials & interfaces*. 2014;6(6):4292-300.
8. Koo HY, Yi DK, Yoo SJ, Kim DY. A Snowman-like Array of Colloidal Dimers for Antireflecting Surfaces. *Advanced Materials*. 2004;16(3):274-7.
9. Turek VA, Cecchini MP, Paget J, Kucernak AR, Kornyshev AA, Edel JB. Plasmonic ruler at the liquid-liquid interface. *ACS nano*. 2012;6(9):7789-99.
10. Renaud G, Lazzari R, Leroy F. Probing surface and interface morphology with grazing incidence small angle X-ray scattering. *Surface Science Reports*. 2009;64(8):255-380.
11. Young KL, Jones MR, Zhang J, Macfarlane RJ, Esquivel-Sirvent R, Nap RJ, et al. Assembly of reconfigurable one-dimensional colloidal superlattices due to a synergy of fundamental nanoscale forces. *Proceedings of the National Academy of Sciences*. 2012;109(7):2240-5.

12. Meyer R, Lemire C, Shaikhutdinov SK, Freund H-J. Surface chemistry of catalysis by gold. *Gold Bulletin*. 2004;37(1-2):72-124.
13. Teichert C. Self-organization of nanostructures in semiconductor heteroepitaxy. *Physics Reports*. 2002;365(5-6):335-432.
14. Gartia MR, Hsiao A, Pokhriyal A, Seo S, Kulsharova G, Cunningham BT, et al. Colorimetric plasmon resonance imaging using nano lycurgus cup arrays. *Advanced Optical Materials*. 2013;1(1):68-76.
15. Park J, Yeo J-S. Colorimetric detection of microRNA miR-21 based on nanoplasmonic core-satellite assembly. *Chemical Communications*. 2014;50(11):1366-8.
16. Cecchini MP, Turek VA, Paget J, Kornyshev AA, Edel JB. Self-assembled nanoparticle arrays for multiphase trace analyte detection. *Nature materials*. 2013;12(2):165.
17. Galarreta BC, Norton PR, Lagugn -Labarthe Fo. SERS detection of streptavidin/biotin monolayer assemblies. *Langmuir*. 2011;27(4):1494-8.
18. Mahajan S, Abdelsalam M, Suguwara Y, Cintra S, Russell A, Baumberg J, et al. Tuning plasmons on nano-structured substrates for NIR-SERS. *Physical Chemistry Chemical Physics*. 2007;9(1):104-9.
19. Ramsden W. Separation of solids in the surface-layers of solutions and 'suspensions'(observations on surface-membranes, bubbles, emulsions, and mechanical coagulation).—Preliminary account. *Proceedings of the royal Society of London*. 1904;72(477-486):156-64.
20. Pickering SU. CXCVI.—emulsions. *Journal of the Chemical Society, Transactions*. 1907;91:2001-21.
21. Flatt  M, Kornyshev A, Urbakh M. Giant Stark effect in quantum dots at liquid/liquid interfaces: A new option for tunable optical filters. *Proceedings of the National Academy of Sciences*. 2008;105(47):18212-4.
22. Luo G, Malkova S, Yoon J, Schultz DG, Lin B, Meron M, et al. Ion distributions near a liquid-liquid interface. *Science*. 2006;311(5758):216-8.
23. Su B, Abid J-P, Ferm n DJ, Girault HH, Hoffmannov H, Krtil P, et al. Reversible voltage-induced assembly of Au nanoparticles at liquid| liquid interfaces. *Journal of the American Chemical Society*. 2004;126(3):915-9.

24. Pieranski P. Two-dimensional interfacial colloidal crystals. *Physical Review Letters*. 1980;45(7):569.
25. Brust M. M. Brust, M. Walker, D. Bethell, DJ Schiffrin, and R. Whyman, *Chem. Commun.(Cambridge, UK)*(1994) 801. *Chem Commun(Cambridge, UK)*.1994:801.
26. Heath JR, Knobler CM, Leff DV. Pressure/temperature phase diagrams and superlattices of organically functionalized metal nanocrystal monolayers: the influence of particle size, size distribution, and surface passivant. *The Journal of Physical Chemistry B*. 1997;101(2):189-97.
27. Markovich G, Collier CP, Heath JR. Reversible metal-insulator transition in ordered metal nanocrystal monolayers observed by impedance spectroscopy. *Physical review letters*. 1998;80(17):3807.
28. Edel JB, Kornyshev AA, Urbakh M. Self-assembly of nanoparticle arrays for use as mirrors, sensors, and antennas. *ACS nano*. 2013;7(11):9526-32.
29. Luo M, Olivier GK, Frechette J. Electrostatic interactions to modulate the reflective assembly of nanoparticles at the oil–water interface. *Soft Matter*. 2012;8(47):11923-32.
30. Kutuzov S, He J, Tangirala R, Emrick T, Russell T, Böker A. On the kinetics of nanoparticle self-assembly at liquid/liquid interfaces. *Physical Chemistry Chemical Physics*. 2007;9(48):6351-8.
31. Xia H, Wang D. Fabrication of Macroscopic Freestanding Films of Metallic Nanoparticle Monolayers by Interfacial Self-Assembly. *Advanced Materials*. 2008;20(22):4253-6.
32. Lin Y, Skaff H, Böker A, Dinsmore A, Emrick T, Russell TP. Ultrathin cross-linked nanoparticle membranes. *Journal of the American Chemical Society*. 2003;125(42):12690-1.
33. Ritcey AM, Borra E. Magnetically deformable liquid mirrors from surface films of silver nanoparticles. *ChemPhysChem*. 2010;11(5):981-6.
34. Wang D, Duan H, Möhwald H. The water/oil interface: the emerging horizon for self-assembly of nanoparticles. *Soft Matter*. 2005;1(6):412-6.
35. Flatte M, Kornyshev A, Urbakh M. Nanoparticles at electrified liquid–liquid interfaces: new options for electro-optics. *Faraday discussions*. 2009;143:109-15.
36. Bresme F, Quirke N. Computer simulation study of the wetting behavior and line tensions of nanometer size particulates at a liquid-vapor interface. *Physical review letters*. 1998;80(17):3791.

37. Luo M, Song Y, Dai LL. Effects of methanol on nanoparticle self-assembly at liquid-liquid interfaces: A molecular dynamics approach. *The Journal of chemical physics*. 2009;131(19):194703.
38. Luo M, Dai LL. Molecular dynamics simulations of surfactant and nanoparticle self-assembly at liquid-liquid interfaces. *Journal of Physics: Condensed Matter*. 2007;19(37):375109.
39. Reincke F, Kegel WK, Zhang H, Nolte M, Wang D, Vanmaekelbergh D, et al. Understanding the self-assembly of charged nanoparticles at the water/oil interface. *Physical Chemistry Chemical Physics*. 2006;8(33):3828-35.
40. Grzelczak M, Vermant J, Furst EM, Liz-Marzán LM. Directed self-assembly of nanoparticles. *ACS nano*. 2010;4(7):3591-605.
41. Park BJ, Pantina JP, Furst EM, Oettel M, Reynaert S, Vermant J. Direct measurements of the effects of salt and surfactant on interaction forces between colloidal particles at water-oil interfaces. *Langmuir*. 2008;24(5):1686-94.
42. Flatté M, Kornyshev A, Urbakh M. Understanding voltage-induced localization of nanoparticles at a liquid-liquid interface. *Journal of Physics: Condensed Matter*. 2008;20(7):073102.
43. Boneva MP, Danov KD, Christov NC, Kralchevsky PA. Attraction between particles at a liquid interface due to the interplay of gravity-and electric-field-induced interfacial deformations. *Langmuir*. 2009;25(16):9129-39.
44. Li YJ, Huang WJ, Sun SG. A Universal Approach for the Self-Assembly of Hydrophilic Nanoparticles into Ordered Monolayer Films at a Toluene/Water Interface. *Angewandte Chemie International Edition*. 2006;45(16):2537-9.
45. Bera MK, Chan H, Moyano DF, Yu H, Tatur S, Amoanu D, et al. Interfacial localization and voltage-tunable arrays of charged nanoparticles. *Nano letters*. 2014;14(12):6816-22.
46. Su B, Fermín DJ, Abid J-P, Eugster N, Girault HH. Adsorption and photoreactivity of CdSe nanoparticles at liquid|liquid interfaces. *Journal of Electroanalytical Chemistry*. 2005;583(2):241-7.
47. Brugger B, Rosen BA, Richtering W. Microgels as stimuli-responsive stabilizers for emulsions. *Langmuir*. 2008;24(21):12202-8.
48. Brugger B, Vermant J, Richtering W. Interfacial layers of stimuli-responsive poly-(N-isopropylacrylamide-co-methacrylic acid)(PNIPAM-co-MAA) microgels characterized by

interfacial rheology and compression isotherms. *Physical Chemistry Chemical Physics*. 2010;12(43):14573-8.

49. Edwards EW, Chanana M, Wang D, Möhwald H. Stimuli-Responsive Reversible Transport of Nanoparticles Across Water/Oil Interfaces. *Angewandte Chemie International Edition*. 2008;47(2):320-3.

50. Montelongo Y, Sikdar D, Ma Y, McIntosh AJ, Velleman L, Kucernak AR, et al. Electrotunable nanoplasmonic liquid mirror. *Nature materials*. 2017;16(11):1127.

51. Cecchini MP, Turek VA, Demetriadou A, Britovsek G, Welton T, Kornyshev AA, et al. Heavy Metal Sensing Using Self-Assembled Nanoparticles at a Liquid-Liquid Interface. *Advanced Optical Materials*. 2014;2(10):966-77.

52. Feng T, Hoagland DA, Russell TP. Assembly of acid-functionalized single-walled carbon nanotubes at oil/water interfaces. *Langmuir*. 2014;30(4):1072-9.

53. Sun Z, Feng T, Russell TP. Assembly of graphene oxide at water/oil interfaces: tessellated nanotiles. *Langmuir*. 2013;29(44):13407-13.

54. Kostianen MA, Hiekkataipale P, Laiho A, Lemieux V, Seitsonen J, Ruokolainen J, et al. Electrostatic assembly of binary nanoparticle superlattices using protein cages. *Nature nanotechnology*. 2013;8(1):52-6.

55. Barrow SJ, Funston AM, Wei X, Mulvaney P. DNA-directed self-assembly and optical properties of discrete 1D, 2D and 3D plasmonic structures. *Nano Today*. 2013;8(2):138-67.

56. Eils R, Athale C. Computational imaging in cell biology. *The Journal of cell biology*. 2003;161(3):477-81.

57. Chen X, Murphy RF, editors. Location proteomics: determining the optimal grouping of proteins according to their subcellular location patterns as determined from fluorescence microscope images. *Signals, Systems and Computers, 2004 Conference Record of the Thirty-Eighth Asilomar Conference on*; 2004: IEEE.

58. Kherlopian AR, Song T, Duan Q, Neimark MA, Po MJ, Gohagan JK, et al. A review of imaging techniques for systems biology. *BMC systems biology*. 2008;2(1):74.

59. Seitavuopio P, Rantanen J, Yliruusi J. Tablet surface characterisation by various imaging techniques. *International journal of pharmaceutics*. 2003;254(2):281-6.

60. Luo X-P, Silikas N, Allaf M, Wilson N, Watts D. AFM and SEM study of the effects of etching on IPS-Empress 2TM dental ceramic. *Surface Science*. 2001;491(3):388-94.

61. Danesh A, Chen X, Davies MC, Roberts CJ, Sanders GH, Tandler SJ, et al. The discrimination of drug polymorphic forms from single crystals using atomic force microscopy. *Pharmaceutical research*. 2000;17(7):887-90.
62. Lyklema J. *Fundamentals of interface and colloid science: soft colloids*: Elsevier; 2005.
63. Younan N, Hojeij M, Ribeaucourt L, Girault HH. Electrochemical properties of gold nanoparticles assembly at polarised liquid| liquid interfaces. *Electrochemistry Communications*. 2010;12(7):912-5.
64. Marinescu M, Urbakh M, Kornyshev A. Voltage-dependent capacitance of metallic nanoparticles at a liquid/liquid interface. *Physical Chemistry Chemical Physics*. 2012;14(4):1371-80.
65. Kornyshev AA, Marinescu M, Paget J, Urbakh M. Reflection of light by metal nanoparticles at electrodes. *Physical Chemistry Chemical Physics*. 2012;14(6):1850-9.
66. Kubowicz S, Hartmann MA, Daillant J, Sanyal MK, Agrawal VV, Blot C, et al. Gold Nanoparticles at the Liquid– Liquid Interface: X-ray Study and Monte Carlo Simulation. *Langmuir*. 2008;25(2):952-8.
67. Levine S, Bowen B. Capillary interaction of spherical particles adsorbed on the surface of an oil/water droplet stabilized by the particles. Part I. *Colloids and Surfaces*. 1991;59:377-86.
68. Reincke F, Hickey SG, Kegel WK, Vanmaekelbergh D. Spontaneous assembly of a monolayer of charged gold nanocrystals at the water/oil interface. *Angewandte Chemie International Edition*. 2004;43(4):458-62.
69. Duan H, Wang D, Kurth DG, Möhwald H. Directing self-assembly of nanoparticles at water/oil interfaces. *Angewandte Chemie International Edition*. 2004;43(42):5639-42.
70. Lin Y, Skaff H, Emrick T, Dinsmore A, Russell TP. Nanoparticle assembly and transport at liquid-liquid interfaces. *Science*. 2003;299(5604):226-9.
71. Lin Y, Böker A, Skaff H, Cookson D, Dinsmore A, Emrick T, et al. Nanoparticle assembly at fluid interfaces: structure and dynamics. *Langmuir*. 2005;21(1):191-4.
72. Toor A, Feng T, Russell TP. Self-assembly of nanomaterials at fluid interfaces. *The European Physical Journal E*. 2016;39(5):57.
73. Fokkink LG, Ralston J. Contact angles on charged substrates. *Colloids and surfaces*. 1989;36(1):69-76.

74. Uhlig H. The solubilities of gases and surface tension. *Journal of Physical Chemistry*. 1937;41(9):1215-26.
75. Kornyshev A, Volkov A. On the evaluation of standard Gibbs energies of ion transfer between two solvents. *Journal of electroanalytical chemistry and interfacial electrochemistry*. 1984;180(1-2):363-81.
76. Dishon M, Zohar O, Sivan U. Effect of cation size and charge on the interaction between silica surfaces in 1: 1, 2: 1, and 3: 1 aqueous electrolytes. *Langmuir*. 2011;27(21):12977-84.
77. Dishon M, Zohar O, Sivan U. From repulsion to attraction and back to repulsion: the effect of NaCl, KCl, and CsCl on the force between silica surfaces in aqueous solution. *Langmuir*. 2009;25(5):2831-6.
78. Cates M, Adhikari R, Stratford K. Colloidal arrest by capillary forces. *Journal of Physics: Condensed Matter*. 2005;17(31):S2771.
79. Aveyard R, Binks BP, Clint JH. Emulsions stabilised solely by colloidal particles. *Advances in Colloid and Interface Science*. 2003;100:503-46.
80. Onsager L. The effects of shape on the interaction of colloidal particles. *Annals of the New York Academy of Sciences*. 1949;51(1):627-59.
81. Vella D, Mahadevan L. The “cheerios effect”. *American journal of physics*. 2005;73(9):817-25.
82. Danov KD, Kralchevsky PA, Boneva MP. Electrodipping force acting on solid particles at a fluid interface. *Langmuir*. 2004;20(15):6139-51.
83. Aveyard R, Binks B, Clint J, Fletcher P, Horozov T, Neumann B, et al. Measurement of long-range repulsive forces between charged particles at an oil-water interface. *Physical review letters*. 2002;88(24):246102.
84. Aveyard R, Clint JH, Nees D, Paunov VN. Compression and structure of monolayers of charged latex particles at air/water and octane/water interfaces. *Langmuir*. 2000;16(4):1969-79.
85. Nikolaides M, Bausch A, Hsu M, Dinsmore A, Brenner M, Gay C, et al. Electric-field-induced capillary attraction between like-charged particles at liquid interfaces. *Nature*. 2002;420(6913):299.
86. Danov K, Kralchevsky P, Ananthapadmanabhan K, Lips A. Particle– Interface Interaction across a Nonpolar Medium in Relation to the Production of Particle-Stabilized Emulsions. *Langmuir*. 2006;22(1):106-15.

87. Leunissen ME, Van Blaaderen A, Hollingsworth AD, Sullivan MT, Chaikin PM. Electrostatics at the oil–water interface, stability, and order in emulsions and colloids. *Proceedings of the National Academy of Sciences*. 2007;104(8):2585-90.
88. Gilbert B, Lu G, Kim CS. Stable cluster formation in aqueous suspensions of iron oxyhydroxide nanoparticles. *Journal of colloid and interface science*. 2007;313(1):152-9.
89. Hamaker H. The London—van der Waals attraction between spherical particles. *physica*. 1937;4(10):1058-72.
90. Kirkwood JG, Poirier JC. The statistical mechanical basis of the Debye–hückel theory of strong electrolytes. *The Journal of Physical Chemistry*. 1954;58(8):591-6.
91. Laanait N, Mihaylov M, Hou B, Yu H, Vanýsek P, Meron M, et al. Tuning ion correlations at an electrified soft interface. *Proceedings of the National Academy of Sciences*. 2012;109(50):20326-31.
92. Moyano DF, Rotello VM. Nano meets biology: structure and function at the nanoparticle interface. *Langmuir*. 2011;27(17):10376-85.
93. Moyano DF, Duncan B, Rotello VM. Preparation of 2 nm gold nanoparticles for in vitro and in vivo applications. *Nanomaterial Interfaces in Biology: Springer*; 2013. p. 3-8.
94. Hou B, Laanait N, Yu H, Bu W, Yoon J, Lin B, et al. Ion distributions at the water/1, 2-dichloroethane interface: Potential of mean force approach to analyzing X-ray reflectivity and interfacial tension measurements. *The Journal of Physical Chemistry B*. 2013;117(17):5365-78.
95. Ross S, Chen E. Adsorption and thermodynamics at the liquid-liquid interface. *Industrial & Engineering Chemistry*. 1965;57(7):40-52.
96. Gibbs JW. *The scientific papers of J. Willard Gibbs*: Longmans, Green and Company; 1906.
97. Weil K. JS Rowlinson and B. Widom: *Molecular Theory of Capillarity*, Clarendon Press, Oxford 1982. 327 Seiten, Preis:£ 30,-. *Berichte der Bunsengesellschaft für physikalische Chemie*. 1984;88(6):586-.
98. Langevin D. *Light scattering by liquid surfaces and complementary techniques*: M. Dekker; 1992.
99. Lamb H. *Hydrodynamics* 6th ed., 738. Dover, New York; 1932.
100. Mabbott GA. An introduction to cyclic voltammetry. *Journal of Chemical education*. 1983;60(9):697.

101. Samec Z, Mareček V, Koryta J, Khalil M. Investigation of ion transfer across the interface between two immiscible electrolyte solutions by cyclic voltammetry. *Journal of Electroanalytical Chemistry and Interfacial Electrochemistry*. 1977;83(2):393-7.
102. Samec Z, Mareček V, Weber J. Charge transfer between two immiscible electrolyte solutions: Part II. The investigation of Cs⁺ ion transfer across the nitrobenzene/water interface by cyclic voltammetry with IR drop compensation. *Journal of Electroanalytical Chemistry and Interfacial Electrochemistry*. 1979;100(1-2):841-52.
103. Strutwolf J, Scanlon MD, Arrigan DW. Electrochemical ion transfer across liquid/liquid interfaces confined within solid-state micropore arrays—simulations and experiments. *Analyst*. 2009;134(1):148-58.
104. Pershan PS, Schlossman M. *Liquid Surfaces and Interfaces: Synchrotron X-ray Methods*: Cambridge University Press; 2012.
105. Als-Nielsen J, McMorrow D. *Elements of modern X-ray physics*: John Wiley & Sons; 2011.
106. Griffiths DJ. *Introduction to electrodynamics*. Prentice-Hall; 1999.
107. Parratt LG. Surface studies of solids by total reflection of X-rays. *Physical review*. 1954;95(2):359.
108. Samec Z. *Electrochemistry at the interface between two immiscible electrolyte solutions (IUPAC Technical Report)*. *Pure and applied chemistry*. 2004;76(12):2147-80.
109. Revenant C, Leroy F, Lazzari R, Renaud G, Henry C. Quantitative analysis of grazing incidence small-angle x-ray scattering: Pd/MgO (001) growth. *Physical review B*. 2004;69(3):035411.
110. He J, Zhang Q, Gupta S, Emrick T, Russell TP, Thiyagarajan P. Drying droplets: a window into the behavior of nanorods at interfaces. *Small*. 2007;3(7):1214-7.